

Quantum to classical crossover in cavity QED and optomechanical systems

Inauguraldissertation

zur

Erlangung des akademischen Grades eines

Doktors der Naturwissenschaften

der

Mathematisch-Naturwissenschaftlichen Fakultät

der

Ernst-Moritz-Arndt-Universität Greifswald

vorgelegt von

Lutz Bakemeier

geboren am 25. Januar 1986

in Greifswald

Greifswald, 21 October 2014

Dekan:	Prof. Dr. Klaus Fesser
1. Gutachter:	Prof. Dr. Holger Fehske
2. Gutachter:	Prof. Dr. Tobias Brandes
Tag der Promotion:	21. November 2014

Contents

1	Summary	1
1.1	Introduction	1
1.2	Quantum phase transition in the Dicke model	3
1.3	Regular dynamics of the Dicke model far and near the classical limit	9
1.4	Route to chaos in Dicke and optomechanical systems	16
1.5	Conclusions	21
2	Thesis Articles	25
2.1	Article I — Quantum phase transition in the Dicke model with critical and noncritical entanglement	27
2.2	Article II — Variational treatment of entanglement in the Dicke model	37
2.3	Article III — Collapse-revival dynamics and atom-field entanglement in the nonresonant Dicke model	47
2.4	Article IV — Dynamics of the Dicke model close to the classical limit	55
2.5	Article V — Route to chaos in optomechanics	67
	Bibliography	73
	Publications and Conferences	79
	Erklärung	83
	Acknowledgement	85

1 Summary

1.1 Introduction

Cavity quantum electrodynamics (cavity QED) describes the interaction of light with matter on the most fundamental quantum level. In the paradigmatic Jaynes-Cummings model [Jaynes63] one quantized mode of the electromagnetic field of the cavity couples resonantly to a single atomic excitation. Originally such a simplified model could only be thought of as a gedanken experiment, unable to cope with the actual experimental situation of a leaky cavity containing a vast number of atoms and modes. However for few decades the progress in the manufacturing of optical [Miller05] and microwave [Walther06] cavities made it possible to reach the so called “strong coupling regime”, which actually allows for the study of single atoms interacting with one preferred field mode. This regime is characterized by quantum Rabi oscillations, i.e. the periodic absorption and reemission of a single photon by an atomic two-level system [Brune96]. Other remarkable effects are the generation of atom-field entanglement [Raimond01] and the generation of highly nonclassical field states, e.g., Fock states or coherent superpositions of well separated classical field states, so called “Schrödinger cat states” [Brune90, Brune92, Haroche97]. The creation and measurement of these states, e.g., via quantum state tomography [Lvovsky09] opens the path to a full control of quantum systems for the use of quantum information and computation [Braunstein05] and was rewarded with the Nobel price for physics for Serge Haroche and David Wineland in the year 2012.

Apart of natural atoms passing through or trapped in optical cavities, cavity QED systems can also be implemented with artificial atoms, e.g., superconducting qubits coupled to microwave resonators [Xiang13]. These “circuit QED” systems have the advantage of switchable atom-field coupling [Peropadre10] and the capability to reach the so called “ultrastrong coupling regime”, in which the vacuum Rabi frequency is comparable to the cavity photon frequency [Bourassa09]. Then the traditional rotating wave approximation (RWA) used in the Jaynes-Cummings model breaks down and virtual transitions have to be included in the coupling term leading to the Rabi model [Rabi37]. Furthermore in circuit QED the number of artificial atoms coupled to the same field mode can arbitrarily be set, which allows for the realization of prototypical models of quantum optics and nuclear physics like the Tavis-Cummings model [Fink09] or the Lipkin-Meshkov-Glick model [Larson10]. This opens the possibility to create collective atomic states and to study the superradiant phase transition taking place in these models.

Another upcoming branch of cavity QED promising fundamental research and technological applications are optomechanical systems, in which the field mode does not couple to an atomic transition, but to nano- or micromechanical motion [Kippenberg08, Marquardt09, Aspelmeyer13, Meystre13]. Because the light-matter coupling and other system parameters, e.g., the size of the mechanical cantilever can be adjusted over

large scales, optomechanics provides a genuine opportunity to access the classical and quantum dynamics of mesoscopic driven dissipative systems in a variety of different regimes. In addition optomechanical set-ups with multiple mechanical oscillators coupled to the optical mode allow for the study of collective dynamics and synchronization phenomena [Heinrich11].

In the cavity QED and cavity optomechanical quantum models a great part of the interesting physics emerges strictly in the classical limit. Signatures of these phenomena occur in the quantum regime together with significant quantum corrections. In this thesis we study the quantum to classical crossover of two prototypical models, the Dicke model [Dicke53] and the generic optomechanical system [Law95]. Common to both models is one photon mode of the optical cavity, which is given by a harmonic oscillator with frequency ω_{cav} and bosonic operators $a^{(\dagger)}$. In the Dicke model the photon mode couples via dipole interaction to an ensemble of $2j$ two-level atoms with transition frequency Δ . Combining the two-level atoms into one pseudospin of length j with operators J_x, J_z , the Hamilton operator is given by

$$H_D = \omega_{\text{cav}} a^\dagger a + \lambda(a^\dagger + a) J_x + \Delta J_z . \quad (1)$$

In the optomechanical system the cavity mode interacts via radiation pressure with one phonon mode of a mechanical cantilever, which is given by a harmonic oscillator with frequency ω_{can} and bosonic operators $b^{(\dagger)}$. The Hamilton operator is given by

$$H_O = \omega_{\text{cav}} a^\dagger a + g_0(b + b^\dagger) a^\dagger a + \omega_{\text{can}} b^\dagger b . \quad (2)$$

The classical limit of both models originates from the particular classical limit of a spin or an oscillator. The classical limit of a spin (CS) is simply obtained by increasing its length to infinity ($j \rightarrow \infty$), which results in a classical angular momentum with negligible quantization. For an oscillator with mass m , frequency Ω and spring constant $k_s = m\Omega^2$ the scaling parameter is given by the ground state uncertainty (also called zero point fluctuations) $x_{\text{zpt}} = \sqrt{\hbar/m\Omega} = \sqrt{\hbar/\sqrt{k_s m}}$. A vanishing ground state uncertainty $x_{\text{zpt}} \rightarrow 0$ corresponds to the classical oscillator (CO) limit $m \rightarrow \infty$ with k_s fixed. In the case of the Dicke model, which is considered without dissipation, the CO limit is given by the static limit $\Omega \rightarrow 0$ of the oscillator, i.e., the photon mode ($\Omega \equiv \omega_{\text{cav}}$). In the optomechanical system however dissipation is taken into consideration by means of the quantum-optical master equation as described in Section 1.4. The CO limit of the phonon mode ($\Omega \equiv \omega_{\text{can}}$) is then given as the bad-cavity limit $g_0/\kappa \rightarrow 0$ [Ludwig08], where κ is the damping rate of the optical mode.

In this thesis we pursue of two subjects. First we (re-)examine the physics taking place in the classical limit of both models. Second we point out in which way the classical signatures appear in the quantum regime when the classical limit is approached (see Fig. 1). In Section 1.2 we start with the quantum phase transition (QPT) of the Dicke model taking place strictly only in the classical limit. We point out how the QPT is obtained in the quantum regime following the CO or CS limit, by means of numerical diagonalization and a variational ansatz. In Section 1.3 we turn to the quantum dynamics of the Dicke model. Using perturbation theory we show the underlying mechanism of collapse and revival (CR) in the nonresonant case and the emergence

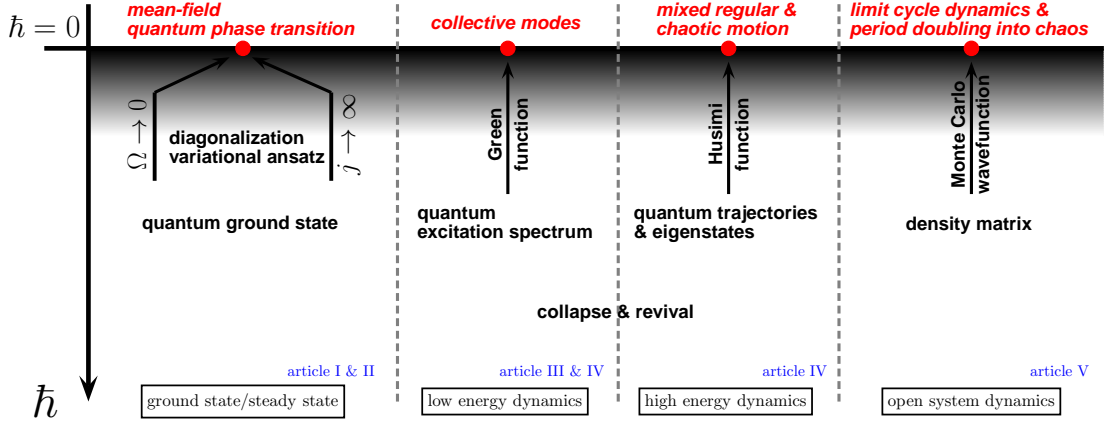


Figure 1: Illustration of cavity QED and optomechanical features emerging in the classical models ($\hbar = 0$) and the quantum-mechanical counterparts. By decreasing the effective Planck constant \hbar , signatures of classical features appear in the quantum-mechanical quantities. Labels at arrows denote the applied methods to undertake the classical limit ($\hbar \rightarrow 0$).

of Schrödinger cat states. We then derive the semiclassical (SC) equations of motion and display their inability to reproduce CR due to the complete neglect of atom-field entanglement. We then turn to the dynamical response of the QPT and show how a certain Green function converges to the classical modes which display collective motion. In Section 1.4 we consider the dynamics at high coupling and energy, where chaotic behavior of the Dicke and the optomechanical model occurs. We revisit classical chaos of the Hamiltonian vs. dissipative system and show how signatures of classical orbits are obtained in the quantum dynamics.

1.2 Quantum phase transition in the Dicke model

Review of mean-field theory The Dicke Hamiltonian (1) has a reflection symmetry, generated by the unitary transformation

$$R = \exp[i\pi(J_z - j)] \exp[i\pi a^\dagger a] \quad (3)$$

with $RJ_xR^\dagger = -J_x$ and $Ra^{(\dagger)}R^\dagger = -a^{(\dagger)}$, leading to $[R, H_D] = 0$. For $j < \infty$ and $\Omega > 0$ this symmetry can not be broken, since the energy of a symmetry-broken state $|\psi\rangle$ can always be lowered by forming the linear combination with the reflected state $R|\psi\rangle$. Nevertheless in the classical limit the overlap $\langle\psi|R|\psi\rangle$ of different classical states vanishes, which circumvents this argument and thus allows symmetry breaking in a quantum phase transition. Then, at the critical coupling $\lambda^2 = (\Delta\Omega)/2j$ the symmetric ground state with $\langle J_x \rangle = \langle a \rangle = 0$ goes over to a two-fold degenerate ground state with finite occupation of the optical mode ($\langle a \rangle > 0$) and macroscopic atomic occupation ($\langle J_x \rangle > 0$) [Hepp73, Wang73]. In order to approach the convergence to the classical limits it is necessary to break the reflection symmetry explicitly, i.e., by adding a symmetry breaking field ϵJ_x with $\epsilon < 0$ to the Hamiltonian H_D .

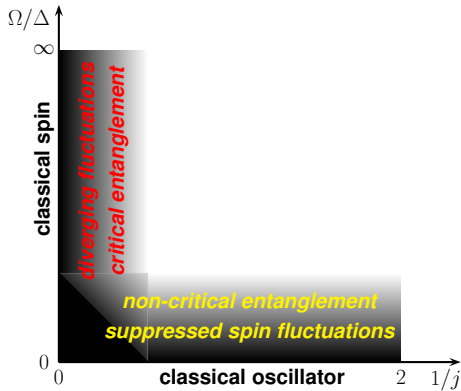


Figure 2: Schematic diagram of the classical limits in the Dicke model. The vertical axis correspond to the CS limit ($1/j = 0$) and the horizontal axis to the CO limit ($\Omega = 0$). Approaching the QPT in the classical limit, diverging quantum fluctuations and critical entanglement occur only for the CS limit, while the CO limit suppresses spin fluctuations leading to a bounded entanglement entropy.

Within the mean-field description of the QPT the product-state ansatz

$$|\psi_{\text{mf}}\rangle = |\phi\rangle \otimes |\chi\rangle, \quad (4)$$

with the spin state $|\phi\rangle$ and the oscillator state $|\chi\rangle$ is used for the ground-state wave function. Spin and oscillator state have to be determined by the minimization of the mean-field energy $\langle\psi_{\text{mf}}|H_{\text{D}}|\psi_{\text{mf}}\rangle$, which results into two individual minimization problems for both states. On the one hand, the spin state $|\phi\rangle$ has to be the ground state of the parametrized spin Hamiltonian

$$H_{\text{mf}}^{\text{s}}(\xi_1) = \Delta J_z + \xi_1 J_x, \quad (5)$$

with $\xi_1 = \kappa\langle\chi|a^\dagger + a|\chi\rangle$. $H_{\text{mf}}^{\text{s}}(\xi_1)$ is the Hamiltonian of a spin in a magnetic field $\vec{B} = (\xi_1, 0, \Delta)$. The spin state $|\phi\rangle$ is thus given by a coherent spin state $|\theta\rangle$ with rotation angle $\tan\theta = \xi_1/\Delta$ [Zhang90]. On the other hand, the oscillator state $|\chi\rangle$ has to be the ground state of the parametrized boson Hamiltonian

$$H_{\text{mf}}^{\text{b}}(\xi_2) = \xi_2(a^\dagger + a) + \Omega a^\dagger a, \quad (6)$$

with $\xi_2 = \kappa\langle\phi|J_x|\phi\rangle$. H_{mf}^{b} is the Hamiltonian of an oscillator displaced by a constant force with amount ξ_2 . The oscillator state is then given by a boson coherent state $|\alpha\rangle$, with $\alpha = -\xi_2/\Omega$. In summary the mean-field ground state $|\psi_{\text{mf}}\rangle = |\theta\rangle \otimes |\alpha\rangle$ is a product state of a spin coherent state $|\theta\rangle$ and an oscillator coherent state $|\alpha\rangle$. Minimizing the ground state energy $\langle\psi_{\text{mf}}|H_{\text{D}}|\psi_{\text{mf}}\rangle$ with respect to α and θ yields $\alpha = -j\lambda/(\Omega)\sin\theta$ with

$$\theta = \begin{cases} 0 & \text{if } \mu < 1, \\ \pm \arccos \frac{1}{\mu} & \text{if } \mu > 1. \end{cases} \quad (7)$$

Here we use the dimensionless coupling constant $\mu = 2j\lambda^2/\Delta\Omega$. Since now the mean-field ground state is fully determined, the given argument about the possibility of symmetry breaking in the classical limit can be confirmed. For $\theta \neq 0$ the overlap $\langle\theta|-\theta\rangle = \cos^{2j}\theta$ goes to zero for $j \rightarrow \infty$, which allows for the QPT in the CS limit. Similarly the overlap $\langle\alpha|-\alpha\rangle = \exp(-2\alpha^2)$ goes to zero for $\mu > 1$, since α scales as $1/\sqrt{\Omega}$ according to Eq. (7). Hence the QPT takes place also in the CO limit independently of

j . Since the mean-field ground state is realized in both classical limits, the QPT in the CS and CO limit show the same critical behavior, which is characterized by the order parameter

$$\langle J_x \rangle = j \sin \theta = \begin{cases} 0 & \text{if } \mu < 1, \\ \pm j \sqrt{1 - \frac{1}{\mu^2}} & \text{if } \mu > 1 \end{cases} \quad (8)$$

and the susceptibility

$$\chi = j \Delta \lim_{\epsilon \rightarrow 0} \frac{\partial \langle J_x \rangle}{\partial \epsilon} = \begin{cases} \frac{1}{1 - \mu} & \text{if } \mu < 1, \\ \frac{1}{\mu(\mu^2 - 1)} & \text{if } \mu > 1. \end{cases} \quad (9)$$

The latter has to be calculated from the symmetry-breaking Hamiltonian $H_\epsilon = H_D + \epsilon J_x$. Using this Hamiltonian it is also possible to show how the order parameter $\langle J_x \rangle$ and the susceptibility χ converge to the mean-field values from Eqs. (8) and (9) when the CO or CS limit is approached from the quantum regime $\Omega/\Delta > 0$ or $j < \infty$. For the numerical calculations reported in Article I we have used $|\epsilon| = 10^{-4}$. As further shown in the article, convergence to the mean-field results is obtained if j is increased with fixed Ω/Δ as well as if Ω/Δ is decreased with fixed j .

Results I: Quantum fluctuations and entanglement Mean-field theory is valid only in the CO and CS limits. For finite $\Omega/\Delta > 0$ and $j < \infty$ quantum fluctuations around the mean-field ground state occur. So far the influence of spin-oscillator correlations and fluctuations were mainly studied for the CS limit [Emary03a, Emary03b, Lambert04, Lambert05]. It has been shown that in this limit corrections to the mean-field ground state can be obtained in leading order of a $1/j$ expansion using the Holstein-Primakoff transformation of spin operators [Holstein40].

We consider quantum fluctuations rising ahead of the CO limit, which point out the differences of the QPTs in both classical limits. The crucial point is that the energy scales for spin fluctuations ($\propto \Delta$) and oscillator fluctuations ($\propto \Omega$) separate. As a result Δ is also larger than the bare coupling parameter $\lambda \propto \sqrt{\Omega}$, thus spin fluctuations are suppressed in the CO limit. Nevertheless oscillator fluctuations remain energetically favorable and can be analyzed with a bosonic model derived by perturbation theory. In the normal phase ($\mu < 1$) the mean-field ground state $|-j\rangle \otimes |\text{vac}\rangle$ is given by the product of the J_z eigenstate $|-j\rangle$ to the smallest eigenvalue $-j$ and the bosonic vacuum. Since $\Delta \gg \Omega$ we only consider the low-energy sector of the Hilbert space which consists of all states $|-j\rangle \otimes |\psi_{\text{bos}}\rangle$ for a given bosonic state $|\psi_{\text{bos}}\rangle$. Perturbation theory gives an effective low-energy model with Hamiltonian $H_{\text{bos}}^<$, which is given in Eq. (14) on page 4 in Article I. In the superradiant phase ($\mu > 1$) fluctuations above the mean-field state $|\theta\rangle \otimes |\alpha\rangle$ with $\theta \neq 0$ have to be considered. Therefore perturbation theory has to be applied to the Hamiltonian with spin and oscillator operators, which are rotated and shifted by the corresponding ground state expectation values. The resulting Hamiltonian $H_{\text{bos}}^>$ is given in Eq. (17) on page 4 in Article I. For $\mu \rightarrow 1$,

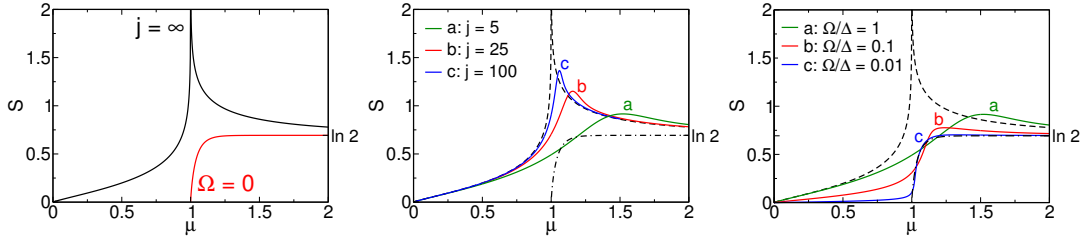


Figure 3: Entanglement in the classical limits and the quantum regime of the Dicke model. Left: Entanglement entropy S in the CS ($j = \infty$) and CO ($\Omega = 0$) limit. Middle: Approaching the CS limit by increasing j for fixed $\Omega/\Delta = 1$. Right: Approaching the CO limit by decreasing Ω/Δ for fixed $j = 5$. (Reproduced from Article I)

$H_{\text{bos}}^>$ coincides with $H_{\text{bos}}^<$. H_{bos}^{\leq} is the Hamiltonian of a squeezed (for $\mu > 1$ also displaced) harmonic oscillator and can be diagonalized by a unitary transformation. The transformed Hamiltonian allows for a simple evaluation of the oscillator variance of the oscillator position $q = (a + a^\dagger)$. As further pointed out in Article I, the variance obtained from H_{bos}^{\leq} is

$$\Delta_q = \begin{cases} (1 - \mu)^{-1/2} & \text{if } \mu < 1, \\ (1 - 1/\mu^2)^{-1/2} & \text{if } \mu > 1. \end{cases} \quad (10)$$

Obviously the oscillator variance diverges at the critical coupling $\mu = 1$, which results from the diverging number of oscillator fluctuations, introduced by the term $(a + a^\dagger)^2$ in $H_{\text{bos}}^<$.

The influence of quantum fluctuations can also be measured by the spin-oscillator entanglement entropy $S = -\text{Tr}[\rho \ln \rho]$ whereas ρ is either the reduced spin or oscillator density matrix. The mean-field state, which neglects spin as well as oscillator fluctuations would suggest a Heaviside function for the entanglement entropy. While the nondegenerate ground state would give $S = 0$ below $\mu = 1$, above the QPT the entropy would be $S = \ln 2$ for the twofold degenerate ground state. Quantum fluctuations modify this behavior significantly. In the CS limit, diverging spin and oscillator fluctuations lead to criticality of entanglement [Lambert04, Lambert05] whereas the entropy diverges at $\mu = 1$ with critical exponent $1/4$ [Lambert05, Vidal07].

For fixed spin length j the entropy is bounded by $S \leq \ln(2j + 1)$, but suppressed spin fluctuations in the CO limit lead to the much stricter condition $S \leq \ln 2$. For $\mu < 1$ the entropy S_{CO} vanishes, since the ground state is a product state even when oscillator fluctuations are included, as confirmed by perturbation theory. For $\mu > 1$ the entanglement entropy is calculated from the reduced spin density matrix of the symmetrized ground-state wave function $|\psi\rangle = 1/\sqrt{2} (|\theta\rangle \otimes |\alpha\rangle \pm |-\theta\rangle \otimes |-\alpha\rangle)$. Although the two oscillator coherent states are orthogonal ($\langle \alpha | -\alpha \rangle = 0$), the spin coherent states are not and the eigenvalues of the reduced spin density matrix are given by $\mu_{\pm} = 1 \pm \langle \theta | -\theta \rangle = 1 \pm \cos^{2j} \theta$. Then the entanglement entropy is given by $S_{\text{CO}} = -\mu_- \ln \mu_- - \mu_+ \ln \mu_+$ and in explicit form in Eq. (24) on page 5 in Article I.

We show $S_{\text{CO}}[\mu > 1]$ together with S_{CS} in Fig. 3 (left panel). While $S_{\text{CO}} = 0$ for $\mu < 1$, it increases from 0 to $\ln 2$ for $\mu > 1$. In the middle and right panel of Fig. 3 we show how the entropy S converges to the analytical results of the classical limits.

We start with the values $j = 5, \Omega/\Delta = 1$. Approaching the CS limit by increasing j with fixed Ω/Δ the divergence of S at $\mu = 1$ develops. Approaching the CO limit by decreasing Ω/Δ with fixed j the entropy S remains small and converges to a continuous function bounded by $\ln 2$.

Results II: Variational ansatz All results so far are obtained by numerical diagonalization for the quantum regime or mean-field theory for the classical limits. In addition our analysis shows how quantum fluctuations around the mean-field state can be included within perturbation theory close to the CO limit. We now ask whether it is possible to go beyond the mean-field description and directly include quantum effects in a variational ansatz for the ground state. We demand not only that the ansatz performs well before the classical limit, i.e., in the regime where mean-field theory fails. We also demand that the ansatz becomes exact in the classical limit, in such a way that the leading quantum corrections are contained. Therefore we improve the mean-field ansatz by including spin-oscillator entanglement and fluctuations. We propose the variational ansatz

$$|\psi\rangle = D_x(\eta)|\phi\rangle \otimes |\chi\rangle \quad (11)$$

with the unitary transformation $D_x(\eta)$ given in Eq. (21) on page 4 in Article II. The variational parameter η ($\eta \in \mathbb{R}$) controls the unitary transformation. For $\eta = 0$ we recover the mean-field ansatz. For $\eta \neq 0$ the transformation can be interpreted as an oscillator shift that depends on the J_x -eigenvalues. This shift introduces spin-oscillator correlations and allows for non-classical fluctuations. The spin state $|\phi\rangle$ and oscillator state $|\chi\rangle$ depend on η and have to be determined within the minimization procedure.

The inclusion of spin-oscillator correlations in the variational state leads to a non-vanishing entanglement entropy S for $\eta > 0$. For $\eta = 0$, the reduced spin density matrix $\rho_s = |\phi\rangle\langle\phi|$ is a pure state with $S = 0$. For $\eta \rightarrow \infty$, ρ_s becomes a diagonal matrix and the entropy attains its maximal value for the given state $|\phi\rangle$. However for each η the entropy is bounded by $S \leq \ln(2j + 1)$.

The energy minimization of the variational ground-state energy $\langle\psi|H_D|\psi\rangle$ can be performed in a similar manner to the derivation of the mean-field state. By tracing out the Hamiltonian in the oscillator state $|\chi\rangle$ or the spin state $|\phi\rangle$ we obtain the effective spin Hamiltonian

$$H_{\text{sp}} = \xi_1 J_z + \xi_2 J_x^2 + \xi_3 J_x, \quad (12)$$

and the respective oscillator Hamiltonian

$$H_{\text{bos}} = \xi_4 \cosh[\eta(a^\dagger - a)] + \Omega a^\dagger a + \xi_5 (a^\dagger + a). \quad (13)$$

The parameters ξ_1, ξ_2, ξ_3 (ξ_4, ξ_5) depend on the variational parameter η and are expectation values of various oscillator (spin) operators with respect to the oscillator state $|\chi\rangle$ (spin state $|\phi\rangle$). The states $|\phi\rangle$ and $|\chi\rangle$ are then given as the respective ground states of the effective Hamiltonians H_{sp} and H_{bos} . Due to the terms J_x^2 and $\cosh[\eta(a^\dagger + a)]$, $|\phi\rangle$ and $|\chi\rangle$ can not be spin or oscillator coherent states. Instead these states have to

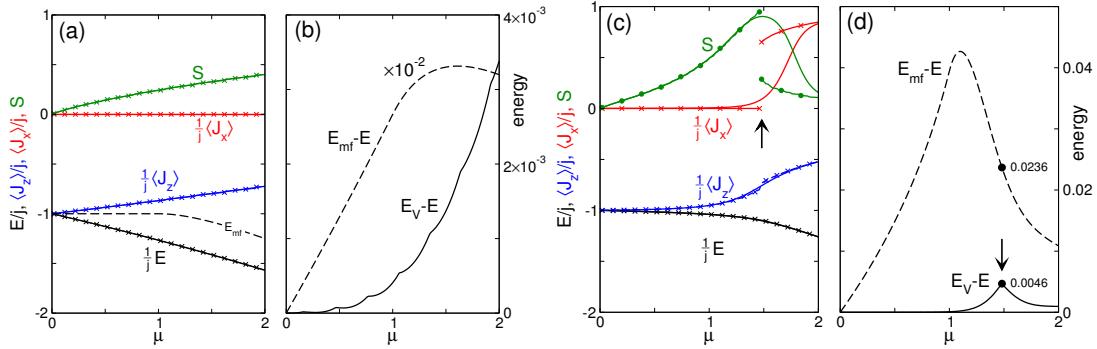


Figure 4: Comparison of the prediction of the variational ansatz with the true ground-state results from numerics, for $j = \frac{1}{2}$ (a,b) and $j = 5$ (c,d). In (a,c) the ground state energy E , the expectation values $\langle J_z \rangle$, $\langle J_x \rangle$ and the entanglement entropy S are displayed as a function of the coupling μ . Crosses indicate the variational results. In (b,d) we show the deviation $E_V - E$ ($E_{mf} - E$) of the variational energy E_V (the mean-field energy E_{mf}) from the true energy E . (Adapted from Article II)

be determined through a self-consistent computation of the respective ground states. In practice an iterative scheme is used to determine the ground states of H_{sp} and H_{bos} alternating, with the updated parameters ξ_1, ξ_2, ξ_3 and ξ_4, ξ_5 .

All results are obtained with the Hamiltonian $H_D + \epsilon J_x$ that includes a small symmetry-breaking term ϵJ_x , similar to the calculations with numerical diagonalization. With the given perturbation one of the symmetry-broken states for $\mu > 1$ and large j is selected, which makes convergence to the classical limit possible. In Fig. 4 we compare for $j = 1/2$ (left panel) and $j = 5$ (right panel) the prediction of the ansatz with the exact results for the expectation values $\langle H \rangle$, $\langle J_x \rangle$, $\langle J_z \rangle$ and the entanglement entropy S . For $j = 1/2$ the agreement between variational and exact results are very good. In particular the ansatz correctly predicts a vanishing order parameter $\langle J_x \rangle = 0$. The rise of the entropy for increased coupling μ shows that the inclusion of spin-oscillator entanglement in the ansatz through the unitary transformation is the key point in order to improve mean-field theory. Nevertheless the ansatz has a significant artefact, which is revealed at larger j as a jump in the curve for S and $\langle J_x \rangle$ and a kink for $\langle J_z \rangle$. This artefact is typical for the variational procedure and results out of the variational energy landscape. While for small and large coupling only one single minimum exists, in between two local minima exist, which switch the role of the global minimum such that a first order phase transition is predicted. Of course in reality such a transition can not occur, as described at the beginning of the section.

Further discussion on the artificial behavior of the variational ansatz and its behavior in the limits of the fast oscillator ($\Omega \rightarrow \infty$) or the large spin ($j \rightarrow \infty$) is given in Article II.

1.3 Regular dynamics of the Dicke model far and near the classical limit

Entanglement-driven collapse and revival We now turn to the dynamics of the Dicke model. We examine the phenomenon of collapse and revival (CR) of Rabi oscillations in the nonresonant case, i.e., for $\Omega \gg \Delta$ and $\Omega \ll \Delta$. Collapse and revival as described in the simpler Jaynes-Cummings model [Jaynes63] of one oscillator and one atom (a spin-1/2) at resonance, is a fundamental consequence of field quantization [Rempe87, Brune96]. It involves the generation of atom-field entanglement and non-classical Schrödinger cat states [Eberly80, Gea-Banacloche90]. For atomic ensembles with more than one atom CR has been discussed previously only in the rotating wave approximation (RWA) [Agarwal97, Klimov98], which is valid only near resonance.

In our analysis we examine the time evolution of the initial product state $|\psi(0)\rangle = |\theta_0\rangle \otimes |\alpha_0\rangle$ of a spin coherent state $|\theta_0\rangle$ and an oscillator coherent state $|\alpha_0\rangle$. For our calculations we set $|\alpha_0| \gg 1$, such that the oscillator is nearly classical. For the numerical time propagation we use the Chebyshev technique [Tal-Ezer84], keeping 10^3 bosons in the calculation to limit the error from the truncation of the bosonic part of the Hilbert space.

The emergence of the CR pattern in the observables $\langle J_{x/z}(t) \rangle$ is shown in Fig. 5 for different time scales. On the shortest time scale [panel (a)] both observables perform fast oscillations with the natural spin frequency Δ . On a longer time scale [panel (b)], oscillations in $\langle J_z(t) \rangle$ are modulated by oscillations with the natural oscillator frequency Ω . The latter are called Rabi oscillations since they arise from the coupling of the spin to a classical field. On the time scale of the first 5 to 10 oscillator periods $2\pi/\Omega$ [panel (c)] the collapse of the Rabi oscillations takes place. On the longest time scale considered [panel (d)] Rabi oscillations reappear with a revival time of $T_R/(2\pi/\Omega) \approx 100$ field oscillations. The emergence of CR is closely associated with the buildup of entanglement, which we measure with the entanglement entropy S as defined in the previous section. Starting with $S = 0$ for the initial product state, the entropy increases during the collapse phase up to its maximal possible value $\ln(2j + 1)$. The revival coincides with decreased S , since the wave function returns to the initial product form. A similar behavior is found for the oscillator (field) variance Δ_f , defined in Eq. (6) on page 2 in Article III.

The reduced state of oscillator and spin can be visualized by its respective Husimi function [Zhang90], which is by definition the probability of finding the oscillator or spin in a coherent state $|\alpha\rangle$ or $|\theta\rangle$. In Fig. 6 we show the oscillator Husimi function $Q_f(\alpha) = |\langle \alpha | \psi \rangle|^2$ corresponding to the spin dynamics shown in Fig. 5 at different times during the collapse phase. The Husimi function has several Gaussian peaks, which indicates a splitting of the initial coherent state into several coherent states, each rotating on a given circle in phase space. If some but not all coherent states merge, a partial revival occurs, e.g., at $t = T_R/2 \approx 50 \times (2\pi)/\Omega$, which confirms the behavior of the variance.

Perturbation theory Here we outline the explanation of the CR mechanism in the nonresonant Dicke model based on perturbation theory. The full derivation is given in Article III.

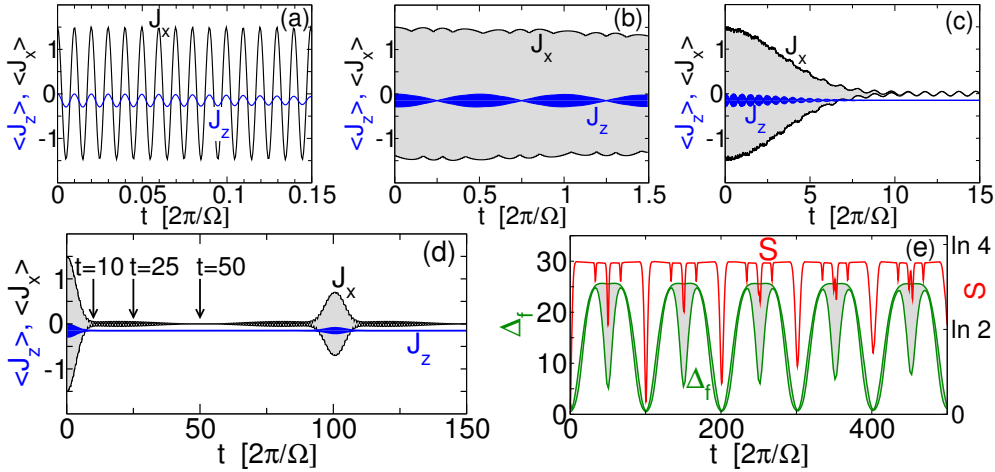


Figure 5: CR dynamics for $j = 3/2$, $\Omega/\Delta = 0.01$, $\lambda/\Delta = 0.01$ and $\theta_0 = \pi/2$, $\alpha_0 = 5$ for the initial state. (a)-(d): spin expectation values $\langle J_x(t) \rangle$ (black) and $\langle J_z(t) \rangle$ (blue) over different time scales, whereas panels (b)-(d) show the envelope of the fast spin oscillations. (e): entanglement entropy $S(t)$ (red) and field variance $\Delta_f(t)$ (green). (Adapted from Article III)

Standard non-degenerate perturbation theory up to second order provides correction to the eigenstates and eigenvalues of the noninteracting Hamiltonian, which can be expressed as

$$|\psi(t)\rangle_{(2)} = U^\dagger \exp[-i\tilde{H}t]U|\psi(0)\rangle, \quad (14)$$

for the perturbative wave function. The overall unitary time-evolution operator contains an effective Hamiltonian

$$\tilde{H} = -\Delta J_z + \Omega a^\dagger a - \omega_E(2a^\dagger a + 1)J_z - \omega_S J_z^2 \quad (15)$$

and a unitary transformation of states via

$$U = \exp \left[-\frac{2\omega_S}{\lambda}(a^\dagger - a)J_x - i\frac{2\omega_E}{\lambda}(a^\dagger + a)J_y \right], \quad (16)$$

where we have introduced the two frequencies

$$\omega_E = \frac{\lambda^2 \Delta}{2(\Delta^2 - \Omega^2)}, \quad \omega_S = \frac{\lambda^2 \Omega}{2(\Delta^2 - \Omega^2)}. \quad (17)$$

Because of its unitary form, the perturbative wave function remains valid for long times and large $|\alpha_0|$ as long as $\lambda|\alpha_0| \ll |\Delta^2 - \Omega^2|$. The central information about the nonresonant CR mechanism manifests in two opposite time scales. The “entangling” time $T_E = \pi/|\omega_E|$ is associated with the term $a^\dagger a J_z$ in \tilde{H} , which is the origin of the spin-dependent field splitting observed in Fig. 6. The “squeezing” time $T_S = \pi/|\omega_S|$ is interrelated to the term J_z^2 , which affects only the spin state and thus generates no additional entanglement, but squeezing of spin coherent states. The ratio $T_E/T_S = \Omega/\Delta$ determines which mechanism dominates the initial dynamics.

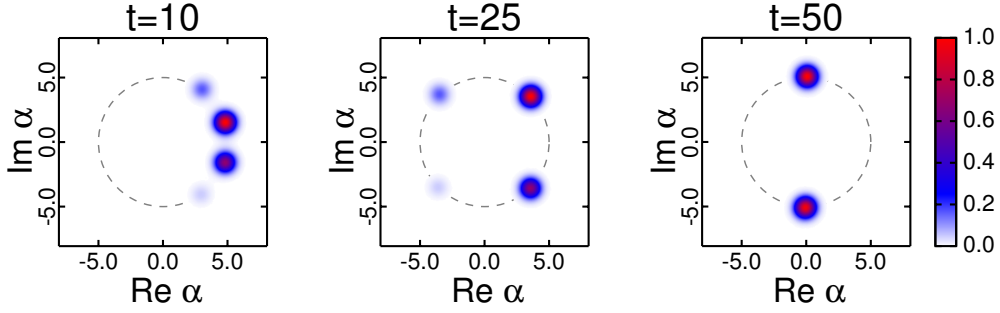


Figure 6: Oscillator Husimi function $Q_f(\alpha)$ for times $t/(2\pi/\Omega) = 10, 25, 50$ corresponding to the spin dynamics shown in Fig. 5. The radius of the dashed circle is given by the amplitude α_0 of the oscillator coherent initial state. (Adapted from Article III)

To further investigate the structure of the perturbative wave function one has to apply one after another of the unitary operators in Eq. (14) onto the initial product state $|\theta_0\rangle \otimes |\alpha_0\rangle$. We assume $|\alpha_0| \gg 0$ so we can substitute the operators $a^\dagger + a$ and $i(a^\dagger - a)$ in the unitary transformation U from Eq. (16) by the scalars $2 \operatorname{Re} \alpha_0$ and $2 \operatorname{Im} \alpha_0$. Then, U reduces to the spin rotation operator $R(a, b) = \exp[i(aJ_x - bJ_y)]$ with $(a, b \in \mathbb{R})$. Spin coherent states remain coherent under rotation, i.e., $U[|\theta_0\rangle \otimes |\alpha_0\rangle] = |\theta_0 + \delta\theta\rangle \otimes |\alpha_0\rangle$ with the angle $\delta\theta$ given in Eq. (20) on page 3 in Article III. The following application of $\exp[-i\tilde{H}t]$ rotates the oscillator component of each of the $(2j + 1)$ J_z -contributions $|m\rangle$ contained in the spin state. Since the operator $a^\dagger a$ rotates an oscillator coherent state according to $\exp[i\xi a^\dagger a]|\alpha\rangle = |\exp(i\xi)\alpha\rangle$, we get a spin-projected superposition of coherent states as given in Eq. (21) on page 3 in Article III. At the end the inverse transformation U^\dagger is applied, which leads again to a spin rotation, but now the arguments of $R(\cdot, \cdot)$ depend on the amplitudes of the spin-projected oscillator coherent states. The resulting rotated spin contributions $|\sigma_m(t)\rangle$ are given in Eq. (24) on page 4 in Article III. Putting all results together, the structure of the perturbative wave function $|\psi(t)\rangle_{(2)}$ is given as

$$|\psi(t)\rangle = \sum_{m=-j}^j \psi_m(t) |\sigma_m(t)\rangle \otimes |\alpha_m(t)\rangle, \quad (18)$$

with a set of spin states $|\sigma_m(t)\rangle$ and oscillator coherent states $|\alpha_m(t)\rangle$.

Explicit expressions for spin and oscillator expectation values follow easily from the given form of the wave function. As shown in Article III these perturbative results are in excellent agreement with the exact results obtained from numerics. In addition a qualitative understanding of CR in perturbation theory can be obtained from the derived expressions. In the following we consider the case $\Omega \ll \Delta$. In the initial dynamics for $t \ll T_E, T_S$ differences between the coherent state parameters $\alpha_m(t)$ are negligible and the wave function has the product form $|\psi(t)\rangle \approx |\sigma(t)\rangle \otimes |\alpha_0 e^{-i\Omega t}\rangle$. The spin state $|\sigma(t)\rangle$ is obtained from $|\theta_0\rangle$ through three rotations around different axes, the rotation with the spin operator R , the rotation from the effective Hamiltonian as $\exp[it\Delta J_z]$, and then again from R which presently does not depend on m . The spin part of the wave function thus remains coherent, which leads to the described Rabi oscillations. For times $t \sim T_E \ll T_S$ the term $a^\dagger a J_z$ becomes important, leading to

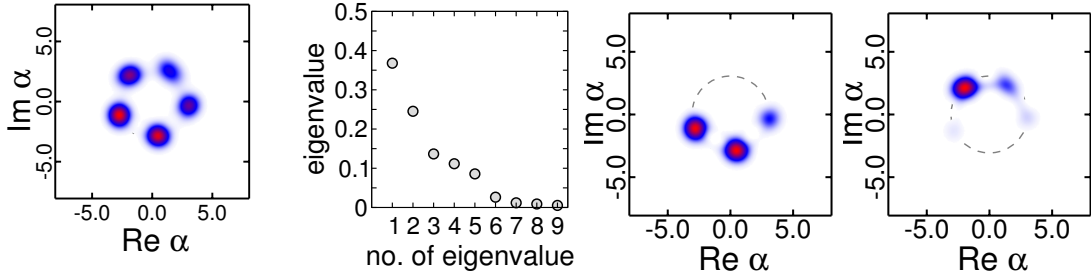


Figure 7: Emergence of oscillator cat states for $\Omega/\Delta = 0.05$, $\lambda/\Delta = 0.02$, $j = 10$, and $\theta_0 = \pi/4$, $\alpha_0 = 3$. 1st panel: $Q_f(\alpha)$ at $t/(2\pi/\Omega) = 25$. 2nd panel: Schmidt coefficients. 3rd and 4th panel: $Q_f(\alpha)$ of the two largest contribution in the Schmidt decomposition with weight 0.37 and 0.25. (Adapted from Article III)

the splitting of the initial coherent oscillator state $|\alpha_0\rangle$ into $2j + 1$ coherent states $|\alpha_m\rangle$. Because different $|m\rangle$ -states are orthogonal, the oscillator is in an incoherent superposition. The collapse of Rabi oscillations is a consequence of the decreasing overlap $|\langle\alpha_m(t)|\alpha_{m'}(t)\rangle| = \exp[-|\alpha_0|^2(1 - \cos \delta\alpha_{mm'})]$ with $\delta\alpha_{mm'} = 2\pi(m - m')(t/T_E)$. From this equation and the explicit form of $\alpha_m(t)$ given in Eq. (22) on page 4 in Article III we observe that periodic revivals occur at multiples of the entangling time T_E .

Schrödinger cat states Closely associated with the collapse of the wave function is the generation of spin and oscillator cat states. These states appear as linear combinations of well-separated spin or oscillator coherent states, e.g., $|\alpha\rangle \pm |-\alpha\rangle$ for $|\alpha| \gg 1$. An example of such a superposition of oscillator coherent states is given in the leftmost panel of Fig. 7, which shows the Husimi function $Q_f(\alpha)$ of the oscillator state at the beginning of the collapse phase. In order to check if the superposition is coherent, we decompose the wave function into mutually orthogonal states according to the Schmidt decomposition [Horodecki09]. The corresponding eigenvalues are shown in the second panel of Fig. 7, indicating five relevant contributions. The Husimi function of the two greatest eigenvalues are shown in the two most right panels of Fig. 7. Field cat states can be identified in both components, showing that the field superposition is partially coherent. This result is already anticipated by the perturbative wave function. If the spin states $|\sigma_m(t)\rangle$ in Eq. (18) were mutually orthogonal the field superposition seen in Q_f would be completely incoherent. However, these states are not orthogonal due to the rotation with U^\dagger , which allows for a coherent superposition and the appearance of field cat states.

Collapse and revival and the classical field limit We now turn to the dynamics exactly at and near the classical limit of the Dicke model. First we derive the semiclassical (SC) equations of motion, which become exact in the CS ($j \rightarrow \infty$) and CO ($\Omega \rightarrow 0$) limit. One way to obtain the SC equations is to start with the Ehrenfest equations of motion $d\langle A \rangle/dt = i\langle [H, A] \rangle$ for the spin (J_x, J_y, J_z) and oscillator ($a^{(\dagger)}$) observables. In the SC approximation spin-oscillator correlations are neglected [Graham84], i.e., mixed operator products are substituted according to e.g., $\langle (a^\dagger + a)J_z \rangle \mapsto \langle a^\dagger + a \rangle \langle J_z \rangle$. This

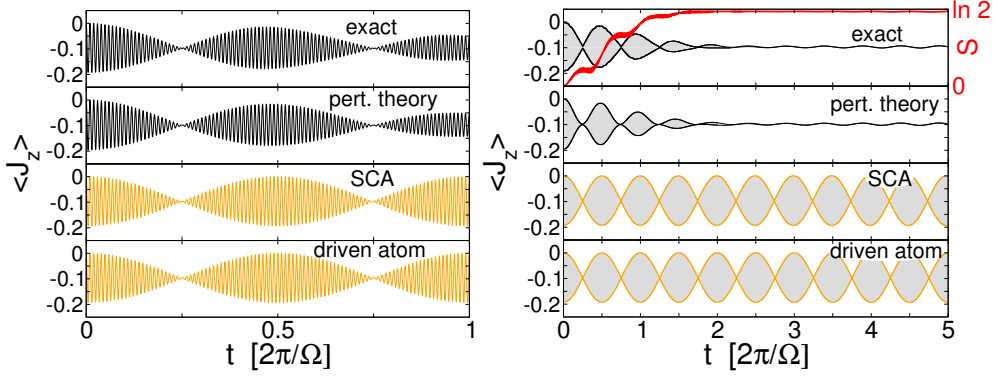


Figure 8: Comparison of the exact dynamics from numerical diagonalization with the prediction from perturbation theory, the SC approximation and the driven spin (atom) model for $j = 1/2$, $\Omega/\Delta = 0.01$, $\lambda/\Delta = 0.02$ and $\theta_0 = \pi/2$, $\alpha_0 = 5$. Left panel: All four descriptions agree for short times. Right panel: Only perturbation theory is capable to correctly predict the collapse while the entanglement entropy $S(t)$ (red) increases. (Adapted from Article III)

results into the SC equations of motion

$$\partial_t \mathbf{J} = \mathbf{B}(\alpha) \times \mathbf{J}, \quad i\partial_t \alpha = \Omega\alpha + \lambda\langle J_x \rangle. \quad (19)$$

While the oscillator evolves under the influence of an external force $\lambda\langle J_x \rangle$, the spin is driven by an effective magnetic field $\mathbf{B}(\alpha) = (2\lambda \text{Re } \alpha, 0, \Delta)$ which depends on the oscillator state α . A second method to obtain the SC equations (19) illustrates the resemblance with the mean-field description of the QPT in Section 1.2. The SC approximation of neglecting spin-oscillator correlations is equivalent to the assumption that the coupled spin-oscillator system remains in the product state $|\psi_{\text{SC}}\rangle = |z(t)\rangle \otimes |\alpha(t)\rangle$, with the complex valued amplitude $z = e^{-i\phi} \tan(\theta/2)$ for the coherent spin state. The time dependence of $|\psi_{\text{SC}}\rangle$ follows from the Dirac-Frenkel time-dependent variational principle [Dirac30, Frenkel34]. The equation of motion is

$$\frac{d}{dt} |\psi_{\text{SC}}\rangle = \mathcal{P} \frac{1}{i} H |\psi_{\text{SC}}\rangle, \quad (20)$$

where \mathcal{P} is the orthogonal projection onto the tangent space of the manifold of $|\psi_{\text{SC}}\rangle$ states. Evaluation of the projection gives the equations of motion (19).

We now consider the limit $\Omega \rightarrow 0$ of the classical oscillator with negligible energy quantization. Since CR for $\Omega \ll \Delta$ does not depend on the nonclassical properties of a quantized field, but only on the possibility of atom-field entanglement, one would expect the collapse of Rabi oscillations also in the classical oscillator limit. This limit can also be defined as the limit $|\alpha_0| \rightarrow \infty$, keeping $\lambda|\alpha_0|$ constant. Then, the oscillator evolves independently of the spin because the strength of the influence of the spin on the field given by $\lambda\langle J_x \rangle$ goes to zero for $\lambda \rightarrow 0$ and finite j . However the influence of the field on the spin given by $\lambda\langle a + a^\dagger \rangle$ remains finite. Then, the Dicke model reduces to the model of a spin driven by the external field $\mathbf{B}(t) = (2\lambda\alpha_0 \cos \Omega t, 0, -\Delta)$. The

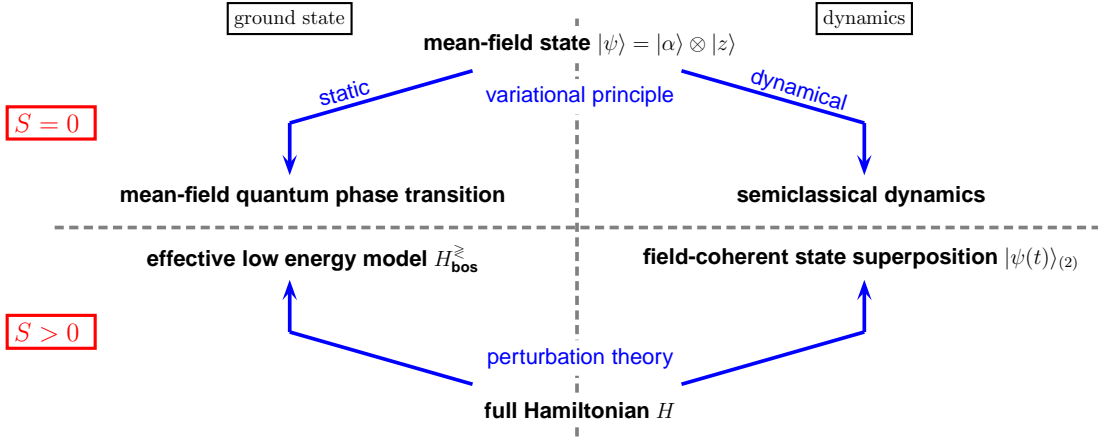


Figure 9: Schematic diagram of the mean-field description and perturbation theory for the Dicke ground state and dynamics. The mean-field QPT and semiclassical dynamics follow from variational calculations from the coherent product state, which entirely neglects quantum entanglement and fluctuations. Perturbation theory accounts for the leading order of quantum corrections, featuring e.g., the criticality of oscillator fluctuations close to the QPT in the CO limit and the entanglement-driven CR mechanism in the dynamics.

spin expectation values $\mathbf{J} = (\langle J_x \rangle, \langle J_y \rangle, \langle J_z \rangle)$ obey the equations of motion

$$\partial_t \mathbf{J} = \mathbf{B}(t) \times \mathbf{J}. \quad (21)$$

The SC equations of motion (19) reduce to the Eqs. (21) in the classical oscillator limit. In Fig. 8 we contrast the results from numerical exact propagation, the semiclassical equations, perturbation theory, and from the simplified Eqs. (21) of the driven spin. For short times (left panel) all four descriptions agree and show Rabi oscillations, which are characteristic for classical field dynamics. For longer times (right panel), significant entanglement is generated over the first few periods of the natural oscillator frequency Ω . Since the SC approximation relies on the product state assumption, it cannot account for entanglement and consequently misses the collapse of Rabi oscillations. In particular the SC approximation does not even improve the results from the model in Eq. (21) with entire classical field dynamics. However perturbation theory provides the correct result.

Figure 9 summarizes our explanations on the mean-field description of dynamics and the ground state of the Dicke model and the perturbative approach to include quantum correlations and entanglement. The mean-field state $|\alpha\rangle \otimes |z\rangle$ contains all information on the ground state and the dynamics, emerging exactly in the classical limit. The ground state featuring the QPT is obtained by means of the standard (“static”) variational principle. The dynamics of the classical model is derived by means of the Dirac-Frenckel (“dynamical”) variational principle. In each case the mean-field description neglects quantum correlations and entanglement between spin and oscillator. However, as pointed out in the previous sections, close to the classical limits quantum fluctuations can become significant in the dynamics and even critical in the ground

state. To account for these quantum corrections we apply perturbation theory. In that way we obtain an effective low energy model H_{bos}^{\leq} for the ground state, which gives the diverging oscillator variance at the critical coupling. For the dynamical case, we derive a perturbative wave function $|\psi(t)\rangle_{(2)}$ as a superposition of nearly classical field states, each “tagged” with an associated spin configuration. We are able to construct this state as a sequence of unitary time-evolution operators applied to the initial product state. This structure makes it possible to distinguish between different mechanism of CR, i.e., entanglement generation for $\Omega \ll \Delta$ and spin squeezing for $\Omega \gg \Delta$.

Classical and quantum collective modes The buildup of entanglement during CR for $\Omega \ll \Delta$ hinders to follow the dynamics of quantum observables into the classical limit. For a direct comparison of quantum and classical dynamics more adequate measures have to be applied. We start with the dynamics in the vicinity of the stationary solutions of the classical equation of motion (19) and compare the collective response of the Dicke model for small perturbations of the ground state in the classical and quantum regime. In Section 1.2 the stationary solution is stated, which gives the ground state in the CS and CO limit. We now consider small (complex valued) oscillations $z = z_s + \delta z$, $\bar{\alpha} = \bar{\alpha}_s + \delta \bar{\alpha}$ around a stationary solution. The deviations $\delta \bar{\alpha}$, δz satisfy a linear equation of motion, which is shown in detail in Article IV. The full dynamical response to the perturbation is given by the set of eigenvalues and eigenvectors of this equation. It reveals the existence of two collective modes with frequencies ω_{\pm} and weights w_{\pm} . The frequency ω_{-} of the lower mode vanishes at the critical coupling $\mu = 1$, which signals the second order QPT. The frequencies obtained from the SC equations were derived previously by means of the Holstein-Primakoff transformation of the spin operators in Ref. [Emary03a].

For the quantum regime we proceed in a similar manner to the classical case. We slightly disturb the ground state and determine the time evolution of the wave function. The initial state is given as the ground state, rotated around the y -axis according to $|\psi_{\delta}\rangle = S(\delta\theta)|\psi_0\rangle$ with $S(\theta) = e^{i\theta J_y}$ and $\delta\theta \ll 1$. From the linearization of the expectation value $\langle \psi_{\delta}(t) | J_x | \psi_{\delta}(t) \rangle$ for small $\delta\theta$ we identify the commutator Green function

$$\langle \langle J_x(t); J_y \rangle \rangle = i \langle \psi_0 | [J_x(t), J_y] | \psi_0 \rangle, \quad (22)$$

as the relevant quantity for the comparison with the SC result. We compute the Fourier transform $\langle \langle J_x; J_y \rangle \rangle_{\omega}$ of the Green function with the Kernel Polynomial Method [Weiße06] which allows us to treat large j . As for the Chebyshev time propagation technique, up to 10^3 bosons are kept in the bosonic part of the Hilbert space to limit the error from truncation. As shown in full detail in Article IV, the Green function consists of several peaks, whereas a pair of two peaks close to the classical frequencies $\pm\omega_{\pm}$ dominate the spectrum already for low j . For a quantitative comparison with the classical limit, we show in Fig. 10 the peak positions and weights as extracted from the Green function for $j = 10$. Already for this rather low spin length we observe that the position of the peaks with the most weight are located close to the classical frequencies ω_{\pm} . As shown in Fig. 3 on page 4 in Article IV the quantum mechanical Green function indeed converges with increased j to the result in the classic limit, in the sense that the weight

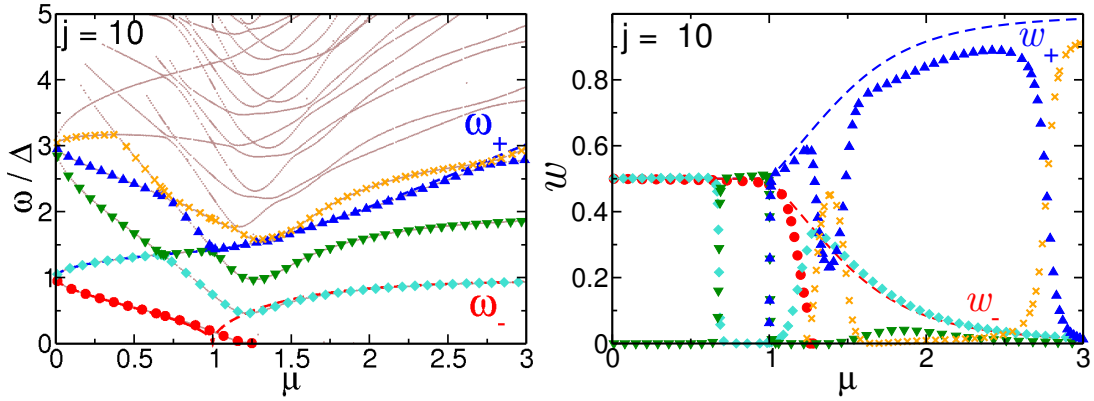


Figure 10: Position (left panel) and weight (right panel) of peaks in the Green function $\langle\langle J_x; J_y \rangle\rangle_\omega$ for $\Omega/\Delta = 1$ and $j = 10$. The dashed lines show the frequencies ω_\pm and weights w_\pm of the classical collective modes. The quantum excitation spectrum is characterized by a huge number of branches with avoided crossings. Those branches of the spectrum which gain significant spectral weight are accentuated by different colored symbols. (Adapted from Article IV)

of the dominant peaks increases and its position shifts towards the frequencies $\pm\omega_\pm$ of the classical collective modes.

1.4 Route to chaos in Dicke and optomechanical systems

We now turn to the general nonequilibrium dynamics at higher energy and large coupling. In this regime the classical dynamics is distinguished by the onset of chaotic motion. In the quantum case additional corrections beyond the leading order of the SC approximation arise, e.g., from quantum diffusion in phase space.

Here we outline a comparative analysis of Hamiltonian chaos for the Dicke model and driven dissipative chaos for the optomechanical system. For the Dicke model the classical dynamics is given by the SC equations derived in the previous section. For the dissipative dynamics of the optomechanical system we have to start from the quantum-optical Master equation

$$\frac{d\rho}{dt} = -i[H_O, \rho] + \Gamma\mathcal{D}[b, \rho] + \kappa\mathcal{D}[a, \rho], \quad (23)$$

for the density matrix $\rho(t)$. The dissipative terms given in Lindblad form,

$$\mathcal{D}[L, \rho] = L\rho L^\dagger - \frac{1}{2}(L^\dagger L\rho + \rho L^\dagger L) \quad (24)$$

for $L \in \{a, b\}$, account for radiative cavity losses ($\propto \kappa$) and cantilever damping ($\propto \Gamma$). We assume zero bath temperature. The relevant parameters entering the dynamics are the laser-cavity detuning Δ/Ω , the pump parameter $P = 8\alpha_L^2 g_0^2 / \Omega^4$, and the quantum-classical scaling parameter $\sigma = g_0 / \kappa$. The scaling parameter can equally be written as $\sigma = x_{\text{zpt}} / x_{\text{res}}$ and then relates the zero-point fluctuations $x_{\text{zpt}} = \sqrt{\hbar / (2m\Omega)}$ of the cantilever (with mass m) to the resonance width x_{res} of the cavity [Ludwig08].

While x_{res} is a classical quantity, which characterizes the cavity quality, x_{zpt} is of order $\hbar^{1/2}$ such that σ vanishes for $\hbar \rightarrow 0$. Variation of σ thus allows us to follow how the quantum dynamics of the optomechanical system evolves towards the classical dynamics in the bad-cavity limit $\sigma \ll 1$. The SC equations now follow from the equation of motion for the expectation values $d/dt \langle A \rangle = \text{Tr}(A d\rho/dt)$ for $A \in \{a, b\}$. Similar to the SC equations for the Dicke model we now apply the SC approximation by neglecting quantum correlations, e.g., $\langle (b^\dagger + b) a \rangle \approx \langle b^\dagger + b \rangle \langle a \rangle$ and obtain

$$\frac{d\alpha}{d\tau} = -i \left[\frac{\Delta}{\Omega} \alpha - (\beta + \beta^*) \alpha - \frac{1}{2} \right] - \frac{\kappa}{2\Omega} \alpha, \quad (25)$$

$$\frac{d\beta}{d\tau} = -i \left[\frac{P}{2} |\alpha|^2 + \beta \right] - \frac{\Gamma}{2\Omega} \beta \quad (26)$$

for the rescaled cavity and cantilever amplitude $\alpha = (\Omega/(2\alpha_L)) \langle a \rangle$, $\beta = (g_0/\Omega) \langle b \rangle$ with the rescaled time $\tau = \Omega t$.

Classical Hamiltonian and dissipative chaos Depending on initial conditions and system parameters classical orbits are either regular or chaotic. The stability of classical orbits is distinguished by means of the maximal Lyapunov exponent $\Lambda(t)$ for $t \rightarrow \infty$, which we calculate with the “standard method” [Benettin80a, Benettin80b]. The sum over all Lyapunov exponents is equal to the divergence of the vector field $\partial g_k / \partial x_k$ of the respective dynamical system, $dx_k/dt = g_k(x_n)$ written in “standard” form. The sum thus vanishes for the Hamiltonian Dicke system and equals $-(\kappa + \Gamma)/\Omega$ for the driven dissipative optomechanical system.

Due to energy conservation the Dicke model is effectively a four-dimensional Hamiltonian system and the Lyapunov exponents appear in two pairs $\pm\Lambda_1(t)$, $\pm\Lambda_2(t)$. Since motion along the orbit is stable, two exponents $\pm\Lambda_2(t)$ always vanish. Therefore regular and chaotic motion is distinguished by the remaining exponent $\Lambda_1(t)$, which vanishes in the limit $t \rightarrow \infty$ for a regular orbit, while $\Lambda_1(t) > 0$ for a chaotic orbit. For given energy E the global structure of phase space can be visualized by means of Poincare plots as given in the left panel of Fig. 11. Plotted are the values $J_x(t)$, $J_y(t)$ at those times where the orbit intersects the plane $Q(t) = \text{Re} \bar{\alpha}(t) = 0$. For small coupling the whole accessible area of the Poincare plot is covered by invariant curves, corresponding to quasiperiodic motion. Increasing the coupling, the “chaotic sea” emerges and eventually covers the whole area for sufficiently strong coupling.

In the optomechanical system the simplest regular orbits are given by cantilever oscillations $x(\tau) = \bar{x} + \cos(\Omega\tau)$ with the static displacement \bar{x} and the natural cantilever frequency Ω . Beyond a certain driving strength a period-doubling bifurcation (PDB) occurs and a new limit cycle with twice the period emerges. While the maximal Lyapunov exponent is negative for periodic motion, it vanishes at the point of the PDB. Increasing the coupling further additional PDBs occur, leading to multi-periodic limit cycles. Eventually chaotic motion occurs, which is indicated by a positive Lyapunov exponent. The route to chaos is illustrated by bifurcation diagrams as given in the right panel of Fig. 11. We plot the observed amplitudes extracted from the numerical solution as shown in Article V. The up-spring of subsequent branches in the bifurcation

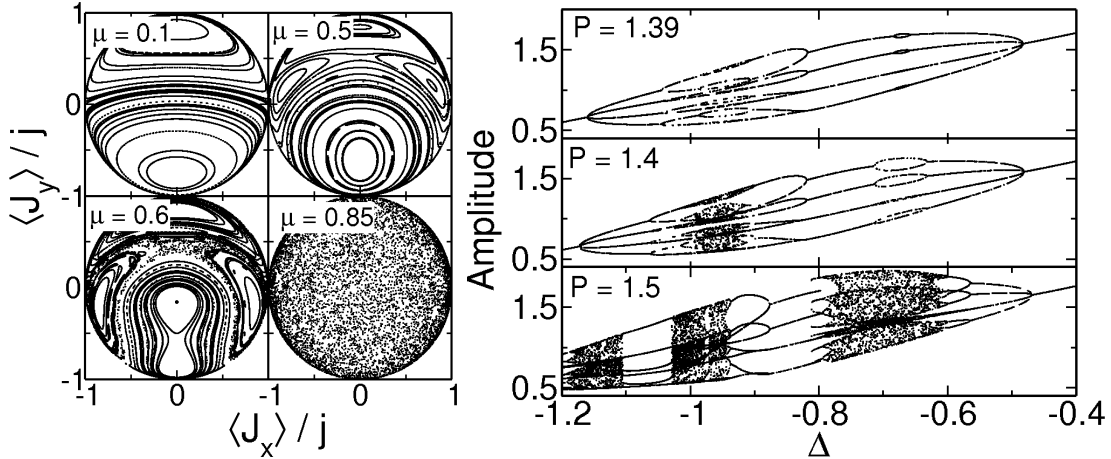


Figure 11: Route from classical regular motion to chaotic dynamics. Left: Poincare plots for energy $E = -0.5$ and increasing coupling for the Dicke model. Right: bifurcation diagram of the limit cycle amplitude for increasing driving for the optomechanical system. (Adapted from Article IV and V)

diagram shows PDBs leading into the chaotic regions. With increased driving more and more complex intertwined sequences of windows of regular and chaotic dynamics emerge.

Signatures of chaos in quantum dynamics I: Dicke model We now turn to the quantum dynamics and begin with the Dicke model. Quantum trajectories start from the initial state $|\psi(0)\rangle = |\alpha(0)\rangle \otimes |z(0)\rangle$ which correspond to the initial conditions from the respective classical orbit. As shown in Article IV classical and quantum trajectories – the latter are given by the expectation values $(\langle J_x(t) \rangle, \langle J_y(t) \rangle)$ – agree only over a short time period, the Ehrenfest time T_{Eh} . Convergence of the quantum to classical trajectory, which is equivalent to an increasing of T_{Eh} for increased j is slow or absent. Coincidence of classical and quantum orbits is given only as long as the wave function approximately remains in the product state form. However classical drift and quantum diffusion change significantly the form of the wave function.

A better comparison of classical and quantum time evolution is thus given by phase space functions, e.g., the spin Husimi function $Q(\theta, \phi; t) = |\langle \theta, \phi | \psi(t) \rangle|^2$. The Husimi function for a coherent state covers a phase space volume $\propto 1/j$ and thus $Q(\theta, \phi; \cdot)$ strikes to a point in the limit $j \rightarrow \infty$. The time evolution of the joint spin-oscillator Husimi function $Q(z, \alpha; t)$ is determined by a Fokker-Planck equation with a classical drift and a quantum diffusion term [Altland12a, Altland12b]. The latter vanishes in the CS limit and the Husimi function reduces to a classical probability function which obeys the Liouville equation. Therefore convergence of the quantum to the classical dynamics is observed in the way that the spin Husimi function traces out the phase space region which is accessible to the classical orbits. This is illustrated for a regular orbit in the first and second panel of Fig. 12. For a point of time T far beyond T_{Eh} we plot the $(\langle J_x(t) \rangle, \langle J_y(t) \rangle)$ -trajectory in the time interval $[0, T]$ and the Husimi function at time T . The quantum trajectory has lost all resemblance to the classical trajectory and is given as a spiral to the origin showing the collapse of the wave function. However

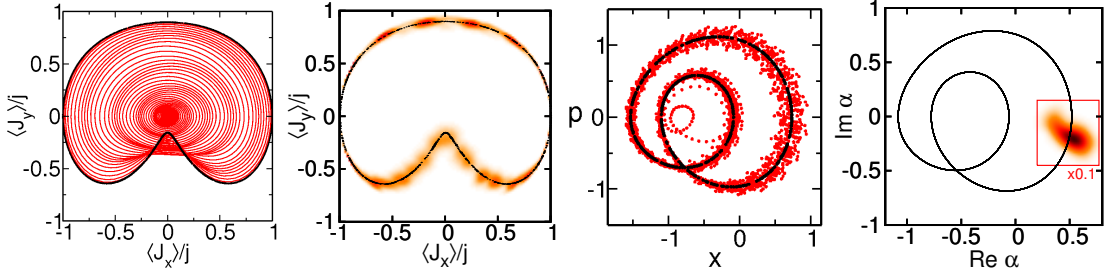


Figure 12: Delocalization of a wave function in the Dicke model vs. localization of an Monte Carlo wave function in the optomechanical system. 1st panel: quantum (red, $j = 400$) and classical (black) trajectory of the Dicke model for $\Delta/\Omega = 1$, $\mu = 0.6$ and $\langle J_x(0) \rangle = 0$, $\langle J_y(0) \rangle = 0.9$ from $t = 0$ until $t/(2\pi/\Delta) = 200$. 2nd panel: corresponding spin Husimi function at $t/(2\pi/\Delta) = 200$. 3rd panel: stroboscopic plot of a quantum (red, $\sigma = 0.01$) and classical (black) trajectory of the optomechanical system for $\Delta/\Omega = -0.85$, $P = 1.5$, $\kappa/\Omega = 1$, $\Gamma/\Omega = 0.001$ from $t = 0$ until $t/(2\pi/\Omega) = 150$. 4th panel: corresponding oscillator Husimi function of the cantilever at $t/(2\pi/\Omega) = 150$. Note that the size of the Husimi function is increased by a factor of 10 to enable visibility.

the Husimi function is tacked to the classical trajectory. Due to classical phase-space drift and quantum diffusion the quantum state spreads along but not perpendicular to the classical orbit.

The same mechanism performs also in the case of chaotic orbits. However in that case the classical trajectory passes through the whole phase space and so does the Husimi function. Furthermore the classical drift in the unstable direction dominates the dynamics leading to an Ehrenfest time which scales as $T_{\text{Eh}} \sim \Lambda^{-1} \ln(1/V)$ [Schubert12], with the maximal Lyapunov exponent Λ and the initial occupied phase space volume V . In contrast, for a regular orbit the slow quantum diffusion along the orbit dominates the Ehrenfest time, which then scales as $T_{\text{Eh}} \sim 1/\sqrt{V}$. We can quantify the spreading of the quantum state by means of the spin variance $\Delta J_{\parallel} = \langle J_{\parallel}^2 \rangle - \langle J_{\parallel} \rangle^2$ of a rotated spin operator $J_{\parallel} = \mathbf{n} \cdot \mathbf{J}$ which is minimized over all the possible directions $\mathbf{n} = (n_x, n_y, n_z)^T$ with $|\mathbf{n}| = 1$. The spin variance is invariant under rotation. It is $\Delta J_{\parallel} \geq 0$, and $\Delta J_{\parallel} = 0$ precisely for a spin coherent state. We show ΔJ_{\parallel} in Fig. 13 for quantum trajectories with small ($j = 2$) and large ($j = 400$) spin length, corresponding to a classical regular and a chaotic orbit. For $j = 2$ the variance behaves similarly for both orbits. However for $j = 400$ the variance and thus the Ehrenfest time of the regular vs. chaotic orbit scales differently. While for the regular orbit the variance is significantly reduced, for the chaotic orbit it again grows fast and saturates at a level not much smaller than that for $j = 2$.

The filling of the entire energy shell of the Husimi function for a chaotic orbit can be understood as a signature of microcanonical thermalization [Altland12a, Altland12b]. Nevertheless time evolution of the Hamiltonian Dicke model is reversible and the initial coherent state reappears due to the CR mechanism which is shown in Section 1.3. In order to attain true irreversibility and the approach to an stationary equilibrium state, one has to include the coupling to an environment as in the case of the optomechanical system.

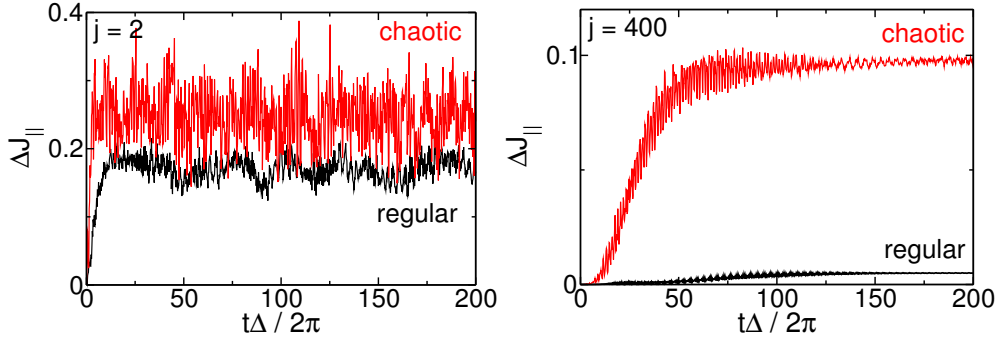


Figure 13: Spin variance ΔJ_{\parallel} as a function of time for a quantum trajectory with $j = 2$ (left) and $j = 400$ (right) corresponding to a classical regular and chaotic orbit. (Adapted from Article IV)

Signatures of chaos in quantum dynamics II: optomechanical model Here nonlinear signatures emerge in the quantum dynamics close to the bad-cavity limit $\sigma \ll 1$. In this regime the photon and phonon mode are occupied up to high boson numbers ($\langle a \rangle, \langle b \rangle \sim 10^3$), which makes it impossible to directly solve the master equation (23) (e.g. via Runge-Kutta type integrators). Instead we use the Monte Carlo (MC) method of quantum state diffusion (QSD) [Diosi88, Gisin92], in which the density matrix $\rho(t)$ is unraveled in a classical ensemble of pure states. The time evolution of the MC state is governed by a stochastic differential equation, which is given in its differential Itô form by

$$\begin{aligned}
 |d\psi\rangle = & -iH_0|\psi\rangle dt + \sum_j \left(\langle L_j^\dagger \rangle L_j - \frac{1}{2} L_j^\dagger L_j - \frac{1}{2} \langle L_j^\dagger \rangle \langle L_j \rangle \right) |\psi\rangle dt \\
 & + \sum_j (L_j - \langle L_j \rangle) |\psi\rangle d\xi_j,
 \end{aligned} \tag{27}$$

with $\langle L_j^{(\dagger)} \rangle = \langle \psi | L_j^{(\dagger)} | \psi \rangle$ and $L_j \in \{a, b\}$. While the first term depicts unitary time propagation caused by the Hamiltonian, the second and third term describe the influence of the environment resulting in a drift of the state vector and random fluctuations. The independent complex differential random variables $d\xi_j$ represent a complex normalized Wiener process and satisfy

$$\text{M} d\xi_j = \text{M} d\xi_i d\xi_j = 0, \quad \text{M} d\xi_i^* d\xi_j = \delta_{ij} dt, \tag{28}$$

where M denotes the ensemble mean. The density operator is then obtained as the mean over the pure state projectors, i.e. $\rho(t) = \text{M} |\psi(t)\rangle \langle \psi(t)|$. In our work we apply the QSD implementation of Schack and Brun [Schack97]. One advantage of QSD over other unraveling methods, e.g., the quantum jump method [Mølmer93], is the dynamical localization of the quantum trajectories on classical orbits [Schack95, Rigo96, Strunz98]. Taking advantage of dynamical localization, QSD was previously applied to study the classical limit of quantized Duffing-type oscillators [Spiller94, Brun96, Kryuchkyan02] and models for second harmonic generation [Zheng95].

Dynamical localization is in strong contrast to the delocalization of the wave function

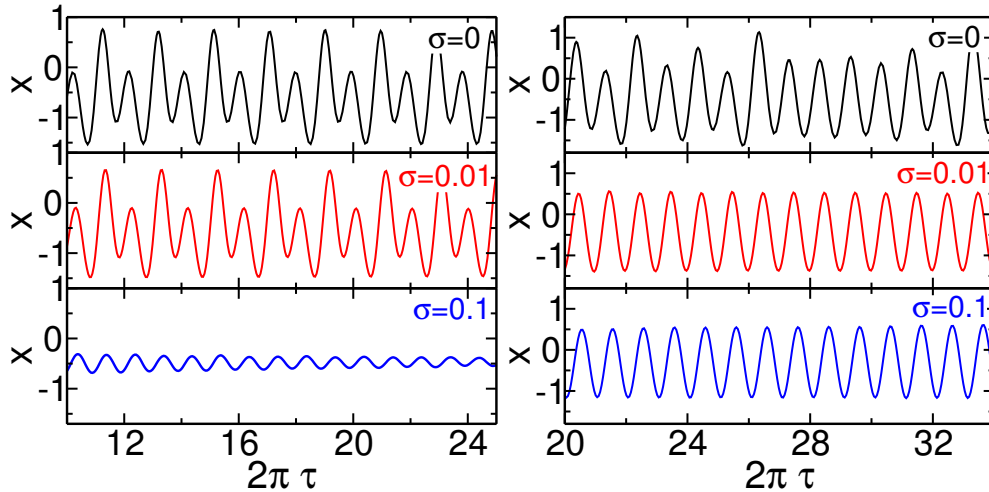


Figure 14: Comparison of the SC dynamics ($\sigma = 0$) of the cantilever position $x(\tau)$ with the corresponding quantum dynamics from the ensemble average of 5000 MC quantum trajectories ($\sigma > 0$). The figures present the case of a classical period-2 orbit (left panel with $\Delta = -0.85$) and a chaotic orbit (right panel with $\Delta = -0.7$). In each case $P = 1.5$, $\kappa/\Omega = 1$, $\Gamma/\Omega = 0.001$. (Adapted from Article V)

of a Hamilton system as shown in the third and fourth panel of Fig. 12. For a sufficient low scaling parameter σ the quantum trajectory localizes on the classical limit cycle as observed in the stroboscopic plot in the third panel. Correspondingly the phase space density of the MC wave function, i.e., the Husimi function remains strongly coherent during the time propagation.

The localization properties of MC trajectories are also found in the ensemble average from which experimentally accessible quantities can be obtained. As an example we show in Fig. 14 the time evolution of the cantilever position $x(\tau)$ after the initial transient has faded out. The figure depicts for a classical ($\sigma = 0$) regular period-2 orbit and a chaotic orbit the corresponding quantum dynamics for two different values of the scaling parameter σ . As a principal result we observe that quantum mechanics favors simple periodic motion which does not need to have a classical counterpart. This is clearly observed for the case $\sigma = 0.1$. The crossover from classical to period-1 motion depends on the complexity of the classical attractor. So, closer to the classical limit ($\sigma = 0.01$) quantum dynamics agrees with classical dynamics only for simple trajectories like the period-2 orbit shown in the figure. For the classically chaotic orbit, however, the quantum trajectory shows simple period-1 oscillations even close to the classical limit.

1.5 Conclusions

Modern cavity QED and cavity optomechanical systems realize the interaction of light with mesoscopic devices, which exhibit discrete (atom-like) energy spectra or perform micromechanical motion. Due to the large variety of experimental systems which cover several orders of the coupling strength and the size of the material subsystem, fundamental questions concerning the coupling of a truly quantum system – the cavity light

field – to a potentially classical system can be addressed. In this thesis we have studied the crossover from the quantum regime to the classical limit of two prototypical models, the Dicke model and the generic optomechanical model. The physical problems considered in this approach range from a ground state phase transition, its dynamical response to general nonequilibrium dynamics including Hamiltonian and driven dissipative chaotic motion.

The classical limit of these models follows from the classical limit of at least one of its subsystems, i.e., the atomic (spin) system, the photon mode of the cavity or the phonon mode of the cantilever. The classical equations of motion result from the respective quantum equations through the application of the semiclassical approximation, i.e., the neglect of quantum correlations. The approach of the results from quantum mechanics to the prediction of the classical equations can be obtained by subsequently decreasing the respective scaling parameter, i.e., the inverse spin length or the photon frequency for the Dicke model, or the ratio of the photon-phonon coupling parameter over the inverse photon lifetime for the optomechanical system. In this way the bosonic modes attain high occupation, which requires consideration of an increasing number of oscillator number states in Hilbert space. In order to obtain exact results we have utilized advanced numerical methods, e.g., the Lanczos diagonalization method for ground state calculations, the Kernel Polynomial Method for dynamical response functions, Chebyshev recursion for time propagation, and quantum state diffusion for open system dynamics.

In Article I we have studied the quantum phase transition of the Dicke model in the classical oscillator limit. Our work shows that in this limit the transition occurs already for finite spin length but with the same critical behavior as in the classical spin limit. We have derived an effective model for the oscillator degrees of freedom and have discussed the differences of both classical limits with respect to quantum fluctuations around the mean-field ground state. Furthermore the spin-oscillator entanglement remains small in the classical oscillator limit, while it diverges at the transition in the classical spin limit. In this article we have depicted also the limit of the high-frequency oscillator. Here, in contrast to the classical oscillator limit, the spin degrees of freedom are described by the Lipkin-Meshkov-Glick model. For the special case of a spin one-half, an alternative limit can be defined which then replaces the quantum phase transition by spin frequency renormalization.

In Article II we have proposed a variational ansatz for the Dicke model which extends the mean-field description through the inclusion of spin-oscillator correlations. The ansatz becomes correct in the limit of large oscillator frequency and in the limit of a large spin. For the latter it captures the leading quantum corrections to the classical limit exactly including the spin-oscillator entanglement entropy. For moderate spin lengths however the ansatz encounters problems near the transition regime and then fails to reproduce the precursors of the quantum phase transition. Our analysis illustrates the principal limits of the variational method to correctly describe the critical behavior emerging in the quantum regime ahead of a quantum phase transition. A possible improvement of the ansatz with the prospect to overcome the artefacts remains an open problem for future work.

In Article III we have studied the dynamics of spin and oscillator coherent states in the nonresonant Dicke model at weak coupling. In this regime periodic collapses and

revivals of Rabi oscillations occur, which are accompanied by the buildup and decay of atom-field entanglement. The spin-oscillator wave function evolves into a superposition of multiple field coherent states that are correlated with the spin configuration. In our work we provide a description of the underlying dynamical mechanism based on perturbation theory. Our analysis shows that collapse and revival at nonresonance is distinguished from the resonant case treated within the rotating wave approximation by the appearance of two time scales instead of one. The generation of either spin or oscillator cat states during the collapse phase, accompanied by the buildup of atom-field entanglement or atomic squeezing depends thus on the sign of the detuning between the spin and oscillator frequency.

In Article IV we have extended our study of the Dicke dynamics to the case of increasing spin length, as the system approaches the classical spin limit. We described the emergence of collective excitations above the ground state that converge to the coupled spin-oscillator oscillations observed in the classical limit. With increased spin length the corresponding Green functions thus reveal quantum dynamical signatures of the quantum phase transition. For the dynamics at larger coupling and energy, classical phase space drift and quantum diffusion hinders the direct comparison of quantum and classical observables. As we show in our work, signatures of classical quasiperiodic orbits can be identified in the Husimi phase-space functions of the propagated wave function and individual eigenstates with energies close to that of the quasiperiodic orbits.

Our work on the quantum to classical crossover in the Dicke model is restricted to a Hamiltonian system without dissipation. The analysis of the generic optomechanical system given in Article V thus complements our study of cavity QED systems by a quantum dissipative system. In this thesis we have shown for the first time, how the route to chaos in the classical optomechanical system takes place, given as a sequence of consecutive period doubling bifurcations of self-induced cantilever oscillations. In addition to the semiclassical dynamics we have analyzed the possibility of chaotic motion in the quantum regime. Our results showed that quantum mechanics protects the optomechanical system against irregular dynamics. In sufficient distance to the semiclassical limit simple periodic orbits reappear and replace the classically chaotic motion. In this way direct observation of the dynamical properties of an optomechanical system makes it possible to pin down the crossover from quantum to classical mechanics. However the precise nature of the quantummechanical state of the coupled photon-phonon system is not studied. Future work should therefore examine the influence of quantum correlations and entanglement on the crossover from classical chaotic motion to the simple periodic orbits of quantum mechanics.

2 Thesis Articles

Author Contribution

Article I:

“Quantum phase transition in the Dicke model with critical and noncritical entanglement”, L. Bakemeier, A. Alvermann, and H. Fehske, *Phys. Rev. A* **85**, 043821 (2012). Copyright (2012) by the American Physical Society.

L. Bakemeier, A. Alvermann, and H. Fehske outlined the scope and strategy of the calculation. The calculation was performed by L. Bakemeier. L. Bakemeier and A. Alvermann wrote the manuscript which was edited by all authors.

Article II:

“Variational treatment of entanglement in the Dicke model”, L. Bakemeier, A. Alvermann, and H. Fehske, submitted to *Physica Scripta*

L. Bakemeier, A. Alvermann, and H. Fehske outlined the scope and strategy of the calculation. The calculation was performed by L. Bakemeier. L. Bakemeier and A. Alvermann wrote the manuscript which was edited by all authors.

Article III:

“Collapse-revival dynamics and atom-field entanglement in the nonresonant Dicke model”, A. Alvermann, L. Bakemeier, and H. Fehske, *Phys. Rev. A* **85**, 043803 (2012). Copyright (2012) by the American Physical Society.

L. Bakemeier, A. Alvermann, and H. Fehske outlined the scope and strategy of the calculation. The calculation was performed by L. Bakemeier. A. Alvermann and L. Bakemeier wrote the manuscript which was edited by all authors.

Article IV:

“Dynamics of the Dicke model close to the classical limit”, L. Bakemeier, A. Alvermann, and H. Fehske, *Phys. Rev. A* **88**, 043835 (2013). Copyright (2013) by the American Physical Society.

L. Bakemeier, A. Alvermann, and H. Fehske outlined the scope and strategy of the calculation. The calculation was performed by L. Bakemeier. L. Bakemeier and A. Alvermann wrote the manuscript which was edited by all authors.

Article V:

“Route to chaos in optomechanics”, L. Bakemeier, A. Alvermann, and H. Fehske, submitted to *Phys. Rev. Lett.*

L. Bakemeier, A. Alvermann, and H. Fehske outlined the scope and strategy of the calculation. The calculation was performed by L. Bakemeier. L. Bakemeier and A. Alvermann wrote the manuscript which was edited by all authors.

Confirmed:

(Prof. Dr. Holger Fehske)

Greifswald, 21 October 2014

(Lutz Bakemeier)

Greifswald, 21 October 2014

Quantum phase transition in the Dicke model with critical and noncritical entanglement

L. Bakemeier

Institut für Physik, Ernst-Moritz-Arndt-Universität, 17487 Greifswald, Germany

A. Alvermann*

Theory of Condensed Matter, Cavendish Laboratory, Cambridge CB3 0HE, United Kingdom

H. Fehske

Institut für Physik, Ernst-Moritz-Arndt-Universität, 17487 Greifswald, Germany

(Received 15 February 2012; published 13 April 2012)

We study the quantum phase transition of the Dicke model in the classical oscillator limit, where it occurs already for finite spin length. In contrast to the classical spin limit, for which spin-oscillator entanglement diverges at the transition, entanglement in the classical oscillator limit remains small. We derive the quantum phase transition with identical critical behavior in the two classical limits and explain the differences with respect to quantum fluctuations around the mean-field ground state through an effective model for the oscillator degrees of freedom. With numerical data for the full quantum model we study convergence to the classical limits. We contrast the classical oscillator limit with the dual limit of a high-frequency oscillator, where the spin degrees of freedom are described by the Lipkin-Meshkov-Glick model. An alternative limit can be defined for the Rabi case of spin length one-half, in which spin frequency renormalization replaces the quantum phase transition.

DOI: [10.1103/PhysRevA.85.043821](https://doi.org/10.1103/PhysRevA.85.043821)

PACS number(s): 42.50.Ct, 42.50.Pq, 03.65.Ud, 05.30.Rt

I. INTRODUCTION

For a system of a single spin coupled to a quantum harmonic oscillator a quantum phase transition (QPT) [1] can take place only in the classical limit of one of the two components, that is, in the limit of infinite spin length or zero oscillator frequency. Prior to the respective classical limit, the spin-oscillator system admits no phase transition since symmetry-breaking states can always be combined in a linear superposition that restores the symmetry and reduces the energy further. In the classical limit phase transitions become possible because different classical states have zero overlap, which circumvents the previous argument against symmetry breaking.

This type of QPT is realized in the Dicke model [2],

$$H = \Delta J_z + \Omega a^\dagger a + \lambda(a^\dagger + a)J_x. \quad (1)$$

It describes an ensemble of $2j$ two-level atoms with transition frequency Δ as a pseudospin of length j (using spin operators $J_{x/z}$). The atoms are coupled to a single cavity mode of the photon field with frequency Ω (using bosonic operators $a^{(\dagger)}$). The Hamiltonian in Eq. (1) is invariant under the replacement $J_x \mapsto -J_x$, $a \mapsto -a$. This symmetry is broken in a phase transition, and the spin expectation value $\langle J_x \rangle$ serves as the order parameter.

In the classical spin (CS) limit $j \rightarrow \infty$ the Dicke model features a thermodynamic phase transition from a high-temperature state with $\langle J_x \rangle = \langle a \rangle = 0$ to a superradiant state with a finite cavity field ($\langle a \rangle \neq 0$) and macroscopic atomic excitation ($\langle J_x \rangle \neq 0$) at low temperatures [3–5]. The thermodynamic phase transition is complemented at zero temperature

by a QPT from the zero field to the superradiant state at a critical atom-field (i.e., spin-oscillator) coupling λ_c .

The driving mechanism behind the QPT is the critical behavior of a classical energy functional for the spin, which is obtained after integrating out the quantum-mechanical oscillator. Strictly in the $j = \infty$ limit the ground state is a mean-field (MF) product state of a spin and oscillator coherent state. The order parameter $\langle J_x \rangle$ and the corresponding susceptibility χ , which characterize the critical behavior, converge to the classical results if the CS limit is approached from $j < \infty$.

Modifications of the classical picture arise from quantum corrections of order $1/j$ to the MF ground state [6,7]. Spin and oscillator variances diverge and signal the breakdown of the classical limit in the vicinity of the QPT. A characteristic feature is the criticality of spin-oscillator entanglement [8–10], which is related to the vanishing excitation gap at the QPT and found for many different models in the CS limit [11].

In this paper we address a QPT in the different classical limit $\Omega \rightarrow 0$, the classical oscillator (CO) limit. In contrast to the CS limit, a QPT transition occurs here already at finite spin length j . The critical behavior is identical to the CS limit, since both limits realize the same MF transition. Quantum corrections to the MF ground state are different. In the CO limit spin fluctuations are suppressed because of the large spin frequency. Therefore, the spin variance and the spin-oscillator entanglement remain small in the vicinity of the QPT. The entanglement entropy is bounded by $\ln 2$ independently of j . The CS and CO limits thus give rise to QPTs with identical critical behavior that are distinguished through the criticality versus noncriticality of entanglement.

An overview of the different limits in the Dicke model is given in Fig. 1. The paper is organized according to this diagram. We first derive in Sec. II the QPT in the CS and the CO limit from MF theory, which becomes exact in the

*Present address: Institut für Physik, Ernst-Moritz-Arndt-Universität, 17487 Greifswald, Germany; alvermann@physik.uni-greifswald.de

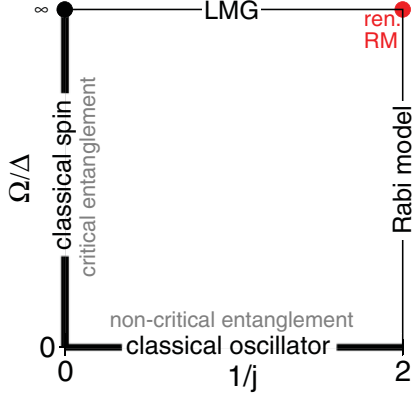


FIG. 1. (Color online) Diagram of the qualitative behavior of the Dicke model in dependence on the spin length j and the oscillator-spin frequency ratio Ω/Δ . The bold axes correspond to the QPT in the CS limit $1/j = 0$ and the CO limit $\Omega/\Delta = 0$. The top edge of the square corresponds to the FO limit $\Omega/\Delta \rightarrow \infty$, where the LMG model describes the spin. On the right edge of the square we find the Rabi model ($j = 1/2$), with renormalization of the effective spin frequency in the limit $\Omega/\Delta \rightarrow \infty$ (top right corner).

two limits. Quantum corrections in the CO limit are discussed in Sec. III with an effective bosonic model for the oscillator degree of freedom and contrasted with the behavior in the CS limit known from the literature. The (non-) criticality of entanglement is addressed in Sec. IV. We complement the CO limit with the fast oscillator (FO) limit $\Omega/\Delta \rightarrow \infty$ in Sec. V. Similar to the considerations for the CO limit, the large oscillator frequency leads to the suppression of oscillator fluctuations. One obtains the Lipkin-Meshkov-Glick (LMG) model for the spin degree of freedom, but no QPT occurs unless we let again $j \rightarrow \infty$. A related FO limit that is peculiar to the Rabi case $j = 1/2$ leads to renormalization of the spin frequency instead of a QPT. The appendixes summarize the solution of the effective bosonic models for the CO and FO limit (Appendix A), and the definition of coherent states (Appendix B) and of the rotation invariant spin variance (Appendix C).

II. CLASSICAL LIMITS AND THE QUANTUM PHASE TRANSITION

As noted in the Introduction, the Dicke Hamiltonian from Eq. (1) is invariant under the symmetry transformation

$$\Pi = e^{i\pi N_E}; \quad N_E = a^\dagger a + J_z + j, \quad (2)$$

which corresponds to the simultaneous replacement of $a \mapsto -a$ and $J_x \mapsto -J_x$. We have $\Pi^{-1}H\Pi = H$ or $[H, \Pi] = 0$, such that the eigenstates of H can be classified by the eigenvalues ± 1 of the parity operator Π . For positive Δ , the ground state of the Dicke model has positive parity.

The QPT breaks parity symmetry, with a finite order parameter $\langle J_x \rangle \neq 0$ above a critical coupling. To study the convergence to the classical limits it is useful to break the parity symmetry explicitly, using the Hamiltonian

$$H_\epsilon = H - \epsilon J_x, \quad (3)$$

which includes a symmetry breaking field ϵJ_x .

A. Mean-field theory of the QPT

Let us first discuss the QPT in the MF picture. The MF ansatz for the ground-state wave function

$$|\psi_{\text{MF}}\rangle = |\theta\rangle \otimes |\alpha\rangle \quad (4)$$

is a product of a spin coherent state $|\theta\rangle$ and a boson coherent state $|\alpha\rangle$ (cf. Appendix B). This state has energy

$$\begin{aligned} E(\theta, \alpha) &= \langle \psi_{\text{MF}} | H | \psi_{\text{MF}} \rangle \\ &= -j\Delta \cos \theta + \Omega\alpha^2 + 2j\lambda\alpha \sin \theta. \end{aligned} \quad (5)$$

Minimization with respect to α results in

$$\alpha = -\frac{j\lambda}{\Omega} \sin \theta, \quad (6)$$

which, inserted into Eq. (5), gives the energy functional

$$E(\theta) = -j\Delta \left(\cos \theta + \frac{\kappa}{2} \sin^2 \theta \right). \quad (7)$$

We here introduce the dimensionless coupling constant

$$\kappa = \frac{2j\lambda^2}{\Delta\Omega}. \quad (8)$$

We assume $\kappa \geq 0$, which corresponds to $\Delta > 0$.

The energy functional $E(\theta)$ describes a second-order MF transition at $\kappa = 1$ (cf. Fig. 2). The minima of $E(\theta)$ are given by

$$\theta = \begin{cases} 0 & \text{if } \kappa < 1, \\ \pm \arccos \frac{1}{\kappa} & \text{if } \kappa > 1, \end{cases} \quad (9)$$

which leads to the expression

$$\langle J_x \rangle = j \sin \theta = \begin{cases} 0 & \text{if } \kappa < 1, \\ \pm j \sqrt{1 - \frac{1}{\kappa^2}} & \text{if } \kappa > 1, \end{cases} \quad (10)$$

for the order parameter $\langle J_x \rangle$. We can also calculate the susceptibility χ using the Hamiltonian H_ϵ from Eq. (3) and find

$$\chi = j\Delta \lim_{\epsilon \rightarrow 0} \frac{\partial \langle J_x \rangle}{\partial \epsilon} = \begin{cases} \frac{1}{1 - \kappa} & \text{if } \kappa < 1, \\ \frac{1}{\kappa(\kappa^2 - 1)} & \text{if } \kappa > 1. \end{cases} \quad (11)$$

In contrast to the prediction of MF theory, the argument given in the Introduction shows that a QPT cannot exist in the fully quantum-mechanical Dicke model for finite $j, \Omega/\Delta$. The

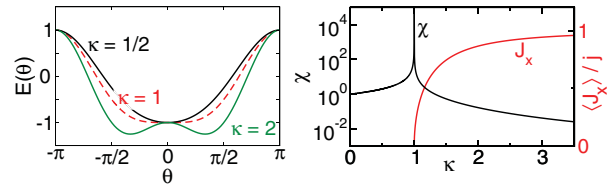


FIG. 2. (Color online) Mean-field QPT in the Dicke model. (Left) Energy functional $E(\theta)$ from Eq. (7) below ($\kappa < 1$), above ($\kappa > 1$), and at ($\kappa = 1$), dashed curve) the QPT. (Right) Order parameter $\langle J_x \rangle$ (red) and susceptibility χ (black) of the MF QPT given in Eqs. (10) and (11).

QPT only becomes possible if the two degenerate MF states for positive or negative θ, α have zero overlap. This can be achieved either if $\langle \theta | -\theta \rangle = 0$ in the CS limit or if $\langle \alpha | -\alpha \rangle = 0$ in the CO limit.

B. QPT in the classical spin limit

In the CS limit $j \rightarrow \infty$ spin coherent states form an orthonormal basis of the spin Hilbert space (see, e.g., Ref. [12]). Therefore, the ground-state wave function has the form $|\psi_{\text{CS}}\rangle = |\theta\rangle \otimes |\psi_{\text{bos}}\rangle$, with a real spin coherent state $|\theta\rangle$ as defined in Eq. (B4) in Appendix B. Note that for $\theta \neq 0$ the overlap $\langle \theta | -\theta \rangle = \cos^{2j} \theta$ goes to zero for $j \rightarrow \infty$, which allows for the QPT.

The bosonic part $|\psi_{\text{bos}}\rangle$ of the wave function, which has to be determined through minimization of the energy $\langle \psi_{\text{CS}} | H | \psi_{\text{CS}} \rangle$, is the ground state of the effective bosonic Hamiltonian

$$H_{\text{osc}}(\theta) = \Omega a^\dagger a + \lambda j \sin \theta (a + a^\dagger), \quad (12)$$

which is parametrized by the CS angle θ .

$H_{\text{osc}}(\theta)$ is the Hamiltonian of an oscillator with a constant force $\propto \lambda j \sin \theta$. The ground state of this Hamiltonian is a boson coherent state $|\psi_{\text{bos}}\rangle = |\alpha\rangle$, with α given by Eq. (6). We thus recover the MF wave function from Eq. (4) in the CS limit, hence also the entire QPT.

C. QPT in the classical oscillator limit

According to Eqs. (6) and (8) the parameter α in the MF ground state in Eq. (4) scales as $1/\sqrt{\Omega}$. For $\Omega \rightarrow 0$ the overlap $\langle \alpha | -\alpha \rangle = \exp(-2\alpha^2)$ goes to zero for $\kappa > 1$. Because of this a QPT in the CO limit is possible independently of the spin length j .

Since the overlap of different real coherent states $|\alpha\rangle$ is zero in the CO limit, the ground-state wave function has the form $|\psi_{\text{CO}}\rangle = |\psi_{\text{spin}}\rangle \otimes |\alpha\rangle$. The spin part $|\psi_{\text{spin}}\rangle$ of the wave function is the ground state of the effective spin Hamiltonian

$$H_{\text{spin}}(\alpha) = \Delta J_z + 2\lambda\alpha J_x, \quad (13)$$

parametrized by the CO displacement α .

$H_{\text{spin}}(\alpha)$ is the Hamiltonian of a spin in a magnetic field $\vec{B} = (2\lambda\alpha, 0, \Delta)$, with a coherent spin state $|\psi_{\text{spin}}\rangle = |\theta\rangle$ as the ground state. θ and α are related through Eq. (6). Again, we recover the MF wave function from Eq. (4) and therefore also the entire QPT in the CO limit.

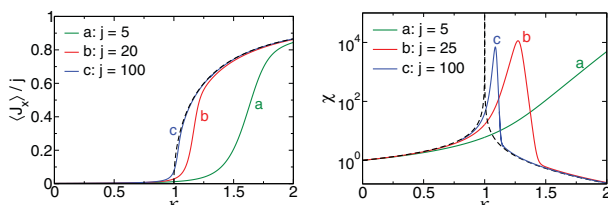


FIG. 3. (Color online) QPT in the CS limit. Order parameter $\langle J_x \rangle$ (left) and susceptibility χ (right) as a function of κ for various values of j and fixed $\Omega/\Delta = 1$. The dashed curves give the MF result from Eqs. (10) and (11).

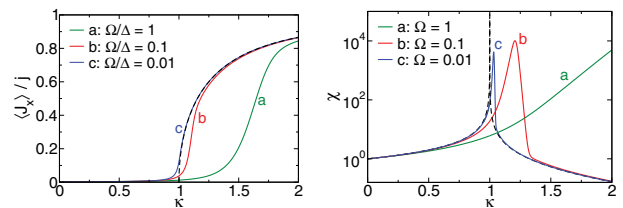


FIG. 4. (Color online) QPT in the CO limit. Order parameter $\langle J_x \rangle$ (left) and susceptibility χ (right) as a function of κ for various values of Ω/Δ and fixed $j = 5$. The dashed curves give the MF result from Eqs. (10) and (11).

Note that the argument for the CS and CO limit are dual to each other: In the CS limit we first observe that the spin has to be in a coherent (“classical”) state and deduce the oscillator coherent state from the particular effective Hamiltonian $H_{\text{osc}}(\theta)$ for the quantum mechanical oscillator. In the CO limit, we start from an oscillator coherent state and obtain the spin coherent state again only because of the particular form of the effective Hamiltonian $H_{\text{spin}}(\alpha)$ for the quantum spin.

D. Convergence to the QPT

Given the QPT in the CS and CO limit, we expect that the order parameter $\langle J_x \rangle$ and the susceptibility χ converge to the MF values from Eqs. (10) and (11) if the classical limits are approached from the quantum regime $j < \infty$, $\Omega/\Delta > 0$, that is, if one moves in Fig. 1 from the interior of the square toward one of the two bold axes.

To observe convergence we must use a small symmetry-breaking field ϵJ_x as in Eq. (3) to select one of the two possible cases $\langle J_x \rangle \geq 0$ in the broken-symmetry phase $\kappa > 1$. Without the additional field convergence cannot be observed because parity symmetry implies that $\langle J_x \rangle = 0$ in the quantum regime. Apart from the calculation of the entanglement entropy in Sec. IV, we use $\epsilon = 10^{-4}$ throughout the paper.

In Figs. 3 and 4 we show $\langle J_x \rangle$ and χ from a numerical calculation of the ground state of the Dicke model using the Lanczos technique [13]. Up to 10^3 bosons are kept in the calculations to ensure a negligible error from the truncation of the infinite-dimensional bosonic Hilbert space. The spin part is not truncated, and the numerical data are accurate on the level of machine precision.

In the figures we start from the curve for $j = 5$, $\Omega/\Delta = 1$, far away from the classical limits. In Fig. 3 we increase j to approach the CS limit, and in Fig. 4 we decrease Ω/Δ to approach the CO limit. In both situations we observe convergence of $\langle J_x \rangle$, χ to the MF values from Eqs. (10) and (11). Note that in the CO limit convergence takes place while the spin length j remains finite.

III. QUANTUM CORRECTIONS TO THE MEAN-FIELD QPT

The previous section showed that MF theory becomes exact in the CS and the CO limit, which are therefore identical with respect to the critical behavior of the QPT. The nature of the two limits is different, however, and they can be distinguished

through the properties of quantum fluctuations around the MF ground state.

The origin of the differences can be understood with a simple energy argument. In the CO limit, the energy scales for spin fluctuations ($\propto \Delta$) and oscillator fluctuations ($\propto \Omega$) separate. Since Δ is large compared to the coupling constant λ , which is proportional to $\sqrt{\Omega}$ [cf. Eq. (8)], spin fluctuations are suppressed in the CO limit. This explains partly why the QPT in the CO limit can occur already for finite j . In the CS limit the ratio Ω/Δ remains constant and neither spin nor oscillator fluctuations are suppressed.

A. Effective model for the CO limit

While spin fluctuations are suppressed in the CO limit, oscillator fluctuations around the classical coherent state $|\alpha\rangle$ remain energetically favorable. Their strength can be derived with an effective bosonic model obtained in perturbation theory.

For $\kappa < 1$ the MF ground state $|-j\rangle \otimes |\text{vac}\rangle$ is the product of the J_z eigenstate $|-j\rangle$ to the smallest eigenvalue $-j$ and the bosonic vacuum $|\text{vac}\rangle$. For $\Delta \gg \Omega$, the low-energy sector of the Hilbert space consists of all states $|-j\rangle \otimes |\psi_{\text{bos}}\rangle$ with a bosonic state $|\psi_{\text{bos}}\rangle$. While the operator J_z remains in the low-energy sector, the operator J_x creates a spin excitation $\propto |-j+1\rangle$ of energy Δ .

Standard perturbation theory [14] gives the effective low-energy model for the bosonic state $|\psi_{\text{bos}}\rangle$ as

$$\begin{aligned} H_{\text{bos}}^{\leq} &= \langle -j | \Delta J_z + \Omega a^\dagger a + \frac{\lambda^2}{\Delta} [(a + a^\dagger) J_x]^2 | -j \rangle \\ &= -\Delta j + \Omega \left[a^\dagger a - \frac{\kappa}{4} (a + a^\dagger)^2 \right]. \end{aligned} \quad (14)$$

Using the results from Appendix A for the bosonic part in the second line, we see that the stability condition in Eq. (A7) is fulfilled only for $\kappa < 1$ below the critical coupling. At the QPT $\kappa = 1$ the number of oscillator fluctuations introduced through the term $(a + a^\dagger)^2$ diverges.

For $\kappa > 1$ we must consider spin fluctuations above the classical ground state $|\theta\rangle \otimes |\alpha\rangle$, which are no longer created by J_x since $\theta \neq 0$. Instead, we rewrite the Hamiltonian with the rotated spin operators $\tilde{J}_z = \cos \theta J_z - \sin \theta J_x$, $\tilde{J}_x = \sin \theta J_z + \cos \theta J_x$ and find

$$\begin{aligned} H &= \Delta \cos \theta \tilde{J}_z - \lambda \sin \theta (a + a^\dagger) \tilde{J}_z + \Omega a^\dagger a \\ &\quad + \Delta \sin \theta \tilde{J}_x + \lambda \cos \theta (a + a^\dagger) \tilde{J}_x. \end{aligned} \quad (15)$$

Here the operator \tilde{J}_x appears with the prefactor Δ , and we cannot immediately use this expression for perturbation theory for small Ω/Δ .

To proceed, we shift operators $\tilde{J}_z \mapsto \tilde{J}_z + j$, $a \mapsto a - \alpha$ by their expectation values in the classical ground state, taken from Eqs. (6) and (9), and obtain the Hamiltonian in the form

$$\begin{aligned} H &= E(\theta) + \Delta (\cos \theta + \kappa \sin^2 \theta) (\tilde{J}_z + j) \\ &\quad - \lambda \sin \theta (a + a^\dagger - 2\alpha) (\tilde{J}_z + j) \\ &\quad + \Omega (a^\dagger - \alpha)(a - \alpha) + \lambda \cos \theta (a + a^\dagger - 2\alpha) \tilde{J}_x, \end{aligned} \quad (16)$$

where the first term is the energy functional $E(\theta)$ from Eq. (7). In this expression, a term $2\alpha\lambda \cos \theta J_x$ has canceled

the problematic term $\Delta \sin \theta \tilde{J}_x$ for the values of α, θ given by Eqs. (6) and (9).

Now, \tilde{J}_x in the last line appears with a prefactor that is small compared to Δ and perturbation theory can be applied. Note that the spin fluctuation energy, which is given by the prefactor $\Delta (\cos \theta + \kappa \sin^2 \theta) = \Delta \kappa$ of $\tilde{J}_z + j$, differs from the bare value Δ . The effective model for $\kappa > 1$ is obtained as

$$\begin{aligned} H_{\text{bos}}^{\geq} &= -\frac{j\Delta}{2} \left(\frac{1}{\kappa} + \kappa \right) \\ &\quad + \Omega \left[(a^\dagger - \alpha)(a - \alpha) - \frac{1}{4\kappa^2} (a + a^\dagger - 2\alpha)^2 \right]. \end{aligned} \quad (17)$$

For $\kappa \rightarrow 1$, it coincides with H_{bos}^{\leq} from Eq. (14).

The effective low-energy models H_{bos}^{\geq} describe the ground state of the Dicke model in the CO limit including oscillator fluctuations. From this model we recover the MF expressions for α and $E(\theta)$, and thus the entire QPT in the CO limit. In particular the present derivation shows that the argument given in Sec. II C is correct and not invalidated by oscillator fluctuations.

For a quantitative analysis of the numerical data, we use the oscillator variance

$$\Delta_q = \langle \hat{q}^2 \rangle - \langle \hat{q} \rangle^2 \quad (18)$$

of the oscillator position $\hat{q} = (a + a^\dagger)$. Using the results from Appendix A the variance is obtained from H_{bos}^{\geq} as

$$\Delta_q = \begin{cases} (1 - \kappa)^{-1/2} & \text{if } \kappa < 1, \\ (1 - 1/\kappa^2)^{-1/2} & \text{if } \kappa > 1. \end{cases} \quad (19)$$

B. Spin and oscillator variance

In Fig. 5 we compare the oscillator variance Δ_q for small Ω/Δ with the spin variance Δ_J . We use Δ_J , as defined in Appendix C, instead of the spin variance in a fixed direction, for example $\Delta_z = \langle J_z^2 \rangle - \langle J_z \rangle^2$, since it is invariant under rotations. For fluctuations around the spin coherent state $|\theta = 0\rangle$ that points in the z direction it is identical to Δ_z . Above the QPT, Δ_J accounts for the rotation of the spin axis relative to which spin fluctuations occur. A large Δ_J is an indication of significant spin fluctuations, while $\Delta_J = 0$ corresponds (in the present examples) to a spin coherent state. The vanishing of $\Delta_J \rightarrow 0$ (left panel) shows the suppression of spin fluctuations in the CO limit.

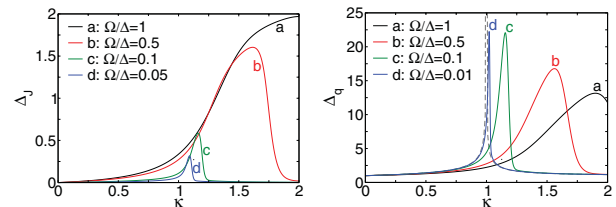


FIG. 5. (Color online) Spin variance Δ_J (left) and oscillator variance Δ_q (right) for decreasing Ω/Δ approaching the CO limit, with fixed finite $j = 5$. The dashed gray curve in the right panel gives the analytical for Δ_q from Eq. (19).

For Δ_q in the right panel we observe the growth of oscillator fluctuations with decreasing Ω/Δ . Recall that $j = 5$ is finite and small in this example, and the QPT in the CO limit is triggered by a macroscopic displacement of the CO. Oscillator fluctuations are a genuine quantum correction, which is independent of j and occurs even in the smallest nontrivial case $j = 1/2$. Approaching the CO limit, Δ_q diverges at the QPT according to Eq. (19). The criticality of quantum fluctuations implies the breakdown of the CO limit in the vicinity of the QPT.

IV. CRITICAL AND NONCRITICAL ENTANGLEMENT

In addition to the spin and oscillator variance studied in the previous section, corrections to the MF ground state arise from spin-oscillator entanglement. It can be measured with the entanglement entropy

$$S = -\text{Tr}[\rho \ln \rho], \quad (20)$$

which is calculated with the reduced spin or oscillator density matrix ρ (both choices give the same result according to the Schmidt decomposition) [15,16].

A simple argument would suggest a jump of S at $\kappa = 1$ from $S = 0$ for the nondegenerate ground state below the QPT to $S = \ln 2$ for the twofold degenerate ground state above the QPT. Note that we assume $\epsilon = 0$ here.

Quantum fluctuations can modify this behavior considerably and lead to criticality of entanglement in the CS limit [8,9]. In the vicinity of the QPT the entanglement entropy in the CS limit is given as [9,11]

$$S_{\text{CS}} = -\frac{1}{4} \ln |1 - \kappa| + \text{const.}, \quad (21)$$

such that S_{CS} diverges at the critical coupling $\kappa = 1$ with critical exponent $1/4$.

We show S_{CS} in Fig. 6 (left panel). The functional form of $S_{\text{CS}} = S_{\text{CS}}(\kappa)$ depends on the ratio Ω/Δ . For $\Omega/\Delta \ll 1$ or $\Omega/\Delta \gg 1$ quantum spin or oscillator fluctuations are energetically less favorable than for $\Omega/\Delta = 1$, and the value of S decreases away from the QPT. The criticality of S_{CS} at the QPT and the critical exponent, however, are independent of Ω/Δ .

A. Entanglement in the classical oscillator limit

Almost trivially, the entanglement entropy S cannot diverge for finite j since it is bounded by $S \leq \ln(2j + 1)$. The suppression of spin fluctuations in the CO limit results in the much stricter condition $S \leq \ln 2$, independently of j . Large entanglement requires a sizable amount of both oscillator and spin fluctuations.

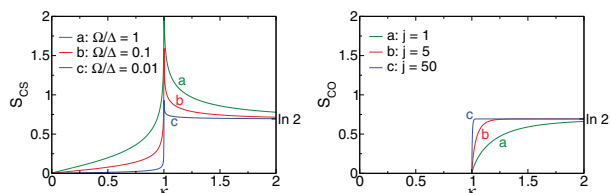


FIG. 6. (Color online) Entanglement entropy S in the CS limit (left panel) (cf. Ref. [8]) and in the CO limit (right) according to Eq. (24).

For $\kappa < 1$ the ground state is a product state and $S_{\text{CO}}[\kappa < 1] = 0$. This follows immediately from the fact used in the perturbative calculation in Sec. III A that the spin part of the ground state is the single J_z eigenstate $|-j\rangle$. In contrast to the CS limit, the absence of spin fluctuations prevents the growth of S_{CO} with increasing κ .

For $\kappa > 1$ the symmetrized ground-state wave function is given by

$$|\psi\rangle = \frac{1}{\sqrt{2}}(|\theta\rangle \otimes |\alpha\rangle \pm |-\theta\rangle \otimes |-\alpha\rangle). \quad (22)$$

Note that we assume $\epsilon = 0$ here.

The two states in the bracket are orthogonal since $\langle \alpha | -\alpha \rangle = 0$ in the CO limit [α diverges according to Eq. (6)], but the two spin coherent states $|\pm\theta\rangle$ are not orthogonal such that S remains strictly smaller than $\ln 2$.

The reduced spin density matrix is

$$\rho_s = \frac{1}{2}(|\theta\rangle\langle\theta| + |-\theta\rangle\langle-\theta|), \quad (23)$$

with eigenvalues $\mu_{\pm} = 1 \pm \langle \theta | -\theta \rangle = 1 \pm \cos 2\theta$. Note that this expression for ρ_s is valid also for the nonorthogonal states appearing here.

The entanglement entropy obtained from ρ_s as $S_{\text{CO}} = -\mu_- \ln \mu_- - \mu_+ \ln \mu_+$ is

$$S_{\text{CO}}[\kappa > 1] = \ln 2 - \frac{1}{2}(1 - \kappa^{-2j}) \ln(1 - \kappa^{-2j}) - \frac{1}{2}(1 + \kappa^{-2j}) \ln(1 + \kappa^{-2j}), \quad (24)$$

where we inserted the angle $\cos \theta = 1/\kappa$ according to Eq. (9).

We show S_{CO} in Fig. 6 (right panel), where it can be compared to S_{CS} . In the CO limit the entropy remains zero for $\kappa < 1$ and increases monotonically from 0 to $\ln 2$ for $\kappa > 1$. Note that $S_{\text{CO}} \leq \ln 2$ for all j and κ .

For finite j , it remains $S_{\text{CO}} < \ln 2$ even above the QPT because of the finite overlap $\langle \theta | -\theta \rangle$. For $j \rightarrow \infty$, still strictly in the CO limit $\Omega = 0$, the overlap of the two spin coherent states vanishes and the curves approach a step function with a jump at $\kappa = 1$.

B. Quantum regime

We show in Fig. 7 the convergence of the entanglement entropy S to the analytical results for the two classical limits. As in Figs. 3 and 4 we start from the curve for $j = 5$, $\Omega/\Delta = 1$. In the CS limit (left panel) we see how the divergence of S at

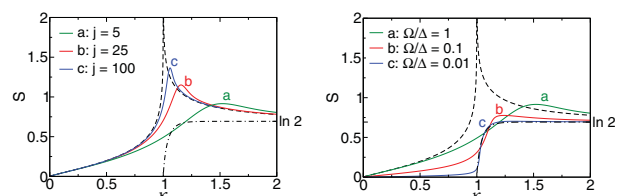


FIG. 7. (Color online) Convergence of entanglement entropy S toward the classical limits. (Left) Approaching the CS limit with increasing j for fixed $\Omega/\Delta = 1$. (Right) Approaching the CO limit with decreasing Ω/Δ for fixed $j = 5$. The dashed (dot-dashed) curve gives the analytical result in the CS (CO) limit according to Fig. 6 and Eqs. (21) and (24).

$\kappa = 1$ develops as j is increased. For the CO limit (right panel) we see that S remains small and converges to a continuous function bounded by $\ln 2$. Since j is finite, the limiting curve is continuous without the jump at $\kappa = 1$ that evolves only for $j \rightarrow \infty$.

It should be noted that the CO limit with $j \gg 1$ and small entanglement differs from the regime $\Omega \ll \Delta$ in the CS limit where the entanglement entropy still diverges at the QPT [17,18]. Both situations are located close to the origin in Fig. 1, but the first (second) situation lies closer to the abscissa (ordinate) than to the second axis.

V. FAST OSCILLATOR LIMIT AND THE LIPKIN-MESHKOV-GLICK MODEL

Opposed to the CO limit is the FO limit $\Omega/\Delta \rightarrow \infty$. In this limit oscillator fluctuations are suppressed, while the spin fluctuations are described by an effective model that can be derived in perturbation theory analogously to Sec. III A. This results in the LMG model [19] known from nuclear physics. For the special case $j = 1/2$, where the Dicke model reduces to the Rabi model, the FO limit can also be performed with a different scaling of the coupling constant.

A. Derivation of the LMG model in the FO limit

We can derive the LMG model as the effective low-energy model for the spin part of the wave function in analogy to Sec. III A. The derivation is, in fact, easier than in the CO limit, since fluctuations around the bosonic coherent state $|\alpha\rangle$ are described by translated bosonic operators $a^\dagger - \alpha$ instead of rotated (spin) operators. The effective spin model, which is valid for all κ , is obtained as the LMG model,

$$H_{\text{LMG}} = \Delta \left(J_z - \frac{\kappa}{2j} J_x^2 \right). \quad (25)$$

In Fig. 8 we show the spin variance Δ_J (left panel) and the oscillator variance Δ_q (right panel) for large Ω/Δ . In reversal of the behavior in the CO limit, we see the suppression of oscillator fluctuations. Spin fluctuations remain finite and converge for $\Omega/\Delta \rightarrow \infty$ to the result from the LMG model.

In contrast to the CO limit, no QPT, and therefore no divergence of spin fluctuations, occurs in the FO limit for finite j , simply because the initial argument against symmetry breaking given in the introduction applies to the LMG model.

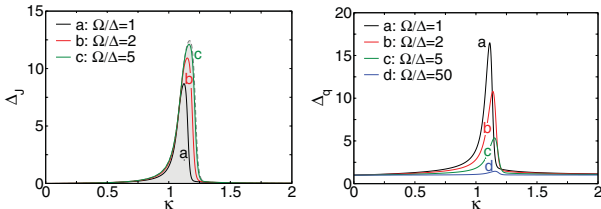


FIG. 8. (Color online) Spin variance Δ_J (left) and oscillator variance Δ_q (right) for increasing Ω/Δ approaching the FO limit, with fixed large $j = 50$. The gray shaded background curve in the left panel gives Δ_J for the LMG model. This figure complements Fig. 5 for the CO limit.

The QPT is recovered if additionally the $j \rightarrow \infty$ limit is performed in the LMG model. Then, the ground state of H_{LMG} is a spin coherent state $|\theta\rangle$, and we recover the energy functional $E(\theta)$ from Eq. (7). Consequently, we also recover the QPT. In this sense, the FO and CS limit commute.

To calculate the spin fluctuations for $j \rightarrow \infty$, we use the Holstein-Primakoff (HP) transformation [20],

$$J_z = b^\dagger b - j, \quad J_x = \sqrt{\frac{j}{2}}(b^\dagger + b) + O(j^{-1/2}), \quad (26)$$

of spin operators to bosonic operators $b^{(\dagger)}$. For $\kappa < 1$, when $\theta = 0$, the HP transformation can be applied directly to H_{LMG} and results in the bosonic model

$$H_\infty^< = \Delta \left[b^\dagger b - \frac{\kappa}{4}(b + b^\dagger)^2 - j \right]. \quad (27)$$

For $\kappa > 1$ it is $\theta \neq 0$ and spin operators must be rotated prior to the HP transformation, similarly to Eq. (15) in Sec. III A. We now obtain the bosonic model

$$H_\infty^> = \Delta \kappa \left[b^\dagger b - \frac{1}{4\kappa^2}(b + b^\dagger)^2 \right] - \frac{j\Delta}{2}(\kappa + 1/\kappa). \quad (28)$$

Comparison of these models to the effective bosonic models H_{bos}^{\geq} from Eqs. (14) and (17) reveals the duality of the CO limit and the combined FO/CS limit in the sense that the role of spin and oscillator fluctuations are reversed.

Using the results from Appendix A for H_∞^{\geq} , we find the spin variance Δ_J as (still for $j \rightarrow \infty$)

$$\Delta_J^\infty = \begin{cases} \frac{\kappa^2}{8(1-\kappa)} & \text{if } \kappa < 1, \\ \frac{1}{8\kappa^2(\kappa^2-1)} & \text{if } \kappa > 1. \end{cases} \quad (29)$$

The spin variance for large j is shown in Fig. 9. We observe convergence to the analytical result for $j \rightarrow \infty$. Again, the QPT is accompanied by a divergence of fluctuations and a breakdown of the corresponding CS limit.

B. FO limit for the Rabi case $j = 1/2$

The FO limit can also be treated by a unitary transformation UHU^\dagger of the Dicke Hamiltonian, where U is given as

$$U = \exp[-\xi(a^\dagger - a)J_x], \quad \xi = \frac{\lambda}{\Omega}. \quad (30)$$

The transformation U displaces oscillator states by a shift $m_x \xi$ that depends on the J_x eigenvalues m_x . The equivalent

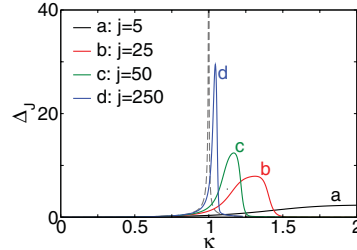


FIG. 9. (Color online) Spin variance Δ_J for increasing j approaching the QPT, with fixed large $\Omega/\Delta = 20$. The gray dashed curve gives the analytical result for Δ_J from Eq. (29).

transformation in polaron physics is known as the Lang-Firsov transformation [21].

With the above choice for ξ , the interaction term $(a^\dagger + a)J_x$ is eliminated through the transformation, and the transformed Hamiltonian reads

$$UHU^\dagger = \Delta \cosh[\xi(a^\dagger - a)]J_z + i\Delta \sinh[\xi(a^\dagger - a)]J_y + \Omega a^\dagger a - \frac{\lambda^2}{\Omega} J_x^2. \quad (31)$$

So far, the transformation is an exact reformulation of the problem. We can now note that for $\Omega \rightarrow \infty$ the presence of the term $\Omega a^\dagger a$ implies that the ground state of UHU^\dagger contains no bosonic excitations. The transformed ground-state wave function has the form $|\psi_{\text{spin}}\rangle \otimes |\text{vac}\rangle$. In the vacuum $|\text{vac}\rangle$ the bosonic operators from UJ_zU^\dagger have expectation values

$$\begin{aligned} \langle \text{vac} | \cosh[\xi(a^\dagger - a)] | \text{vac} \rangle &= e^{-\xi^2/2}, \\ \langle \text{vac} | \sinh[\xi(a^\dagger - a)] | \text{vac} \rangle &= 0, \end{aligned} \quad (32)$$

and the transformed Hamiltonian UHU^\dagger reduces to

$$H_{\text{FO}} = \Delta e^{-(\lambda^2/\Omega^2)/2} J_z - \frac{\lambda^2}{\Omega} J_x^2. \quad (33)$$

We can perform the FO limit in this model in two relevant ways. If we insert the coupling constant κ from Eq. (8) as done before, we obtain the LMG model from Eq. (25). Alternatively, we can keep the parameter $\xi = \lambda/\Omega$ of the transformation constant. Then the prefactor of J_x^2 will diverge for $\Omega \rightarrow \infty$ as we push the system into the strong coupling limit above the QPT. This limit is not interesting for general j .

In the special Rabi case $j = 1/2$, however, it is $J_x^2 = 1/4$. The first kind of FO limit is trivial for this model since it results in the Hamiltonian $\Delta J_z - \kappa/4$ of a free spin. Instead, we can perform the second FO limit because the divergent prefactor of J_x^2 now results only in a divergent shift of the ground-state energy that can be dropped from the Hamiltonian.

We then obtain the simple model

$$H_{\text{ren}} = \tilde{\Delta} J_z \quad (34)$$

of a spin J_z with renormalized frequency $\tilde{\Delta} = e^{-\xi^2/2} \Delta$. It results in the susceptibility

$$\chi_{\text{ren}} = \tilde{\Delta}^{-1} = \frac{e^{\xi^2/2}}{\Delta}, \quad (35)$$

which grows monotonically with the effective coupling strength $\xi = \lambda/\Omega$. The frequency renormalization is the sole effect of coupling to the FO. The exponential prefactor is an example of a Franck-Condon factor, known from the theory of vibronic transitions or polaron physics.

While the transformed model H_{ren} is also not very interesting by itself, with a simple ground state $|-\frac{1}{2}\rangle \otimes |\text{vac}\rangle$, it allows us to obtain the actual ground state of the Rabi model through the transformation U . It is given by

$$\begin{aligned} |\psi\rangle &= U \left[\left| -\frac{1}{2} \right\rangle \otimes |\text{vac}\rangle \right] \\ &= \frac{1}{\sqrt{2}} (|\rightarrow\rangle \otimes |\xi\rangle - |\leftarrow\rangle \otimes |-\xi\rangle), \end{aligned} \quad (36)$$

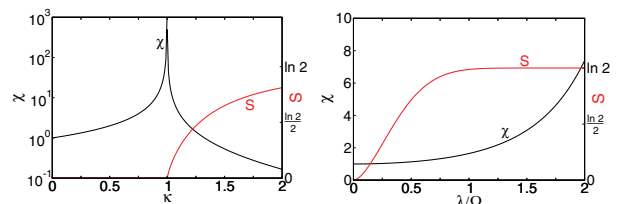


FIG. 10. (Color online) Susceptibility χ and entanglement entropy S for the Rabi case $j = \frac{1}{2}$ in the CO limit [left, Eqs. (11) and (24)] and the FO limit [right, Eqs. (35) and (37)].

where we denote the $j = \pm 1/2$ eigenstates of J_x by $|\rightarrow\rangle, |\leftarrow\rangle$. The entanglement entropy in this state is given by

$$\begin{aligned} S_{\text{ren}} &= \ln 2 - \frac{1}{2}(1 - e^{-2\xi^2}) \ln(1 - e^{-2\xi^2}) \\ &\quad - \frac{1}{2}(1 + e^{-2\xi^2}) \ln(1 + e^{-2\xi^2}) \end{aligned} \quad (37)$$

[cf. the calculation for Eq. (24)]. Similar to the susceptibility, the entropy S increases monotonically with $\xi = \lambda/\Omega$ from 0 to $\ln 2$.

In Fig. 10 we contrast this behavior with the behavior in the CO limit (also for $j = 1/2$). We see that the entanglement entropy S is close to its maximal value $\ln 2$ already for small χ close to one. In this sense, the FO limit of the Rabi model is characterized by significant entanglement.

Note that the relevant coupling constant scales as λ/Ω in the present FO limit but as λ^2/Ω in the CO limit. Previously, for the Dicke model, we had to choose the same coupling constant $\kappa \propto \lambda^2/\Omega$ for both limits, which leads to a duality of the FO and CO limit. For the Rabi model, we have defined a FO limit that is structurally different from the CO limit: Instead of a QPT it features renormalization of the spin frequency.

The frequency renormalization is peculiar for the Rabi model. It is reminiscent of lattice polarons, where the distinction between self-trapped adiabatic polarons (corresponding to the CO limit) and antiadiabatic polarons (in the FO limit) involves characteristically different signatures in, for example, the optical conductivity [22]. In fact, the Rabi model is equivalent to the Holstein polaron model restricted to two lattice sites [23].

VI. SUMMARY

Two different classical limits can be defined for the Dicke model. The QPT in the CS spin limit $j \rightarrow \infty$ has attracted much attention, and the criticality of spin-oscillator entanglement is understood as its characteristic signature.

As pointed out here the QPT is also realized in the second classical limit, the CO limit $\Omega \rightarrow 0$. It should be noted that the QPT in the CO limit is not simply a special case of the CS limit: It occurs already at finite spin length $j < \infty$, even at $j = 1/2$.

A simple MF argument shows the equivalence of the QPT in the two limits if only the critical behavior is considered. Differences occur for quantum fluctuations around the MF ground state. In the CO limit, the suppression of spin

fluctuations prevents significant entanglement, but oscillator fluctuations are important and diverge at the QPT.

The emergence of a QPT in the CO limit is a general feature, which can occur for any finite quantum system coupled to a harmonic oscillator. It does not require the equivalent of an $j \rightarrow \infty$ limit. In every situation the QPT is accompanied by diverging oscillator fluctuations, while fluctuations of the finite system are suppressed.

Also, the FO limit can be performed for general systems, although a different formulation of the limit should be chosen for two-level systems (the Rabi case $j = 1/2$) and systems with multiple energy levels. The duality of the CO and FO limit is a special feature of the Dicke model, where the spin can be mapped onto a bosonic system for $j \rightarrow \infty$.

The basic physical mechanisms realized in the CO and FO limit are typical for any finite quantum system coupled to harmonic oscillators. Oscillator fluctuations or entanglement with the oscillator for two-level systems in the FO limit can be expected to be of general importance in many situations. The Dicke model is an example where their properties can be studied in detail. One particular feature is the occurrence of one QPT in two classical limits, which are distinguished by entirely different quantum corrections to the MF ground state.

ACKNOWLEDGMENTS

This work was supported by Deutsche Forschungsgemeinschaft through Grant No. AL1317/1-2 and Collaborative Research Center 652.

APPENDIX A: SQUEEZED HARMONIC OSCILLATOR

The Hamiltonian of a squeezed harmonic oscillator has the form

$$H = a^\dagger a + \beta(a + a^\dagger)^2, \quad (\text{A1})$$

with $\beta \in \mathbb{R}$.

The Hamiltonian can be diagonalized with a unitary transformation

$$U = \exp\left[\frac{\sigma}{2}(a^\dagger - a)\right], \quad (\text{A2})$$

for which

$$U a U^\dagger = \cosh \sigma a - \sinh \sigma a^\dagger. \quad (\text{A3})$$

With the choice

$$\tanh 2\sigma = \frac{2\beta}{1 + 2\beta} \quad (\text{A4})$$

the transformed Hamiltonian

$$\tilde{H} = U H U^\dagger = \sqrt{1 + 4\beta} a^\dagger a + E_0 \quad (\text{A5})$$

acquires the form of a standard harmonic oscillator Hamiltonian, with ground-state energy

$$E_0 = \frac{1}{2}\sqrt{1 + 4\beta} - \frac{1}{2} - \frac{\alpha^2}{1 + 4\beta}. \quad (\text{A6})$$

We note the stability condition

$$\beta > -\frac{1}{4}. \quad (\text{A7})$$

For smaller β , the original Hamiltonian is not bounded from below.

Since the ground state of \tilde{H} is the bosonic vacuum, expectation values $\langle \dots \rangle$ in the ground state of H can be evaluated through transformation with U . Especially for the oscillator variances we find

$$\langle (a + a^\dagger)^2 \rangle - \langle a + a^\dagger \rangle^2 = \frac{1}{\sqrt{1 + 4\beta}} \quad (\text{A8})$$

and

$$\langle (a^\dagger a)^2 \rangle - \langle a^\dagger a \rangle^2 = \frac{2\beta^2}{1 + 4\beta}. \quad (\text{A9})$$

APPENDIX B: SOME PROPERTIES OF COHERENT STATES

We summarize the essential properties of oscillator and spin coherent states (see also Ref. [24]).

1. Oscillator coherent states

Coherent states of the oscillator can be defined as the eigenstates of the destruction operator

$$a|\alpha\rangle = \alpha|\alpha\rangle. \quad (\text{B1})$$

The coherent state can be written as

$$|\alpha\rangle = e^{\alpha a^\dagger - \alpha^* a}|0\rangle. \quad (\text{B2})$$

Expectation values are given by

$$\begin{aligned} \langle \alpha | a^\dagger a | \alpha \rangle &= |\alpha|^2, \\ \langle \alpha | a^\dagger + a | \alpha \rangle &= 2 \operatorname{Re} \alpha. \end{aligned} \quad (\text{B3})$$

2. Spin coherent states

A (real) spin coherent state is defined as

$$|\theta\rangle = e^{i\theta J_y} |j, -j\rangle. \quad (\text{B4})$$

It is the eigenstate of the operator $\cos \theta J_z - \sin \theta J_x$ to eigenvalue $-j$, that is,

$$(\cos \theta J_z - \sin \theta J_x)|\theta\rangle = -j|\theta\rangle. \quad (\text{B5})$$

Expectation values of spin operators in the coherent state are given by

$$\begin{aligned} \langle \theta | J_x | \theta \rangle &= j \sin \theta, \\ \langle \theta | J_z | \theta \rangle &= -j \cos \theta. \end{aligned} \quad (\text{B6})$$

The overlap between two spin coherent states is given by

$$\langle \theta | \chi \rangle = \cos^{2j} \frac{\theta - \chi}{2}. \quad (\text{B7})$$

For $j \rightarrow \infty$, the overlap is zero for $\theta \neq \chi$.

APPENDIX C: SPIN VARIANCE

The oscillator variance Δ_q is invariant under translations, which modify the bosonic operators through a linear shift $a \mapsto a + \alpha$. For an analogous spin variance we require invariance under rotations, which leads to a slightly more complicated definition. We restrict ourselves to real spin states; the generalization to arbitrary spin states is straightforward.

We define the spin variance Δ_J as the minimal variance of a rotated spin operator $J_{\parallel} = \cos \theta J_z + \sin \theta J_x$ that is obtained through variation of the rotation angle θ . Expansion of J_{\parallel}^2 shows that Δ_J is the minimum of a quadratic form, and given

by the smaller eigenvalue of the 2×2 matrix

$$\begin{pmatrix} \langle J_x^2 \rangle - \langle J_x \rangle^2 & \langle J_x J_z \rangle - \langle J_x \rangle \langle J_z \rangle \\ \langle J_x J_z \rangle - \langle J_x \rangle \langle J_z \rangle & \langle J_z^2 \rangle - \langle J_z \rangle^2 \end{pmatrix}. \quad (\text{C1})$$

Note that $\langle J_x J_z \rangle = \langle J_z J_x \rangle$ for a real spin state.

For a (real) spin coherent state $|\theta\rangle$, we have $\Delta_J = 0$ since $|\theta\rangle$ is obtained from rotation of the J_z eigenstate $|j, -j\rangle$. Conversely, if the smaller eigenvalue $\Delta_J = 0$, the state is an eigenstate of J_{\parallel} ; that is, it is a rotated eigenstate $|j, m\rangle$ of J_z (the angle θ could be deduced from the eigenvectors). However, it need not be a spin coherent state, which would require $m = \pm j$.

For the Dicke model in the $j \rightarrow \infty$ limit, the spin state for $\kappa < 1$ is invariant under the $J_x \mapsto -J_x$ symmetry. The off-diagonal elements in Eq. (C1) vanish, and $\Delta_J = \Delta_z$ since $\langle J_x^2 \rangle$ is of order j .

-
- [1] S. Sachdev, *Quantum Phase Transitions* (Cambridge University Press, Cambridge, 2000).
 - [2] R. H. Dicke, *Phys. Rev.* **93**, 99 (1954).
 - [3] K. Hepp and E. H. Lieb, *Ann. Phys.* **76**, 360 (1973).
 - [4] Y. K. Wang and F. T. Hioe, *Phys. Rev. A* **7**, 831 (1973).
 - [5] R. Gilmore and C. M. Bowden, *Phys. Rev. A* **13**, 1898 (1976).
 - [6] C. Emary and T. Brandes, *Phys. Rev. Lett.* **90**, 044101 (2003).
 - [7] C. Emary and T. Brandes, *Phys. Rev. E* **67**, 066203 (2003).
 - [8] N. Lambert, C. Emary, and T. Brandes, *Phys. Rev. Lett.* **92**, 073602 (2004).
 - [9] N. Lambert, C. Emary, and T. Brandes, *Phys. Rev. A* **71**, 053804 (2005).
 - [10] J. Vidal and S. Dusuel, *Europhys. Lett.* **74**, 817 (2006).
 - [11] J. Vidal, S. Dusuel, and T. Barthel, *J. Stat. Mech.* (2007) P01015.
 - [12] E. H. Lieb, *Commun. Math. Phys.* **31**, 327 (1973).
 - [13] D. C. Sorensen, *Acta Numerica* **11**, 519 (2002).
 - [14] A. Messiah, *Quantum Mechanics* (North-Holland, Amsterdam, 1961).
 - [15] M. A. Nielsen and I. L. Chuang, *Quantum Computation and Quantum Information* (Cambridge University Press, Cambridge, 2010).
 - [16] R. Horodecki, P. Horodecki, M. Horodecki, and K. Horodecki, *Rev. Mod. Phys.* **81**, 865 (2009).
 - [17] G. Liberti, R. L. Zaffino, F. Piperno, and F. Plastina, *Phys. Rev. A* **73**, 032346 (2006).
 - [18] G. Liberti, F. Plastina, and F. Piperno, *Phys. Rev. A* **74**, 022324 (2006).
 - [19] H. J. Lipkin, N. Meshkov, and A. J. Glick, *Nucl. Phys.* **62**, 188 (1965).
 - [20] T. Holstein and H. Primakoff, *Phys. Rev.* **58**, 1098 (1940).
 - [21] I. G. Lang and Y. A. Firsov, *Zh. Eksp. Teor. Fiz.* **43**, 1843 (1962) [*Sov. Phys. JETP* **16**, 1301 (1963)].
 - [22] A. Alvermann, H. Fehske, and S. A. Trugman, *Phys. Rev. B* **81**, 165113 (2010).
 - [23] J. Ranninger and U. Thibblin, *Phys. Rev. B* **45**, 7730 (1992).
 - [24] W.-M. Zhang, D. H. Feng, and R. Gilmore, *Rev. Mod. Phys.* **62**, 867 (1990).

Variational treatment of entanglement in the Dicke model

L. Bakemeier, A. Alvermann,* and H. Fehske
Institute of Physics, Ernst-Moritz-Arndt-University, 17487 Greifswald

We introduce a variational ansatz for the Dicke model that extends mean-field theory through the inclusion of spin-oscillator correlations. The correlated variational state is obtained from the mean-field product state via a unitary transformation. The ansatz becomes correct in the limit of large oscillator frequency and in the limit of a large spin, for which it captures the leading quantum corrections to the classical limit exactly including the spin-oscillator entanglement entropy. We explain the origin of the unitary transformation before we show that the ansatz improves substantially upon mean-field theory, giving near exact results for the ground state energy and very good results for other observables. We then discuss why the ansatz still encounters problems in the transition regime at moderate spin lengths, where it fails to capture the precursors of the superradiant quantum phase transition faithfully. This observation illustrates the principal limits of semi-classical formulations, even after they are extended with correlations and entanglement.

I. INTRODUCTION

A quantum phase transition (QPT) of mean-field type arises in the semi-classical limit of a quantum system whenever a bifurcation of the equilibria of the associated classical Hamiltonian system occurs [1, 2]. A standard example is that of a particle moving in a one-dimensional potential $V(x) \propto x^4 + ax^2$, where the classical limit is realized through $\hbar \rightarrow 0$ or the equivalent scaling of the particle mass and potential. A QPT occurs because the number of potential energy minima changes as the control parameter a is adjusted from $a > 0$ to $a < 0$. The QPT corresponds to breaking of the $x \mapsto -x$ reflection symmetry of $V(x)$ in the ground state.

The properties of this example are characteristic for the more general situation, in particular for the superradiant QPT in the Dicke model addressed in the present paper. First, the QPT takes place only in the classical limit but not in the quantum regime. Prior to the classical limit the ground state is always non-degenerate because of tunneling between the two potential wells. Because of this the QPT itself is fully described by the classical bifurcation. Quantum effects enter the description of the QPT as corrections to the classical limit for small but finite \hbar . Second, the leading quantum corrections can be computed analytically, but the description of the system at larger \hbar , i.e. away from the classical limit, requires solution of the full Schrödinger equation.

In this contribution we ask whether it is possible to go beyond the semi-classical – or mean-field – description and directly include quantum effects in a variational ansatz for the ground state. The ansatz is variational because the values of its parameters will be determined through energy minimization. Variational ansätze have long been used for the Dicke model and related spin-boson models [3–7], often with the exclusive aim of improving the computation of the ground state energy and

other simple observables. Little attention has been paid to the relevance of quantum correlations and fluctuations for the construction of a variational ansatz.

Our requirement is not only that the ansatz performs reasonably well before the classical limit is performed, i.e. in those regimes where the mean-field description fails. We also demand that the ansatz becomes exact in the classical limit in the sense that the leading order quantum corrections are captured faithfully. To go beyond mean-field theory thus requires not only the construction of some improved variational ansatz but to describe quantum correlations and quantum fluctuations in the ground state in a controlled way.

We discuss these questions here for the superradiant QPT in the Dicke model [8, 9], for which we establish our notation in Sec. II. We recapitulate of the mean-field description of the QPT and the theory of quantum corrections in Secs. III, IV before we introduce the correlated variational ansatz in Sec. V. There, we explain the construction of the ansatz and the origin of the unitary transformation used therein, and show that it does indeed capture the leading quantum corrections to the classical limit of the Dicke model. In Sec. VI we evaluate the variational ansatz in comparison to quasi-exact numerical data for finite spin length, before we conclude in Sec. VII.

II. THE DICKE MODEL

The Dicke model [10]

$$H = \Delta J_z + \kappa J_x (a^\dagger + a) + \Omega a^\dagger a \quad (1)$$

describes an ensemble of N two-level systems, e.g. atomic levels, interacting with a quantum harmonic oscillator, e.g. the photons in a cavity. The two-level systems are combined into a pseudo spin with length $j = N/2$ and operators $J_{x,y,z}$. The cavity photon field is described as a harmonic oscillator with bosonic ladder operators $a^{(\dagger)}$. In addition to the three parameters Δ, Ω, κ and the spin length j we will use also the dimensionless coupling

*Electronic address: alvermann@physik.uni-greifswald.de

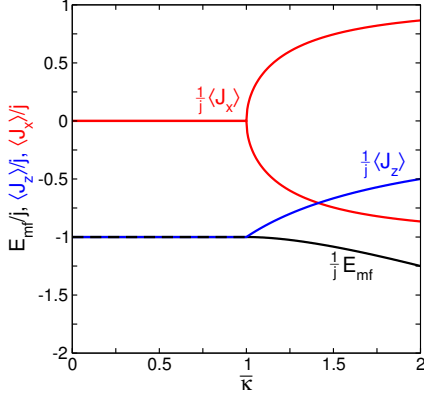


FIG. 1: Energy E_{mf} and spin expectation values $\langle J_x \rangle$, $\langle J_z \rangle$ of the Dicke model in mean-field theory. At $\bar{\kappa} = 1$ the superradiant QPT from $\langle J_x \rangle = 0$ to $\langle J_x \rangle \neq 0$ takes place.

constant $\bar{\kappa}$ with

$$\kappa = \sqrt{\frac{\Delta \Omega \bar{\kappa}}{2j}}. \quad (2)$$

The above Hamiltonian has a combined spin-oscillator reflection symmetry. It is implemented by the unitary operator

$$R = \exp[i\pi(J_z - j)] \exp[i\pi a^\dagger a] \quad (3)$$

with

$$R J_x R^\dagger = -J_x, \quad R a^{(\dagger)} R^\dagger = -a^{(\dagger)} \quad (4)$$

such that $[R, H] = 0$.

The reflection symmetry can be broken in the classical limit $j \rightarrow \infty$ of a large spin [8, 9]. Then, the superradiant QPT from the symmetric ground state with $\langle J_x \rangle = \langle a \rangle = 0$ to a symmetry-broken two-fold degenerate ground state with $\langle J_x \rangle, \langle a \rangle \neq 0$ takes place at the critical coupling $\bar{\kappa} = 1$.

The QPT cannot occur at finite j because the energy of a hypothetical symmetry-broken ground state $|\phi\rangle$ could always be lowered by forming a linear combination with the opposite state $R|\phi\rangle$. Thus, symmetry-breaking is possible only for zero overlap $\langle \phi | R | \phi \rangle = 0$, which requires $j \rightarrow \infty$.

Precursors of the QPT at finite j are visible, e.g., in the entanglement entropy or the spin susceptibility [11]. Nearly degenerate symmetry-broken ground states can be obtained in a situation with small $\langle \phi | R | \phi \rangle \ll 1$ in the usual way by adding a small symmetry-breaking perturbation ϵJ_x to H .

III. MEAN-FIELD THEORY OF THE QPT

The semi-classical – or mean-field – theory of the QPT in the Dicke model is based on the ansatz

$$|\psi_{\text{mf}}\rangle = |\phi\rangle \otimes |\chi\rangle \quad (5)$$

for the ground state, which is the product of a (yet unknown) spin state $|\phi\rangle$ and oscillator state $|\chi\rangle$.

Because of the product form of the ansatz (5) minimization of the mean-field energy

$$E_{\text{mf}} = \langle \psi_{\text{mf}} | H | \psi_{\text{mf}} \rangle = \Delta \langle \phi | J_z | \phi \rangle + \kappa \langle \phi | J_x | \phi \rangle \langle \chi | a^\dagger + a | \chi \rangle + \Omega \langle \chi | a^\dagger a | \chi \rangle \quad (6)$$

splits into two individual minimization problems for the spin and oscillator state, which are coupled only through expectation values formed with the respective other state.

Specifically, the spin state $|\phi\rangle$ has to be the ground state of the effective spin Hamiltonian

$$H_{\text{mf}}^s = \Delta J_z + \xi_1 J_x, \quad (7)$$

with the one parameter $\xi_1 = \kappa \langle \chi | a^\dagger + a | \chi \rangle$. Such a state is a spin coherent state $|\theta\rangle$, with rotation angle $\tan \theta = \xi_1 / \Delta$ relative to the z -axis (see App. A for notation).

Conversely, the oscillator state $|\chi\rangle$ has to be the ground state of the effective boson Hamiltonian

$$H_{\text{mf}}^b = \xi_2 (a^\dagger + a) + \Omega a^\dagger a, \quad (8)$$

where $\xi_2 = \kappa \langle \phi | J_x | \phi \rangle$. The ground state is a boson coherent state $|\alpha\rangle$, with $\alpha = -\xi_2 / \Omega$.

Therefore, the mean-field ground state is

$$|\psi_{\text{mf}}\rangle = |\theta\rangle \otimes |\alpha\rangle, \quad (9)$$

a product state of a spin coherent state $|\theta\rangle$ and an oscillator coherent state $|\alpha\rangle$. It only depends on the two real parameters θ, α . In particular, the absence of spin-oscillator correlations or entanglement in the product state (5) implies that the individual spin and oscillator state is a coherent state.

The mean-field energy then is

$$E_{\text{mf}} = -j\Delta \cos \theta + 2j\kappa\alpha \sin \theta + \Omega\alpha^2, \quad (10)$$

which has to be minimized as a function of θ and α . The optimal α follows immediately as

$$\alpha = -\frac{j\kappa}{\Omega} \sin \theta, \quad (11)$$

such that

$$E_{\text{mf}} = -j\Delta \cos \theta - j^2 \frac{\kappa^2}{\Omega} \sin^2 \theta = -j\Delta (\cos \theta + \frac{1}{2} \bar{\kappa} \sin^2 \theta). \quad (12)$$

The functional form of E_{mf} gives rise to a bifurcation of the minima at the critical value $\bar{\kappa} = 1$. The optimal θ is

$$\theta = \begin{cases} 0 & \text{if } \bar{\kappa} < 1, \\ \pm \arccos(1/\bar{\kappa}) & \text{if } \bar{\kappa} > 1. \end{cases} \quad (13)$$

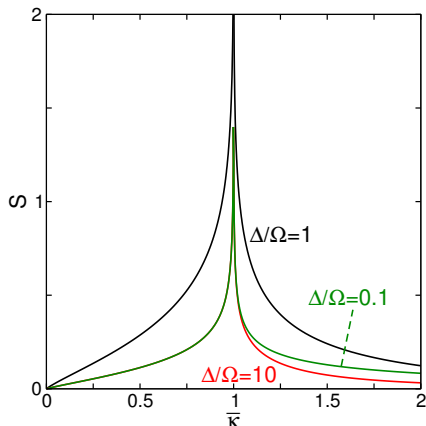


FIG. 2: Spin-oscillator entanglement entropy S for $j \rightarrow \infty$. For $\bar{\kappa} < 1$ curves with equal ratio Δ/Ω and $(\Delta/\Omega)^{-1}$ coincide. Note that S for $\bar{\kappa} > 1$ is given for the situation where one of the two opposite degenerate ground states is selected through inclusion of a small ϵJ_x term. Therefore, $S \rightarrow 0$ for $\bar{\kappa} \rightarrow \infty$.

The relevant observables (cf. Fig. 1) are $E_{\text{mf}} = -j\Delta$, $\langle J_z \rangle = -j$, $\langle J_x \rangle = 0$ for $\bar{\kappa} < 1$, and

$$E_{\text{mf}} = -\frac{1}{2}j\Delta(\bar{\kappa} + 1/\bar{\kappa}), \quad \langle J_z \rangle = -j/\bar{\kappa},$$

$$\langle J_x \rangle = \pm j\sqrt{1 - 1/\bar{\kappa}^2} \quad \text{for } \bar{\kappa} > 1. \quad (14)$$

The mean-field theory thus predicts a QPT transition at $\bar{\kappa} = 1$. This prediction is independent of j , which has dropped out of the mean-field equations entirely because of the particularly simple (j -independent) form of H_{mf}^s and H_{mf}^b . As we noted earlier the QPT transition is in fact realized only in the limit $j \rightarrow \infty$.

IV. QUANTUM CORRECTIONS TO THE CLASSICAL LIMIT

Mean-field theory becomes valid in the classical limit of large $j \rightarrow \infty$. At finite j correlations between the spin and oscillator occur together with non-classical spin and oscillator fluctuations.

The quantum corrections to the classical limit were obtained in Refs. [12–15] in leading order of a $1/j$ expansion using the Holstein-Primakoff (H-P) transformation of the spin operators. The H-P transformation gives

$$J_z = -j + b^\dagger b, \quad (15a)$$

$$J_x = \sqrt{\frac{j}{2}}(b^\dagger + b) + O(j^{-1/2}), \quad (15b)$$

for the spin operators in the Dicke Hamiltonian H , with new bosonic operators $b^{(\dagger)}$. In the symmetric phase ($\langle J_z \rangle = \langle a \rangle = 0$) we get the expansion

$$H = -j\Delta + H_{\text{qc}} + O(1/j), \quad (16)$$

with the bosonic Hamilton operator

$$H_{\text{qc}} = \Delta b^\dagger b + \frac{1}{2}\sqrt{\Delta\Omega\bar{\kappa}}(b^\dagger + b)(a^\dagger + a) + \Omega a^\dagger a \quad (17)$$

for the leading order quantum corrections. In the symmetry-broken phase spin (oscillator) operators have to be rotated (shifted) to the new equilibrium values first, before the Holstein-Primakoff transformation can be applied.

The two oscillators in H_{qc} can be decoupled with a unitary transformation of the form

$$U_2 = \exp[i(\gamma_1 X_1 P_2 + \gamma_2 P_2 X_1)]. \quad (18)$$

Then, the ground state of the transformed Hamiltonian $U_2 H_{\text{qc}} U_2^\dagger$ is a simple product state of two squeezed oscillator states. Back transformation with U_2 reintroduces the correlations present in the ground state of H_{qc} but absent in the product ground state of the transformed Hamiltonian.

A useful measure for correlations between the spin and oscillator, and thus for the relevance of quantum corrections to the mean-field state, is the spin-oscillator entanglement entropy

$$S = -\text{tr}[\rho_s \ln \rho_s]. \quad (19)$$

It is computed, e.g., from the reduced spin density matrix ρ_s after a trace over the bosonic degree of freedom. S is bounded by $S \leq \ln(2j + 1)$. The mean-field state gives $S = 0$ independently of j . In the limit $j \rightarrow \infty$ the entropy S converges to a value that can be computed from H_{qc} [15].

The entropy S , which is shown in Fig. 2, diverges at the QPT and thus provides a characterization of the QPT through the amount of quantum corrections to the classical limit [14]. Larger values of S in the vicinity of the QPT show that deviations from the mean-field state (5) occur not only for small j but remain important in the limit $j \rightarrow \infty$. The divergence of S at the QPT indicates the breakdown of the classical limit and of mean-field theory.

V. CORRELATED MEAN-FIELD THEORY

By construction, the mean-field ansatz does not account for spin-oscillator correlations. It also does not account for quantum fluctuations of the spin or oscillator at finite j . Indeed, we have seen in Sec. III that the assumption of a product state implies that the spin and oscillator are in coherent (i.e. classical) states. Therefore, to improve the mean-field ansatz one has to include spin-oscillator entanglement and correlations.

To go beyond mean-field theory we propose the variational ansatz

$$|\psi\rangle = D_x(\eta)|\phi\rangle \otimes |\chi\rangle \quad (20)$$

with the unitary transformation

$$D_x(\eta) = \exp[\eta J_x(a^\dagger - a)]. \quad (21)$$

The transformation depends on the variational parameter η ($\eta \in \mathbb{R}$). It can be interpreted as an oscillator shift that depends on the J_x -eigenvalues for $\eta \neq 0$. This J_x -dependence is the crucial difference to the mean-field ansatz, which is recovered for $\eta = 0$. It introduces spin-oscillator correlations and, thereby, allows for non-classical fluctuations. The spin state $|\phi\rangle$ and the oscillator state $|\chi\rangle$ remain to be determined in dependence on η . In particular, they will not be coherent states.

The above ansatz is partly modeled after the famous Lang-Firsov transformation of polaron physics, which describes the phonon-dressing of electronic states [16]. Here, the unitary transformation describes the dressing of the spin with bosons. We will later provide further justification for the above choice of the transformation through consideration of the $j \rightarrow \infty$ limit. A similar transformation has been used in Refs. [17–19] for the Rabi model ($j = 1/2$) at weak spin-oscillator coupling ($\bar{\kappa} \ll 1$), but the QPT was not addressed.

A. Entanglement entropy

The variational state (20) contains spin-oscillator correlations. This is exemplified by the fact that the spin-oscillator entanglement entropy S is non-zero for $\eta \neq 0$.

Working in the J_x eigenbasis $|m^x\rangle$, the reduced spin density matrix is given by

$$\begin{aligned} \rho_{mn} &= \langle m^x | \rho_s | n^x \rangle \\ &= \langle m^x | \phi \rangle \langle \phi | n^x \rangle \langle \chi | D(\eta(n-m)) | \chi \rangle, \end{aligned} \quad (22)$$

where $D(\cdot)$ is the standard oscillator displacement operator (cf. Eq. (A1)). For $\eta = 0$, $\rho_s = |\phi\rangle\langle\phi|$ is a pure state and $S = 0$. For $\eta \rightarrow \infty$, ρ_s evolves into a diagonal matrix with entries $|\langle m^x | \phi \rangle|^2$, and the entropy S becomes maximal for the given $|\phi\rangle$. Note that still $S \leq \ln(2j+1)$.

B. Variational equations

Instead of explicit transformation of the product state in Eq. (20) it is more convenient to consider the transformed Hamiltonian

$$\check{H} = D_x(-\eta) H D_x(\eta). \quad (23)$$

With the relations from App. B one finds

$$\begin{aligned} \check{H} &= \Delta J_z \cosh[\eta(a^\dagger - a)] + i\Delta J_y \sinh[\eta(a^\dagger - a)] \\ &\quad + \Omega a^\dagger a + (2\eta\kappa + \Omega\eta^2) J_x^2 \\ &\quad + (\kappa + \Omega\eta) J_x(a^\dagger + a). \end{aligned} \quad (24)$$

The original Hamiltonian is real, and therefore we can assume real states $|\phi\rangle$, $|\chi\rangle$. Then, the term $iJ_y \sinh[\eta(a^\dagger -$

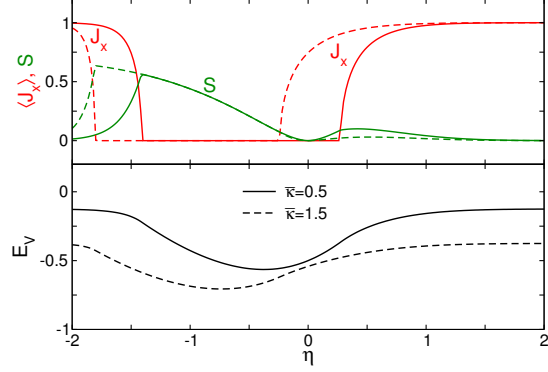


FIG. 3: Variational energy E_V , spin expectation value $\langle J_x \rangle$, and spin-oscillator entanglement entropy S as a function of η , for $j = 1/2$ and $\bar{\kappa} = 0.5$ (solid), $\bar{\kappa} = 1.5$ (dashed). In this and all following figures we use the Dicke model at resonance $\Omega = \Delta$, and measure energies in units of Δ or Ω equivalently.

$a]$ gives no contribution to the variational energy E_V , and thus drops out of the following equations.

Just as in the derivation of the mean-field ansatz we now obtain the spin state $|\phi\rangle$ as the ground state of an effective spin Hamiltonian

$$H_{\text{sp}} = \xi_1 J_z + \xi_2 J_x^2 + \xi_3 J_x, \quad (25)$$

with parameters

$$\begin{aligned} \xi_1 &= \Delta \langle \chi | \cosh[\eta(a^\dagger - a)] | \chi \rangle, \quad \xi_2 = 2\eta\kappa + \Omega\eta^2, \\ \xi_3 &= (\kappa + \Omega\eta) \langle \chi | a^\dagger + a | \chi \rangle. \end{aligned} \quad (26)$$

The oscillator state $|\chi\rangle$ is the ground state of an effective bosonic Hamiltonian

$$H_{\text{bos}} = \xi_4 \cosh[\eta(a^\dagger - a)] + \Omega a^\dagger a + \xi_5 (a^\dagger + a), \quad (27)$$

with parameters

$$\xi_4 = \Delta \langle \phi | J_z | \phi \rangle, \quad \xi_5 = (\kappa + \Omega\eta) \langle \phi | J_x | \phi \rangle. \quad (28)$$

The variational energy is

$$\begin{aligned} E_V &= \langle \psi | H | \psi \rangle = (\langle \phi | \otimes \langle \chi |) \check{H} (|\phi\rangle \otimes |\chi\rangle) \\ &= \langle \phi | H_{\text{sp}} | \phi \rangle + \Omega \langle \chi | a^\dagger a | \chi \rangle \\ &= \langle \chi | H_{\text{bos}} | \chi \rangle + \xi_2 \langle J_x^2 \rangle \end{aligned} \quad (29)$$

obtained either with H_{sp} or H_{bos} . Note that one could include $\Omega \langle \chi | a^\dagger a | \chi \rangle$ as a scalar constant in H_{sp} , or $\xi \langle J_x^2 \rangle$ as a constant in H_{bos} , to get a perfectly symmetric expression.

In contrast to the mean-field ansatz the ground states of the effective Hamiltonians H_{sp} , H_{bos} are no longer simple coherent states because of the J_x^2 and $\cosh[\cdot]$ term. Instead, we have to determine $|\phi\rangle$, $|\chi\rangle$ freely through a self-consistent computation of the respective ground

states. The parameters ξ_i of each effective Hamiltonian depend on expectation values formed with the respective other state, which results in a non-parabolic minimization problem. In practice, we can use a simple iterative strategy and determine the ground states of H_{sp} and H_{bos} alternately, always with the respective updated parameters ξ_1, ξ_2, ξ_3 or ξ_4, ξ_5 .

The result of such a computation for short spin $j = 1/2$ is shown in Fig. 3. The transformation parameter η is determined from the minimum of $E_V(\eta)$, given in the lower panel. Minima occur for $\eta < 0$. We observe the significant lowering of the energy in comparison to the mean-field energy at $\eta = 0$. More interestingly, at the optimal η -value the ansatz gives the correct result $\langle J_x \rangle \approx 0$ also for $\bar{\kappa} = 1.5 > 1$, in contrast to the wrong (and j -independent) prediction $\langle J_x \rangle / j \approx 0.75$ of mean-field theory, which fails completely for the $j = 1/2$ case. We also observe substantial values of S (it is $S \leq \ln 2 \approx 0.69$ for $j = 1/2$) at the optimal η : The ansatz succeeds because it includes spin-oscillator entanglement. We continue with the evaluation in Sec. VI.

Notice that for $j = 1/2$ the term $J_x^2 = 1/4$ is constant. Then, and only then, the effective spin Hamiltonian gives a spin coherent state $|\phi\rangle$ also for $\xi_2 \neq 0$. Nevertheless, the oscillator state $|\chi\rangle$ is not a coherent state but shows significant squeezing because still $\xi_4 \neq 0$ in Eq. (27). Simplifications occur in the two limiting cases discussed next.

C. The fast oscillator limit

In the limit of large Ω , the optimal $|\chi\rangle$ is the boson vacuum $|\text{vac}\rangle$. Then, the transformation parameter η occurs only in the term $(2\eta\kappa + \Omega\eta^2)J_x^2$ of H_{sp} , and energy minimization gives $\eta = -\kappa/\Omega$. The effective spin Hamiltonian now reads

$$H_{\text{sp}}^{\Omega=\infty} = \Delta J_z - \frac{\kappa^2}{\Omega} J_x^2. \quad (30)$$

This is the Lipkin-Meshkov-Glick model of nuclear physics [20]. Because we allow for free variation of $|\phi\rangle$, the variational ansatz here gives the exact ground state $|\phi\rangle \otimes |\text{vac}\rangle$ of \check{H} , and hence the exact ground state $|\psi\rangle$ of H . For $j < \infty$, $|\phi\rangle$ is not a spin coherent state.

We have discussed elsewhere [11] the two possible variations of the limit $\Omega \rightarrow \infty$ for $j = 1/2$ and $j > 1/2$, either with constant κ/Ω or constant κ^2/Ω , and their relation to the Lang-Firsov transformation of polaron physics.

D. The large spin limit

Second, consider the limit of large $j \rightarrow \infty$. In this limit, the transformation $D_x(\eta)$ assumes the form

$$D_x(\eta) \underset{j \rightarrow \infty}{=} \exp[\eta\sqrt{j/2}(b^\dagger + b)(a^\dagger - a)] \quad (31)$$

after H-P transformation. For the sake of the argument we assume being in the ordered phase, otherwise a spin rotation has to be applied first, similar to Sec. IV.

If we compare the above transformation to the transformation (18) we see that it gives only half of the transformation. It is not general enough to achieve full decoupling of the two harmonic oscillators in the Hamiltonian H_{qc} (Eq. (17)). However, the transformation $D_x(\eta)$ can achieve separation of the ground state of H_{qc} , which is all that is required for the variational ansatz.

As explained in App. C the appropriate choice of η gives the Hamiltonian

$$D_x(-\eta)H_{\text{qc}}D_x(\eta) = \omega_1 B^\dagger B + \lambda(B^\dagger A + BA^\dagger) + \omega_2 A^\dagger A + \text{const.} \quad (32)$$

Here, new bosonic operators $A^{(\dagger)}, B^{(\dagger)}$ appear as linear combinations of either the $a^{(\dagger)}$ or $b^{(\dagger)}$ operators. The actual computations are rather technical and collected in App. C.

Although the two oscillators are still coupled in the transformed Hamiltonian (32), its true ground state is a simple product state $|\phi\rangle \otimes |\chi\rangle$. Here, $|\phi\rangle, |\chi\rangle$ are the squeezed oscillator states annihilated by B and A , respectively. Because the coupling operator contains only terms with either A or B , it annihilates the product state. In the language of quantum optics the transformation $D_x(\eta)$ achieves elimination of the counter-rotating terms in H_{qc} .

Because of this property the variational ansatz (20) can give the correct ground state of H for large j including the leading order quantum corrections. This observation gives the justification for the particular form of $D_x(\eta)$ promised earlier.

VI. EVALUATION OF THE CORRELATED ANSATZ

We now continue the evaluation of the variational ansatz for finite j through comparison to quasi-exact data from numerical diagonalization of H .

To prevent ambiguities with the $j \rightarrow \infty$ limit above the QPT, we include a small symmetry breaking term ϵJ_x in $H + \epsilon J_x$, with $\epsilon = 10^{-3}$. This perturbation suffices to select one of the two nearly symmetry broken states for $\bar{\kappa} > 1$ and larger j , but does not affect results in the symmetric phase.

The results shown in Fig. 4 for $j = 1/2$ correspond to the situation of Fig. 3. Here, we plot the optimal results of the variational ansatz after the minimization over η has been performed. The agreement between the variational and exact results is very good in this case. The variational energy deviates from the true ground state energy by less than 0.4%, which is hundred times smaller than the deviation from the mean-field energy (with $\eta = 0$). This picture shows the overall success of the correlated variational ansatz: It gives near-exact results for the energy, spin-observables, and the spin-oscillator entangle-

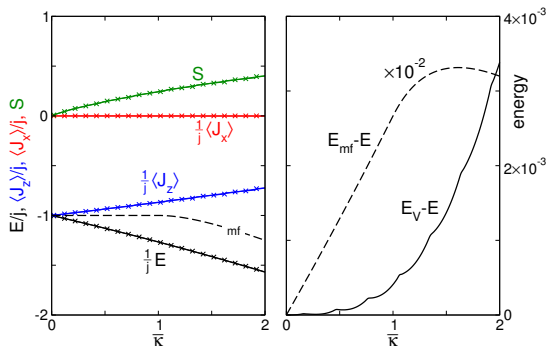


FIG. 4: Comparison of results from the variational ansatz to the true ground state from numerics, for $j = 1/2$. Left panel: Ground state energy E , spin expectation values $\langle J_z \rangle$, $\langle J_x \rangle$, and spin-oscillator entanglement entropy S as a function of coupling $\bar{\kappa}$. The crosses indicate the corresponding results from the variational ansatz. For orientation we include the mean-field energy (dashed curve). Right panel: Deviation $E_V - E$ of the variational energy E_V from the true energy E . For orientation the dashed curve gives the difference $E_{mf} - E$ to the mean-field energy, scaled by 10^{-2} to fit into the panel.

ment. In particular, it gives the correct $\langle J_x \rangle \approx 0$ where mean-field theory would predict symmetry breaking with large $\langle J_x \rangle$. The finite value of S shows that inclusion of spin-oscillator correlations through the unitary transformation $D_x(\eta)$ is the crucial step to go beyond mean-field theory.

The ansatz is however not perfect, and we report in Fig. 5 how it can fail for moderate spin length $j = 5$. There, we observe a jump in S and $\langle J_x \rangle$ at $\bar{\kappa} \approx 1.48$ while the true result is a continuous curve. The jump is accompanied by a small kink in the result for $\langle J_z \rangle$. We note that the variational energy remains very accurate: The deviation from the true ground energy is below 0.5% for all $\bar{\kappa}$, and even precisely at the jump it is still five times more accurate than the mean-field energy.

The origin of the artificial jump is depicted in Fig. 6, where the variational energy $E_V(\eta)$ is shown in the vicinity of the jump. A single minimum exists for smaller $\bar{\kappa}$, but a second minimum appears as $\bar{\kappa}$ approaches the jump value. Both minima switch the role of the global minimum at $\bar{\kappa} \approx 1.48$, and a first order phase transition with a jump is predicted where in reality no such transition occurs. At even larger $\bar{\kappa}$ the second minimum would disappear again. This behavior is a typical artefact of a variational ansatz, known, e.g., from polaron physics, the spin-boson model or general Hartree-Fock computations.

One should note that the energy is computed to much higher accuracy than other observable. This is, quite directly, the consequence of the variational approach: We optimize for the energy. In any case, the energy is not a very sensitive quantity and tiny energy changes can correspond to huge changes in other observables. Therefore, comparison of variational energies is not sufficient to argue for the quality of a variational ansatz.

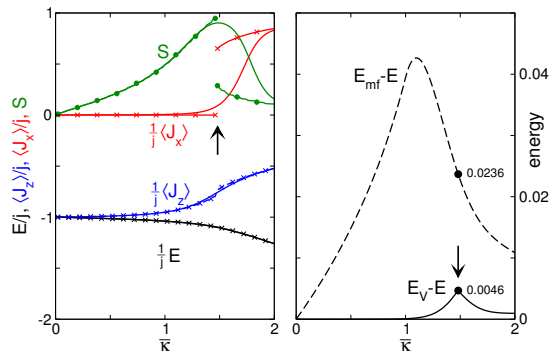


FIG. 5: Comparison of results from the variational ansatz to the true ground state from numerics as in the previous figure, now for $j = 5$. Left panel: Ground state energy E , spin expectation values $\langle J_z \rangle$, $\langle J_x \rangle$, and spin-oscillator entanglement entropy S as a function of coupling $\bar{\kappa}$. The crosses and circles indicate corresponding curves from the variational ansatz. The arrow indicates the “jump” at $\bar{\kappa} \approx 1.48$ of the variational results for S and $\langle J_x \rangle$. Right panel: Deviation $E_V - E$ of the variational energy E_V from the true energy E . The dashed curve gives the difference $E_{mf} - E$ to the mean-field energy. At $\bar{\kappa} = 1.48$, it is $E_V - E = 0.0046$ in comparison to $E_{mf} - E = 0.0236$.

As we have shown in Sec. VD the variational ansatz becomes exact in the large spin limit $j \rightarrow \infty$. Therefore, we expect that the artificial jump becomes less significant with increasing j . Fig. 7 shows that this expectation holds true. At $j = 40$ the jump is still present, but now it traces the true rapid change of S and $\langle J_x \rangle$ slightly above the QPT.

For even larger j the theoretical argument Sec. VD shows that we can observe convergence of the variational result for S towards the analytical result in the $j \rightarrow \infty$ limit. Note that the similar convergence of the $\langle J_x \rangle$ expectation value is not surprising: It only expresses the fact that this observable is obtained from mean-field theory for $j \rightarrow \infty$, and does not make a statement about the quality of the variational ansatz.

VII. CONCLUSIONS

For the example of the Dicke model we introduced and analyzed a correlated variational ansatz that extends mean-field theory with quantum correlations and fluctuations. The extension of mean-field theory is not arbitrary but controlled by the behavior in the $j \rightarrow \infty$ limit, where the variational ansatz gives correct results for the quantum corrections to the classical limit.

We show that the ansatz can give very good results not only for the ground state energy, but also for more crucial quantities such as the spin-oscillator entanglement. The agreement achieved there provides a better test for the quality of the variational ansatz than the near-exact results achieved for the ground state energy.

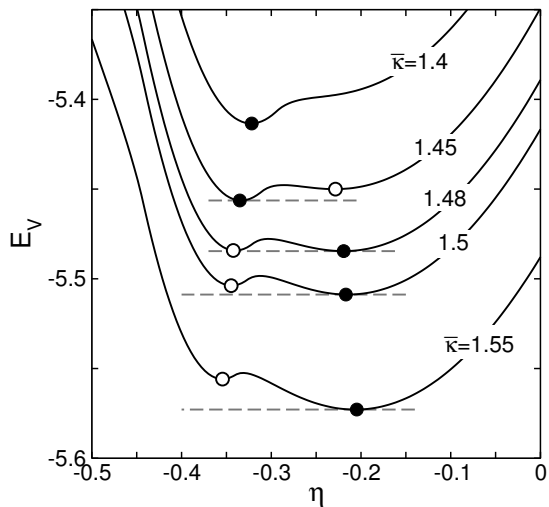


FIG. 6: Variational energy E_V as a function of η , for $j = 5$ and $\bar{\kappa} = 1.4, 1.45, 1.48, 1.5, 1.55$ as indicated. A circle marks a local minimum, a filled circle the global minimum of $E_V(\eta)$. Horizontal grey dashed lines give the respective minimal values of E_V .

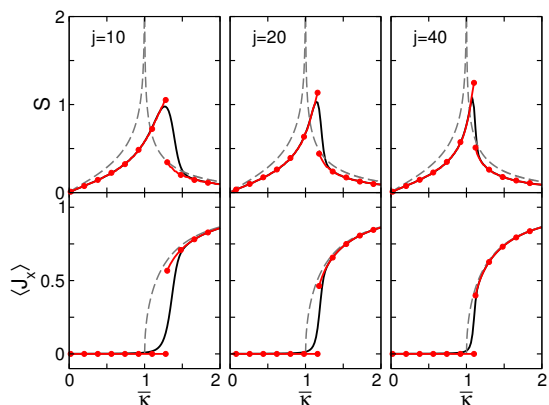


FIG. 7: Comparison of spin-oscillator entanglement entropy S (upper row) and spin expectation values $\langle J_x \rangle$ (lower row) from the variational ansatz (red curves with small circles) to the exact results from numerics (black curves). Curves are given for $j = 10, 20, 40$ in the left, middle, right column. The dashed grey curves in all panels gives the analytical $j \rightarrow \infty$ result for $\langle J_x \rangle$ and S .

Nevertheless, the ansatz still suffers from a typical error found with variational ansätze in general: An artificial jump, here in S and the $\langle J_x \rangle$ expectation value, that occurs whenever several minima appear in the variational energy and the global minimum changes discontinuously as the coupling is increased. This erroneous effect diminishes for larger spin, as expected from the construction of the ansatz. As we show analytically, the variational ansatz becomes exact for $j \rightarrow \infty$ including the leading quantum corrections.

In the present example, the jump of observables appears in spite of the high accuracy of the variational energy. This illustrates the general concerns one should have about a variational ansatz, for which it is sometimes hard to tell which results are real and which are artifacts. To overcome this problem one has to devise a scheme that allows for systematic improvement. The present ansatz is rigid in the sense that one cannot easily include more parameters in the unitary transformation, or additional variational degrees of freedom. Essentially the only way out of this situations would be to start from a linear combination of a few instead of the single product state in Eq. (20). In this way, also the reflection symmetry of the Dicke Hamiltonian could be explicitly accounted for in the variational ansatz.

However, it would be overkill to pursue this avenue for the Dicke model, which can be solved quasi-exactly with standard small-scale numerics. More interesting is the development of improved variational schemes for models such as the spin-boson model with a coupling to continuous bosonic degrees [21, 22]. The QPTs in these systems are different in nature from the QPT in the Dicke model, because they do not require a classical limit, and are still hard to tackle even with advanced numerical methods [23–25].

Acknowledgments

This work was supported by Deutsche Forschungsgemeinschaft via AL1317/1-2 and Sonderforschungsbereich 652.

Appendix A: Spin and oscillator coherent states

We use standard definitions of spin and oscillator coherent states (see Ref. [26] for a review).

An oscillator coherent state is defined through

$$|\alpha\rangle = D(\alpha)|\text{vac}\rangle = \exp[\alpha a^\dagger - \alpha^* a]|\text{vac}\rangle, \quad (\text{A1})$$

where $|\text{vac}\rangle$ is the boson vacuum. It is

$$\langle\alpha|a^\dagger|\alpha\rangle = \alpha^{(*)}. \quad (\text{A2})$$

In the main text, α is real.

A spin coherent state is defined through

$$|\theta\rangle = e^{i\theta J_y}|-j\rangle, \quad (\text{A3})$$

where $| -j \rangle$ is the J_z eigenstate with minimal eigenvalue $-j$. It is

$$\langle\theta|J_z|\theta\rangle = -j \cos \theta, \quad \langle\theta|J_x|\theta\rangle = j \sin \theta. \quad (\text{A4})$$

Only these spin coherent states, which result from a rotation around the y -axis, are needed in the main text.

Appendix B: Algebraic properties of the unitary transformation $D_x(\eta)$

Direct application of $e^A B e^{-A} = \sum_{n=0}^{\infty} (1/n!) [A, B]_n$, with iterated commutators $[A, B]_0 = B$, $[A, B]_{n+1} = [A, [A, B]_n]$, gives the transformation rules

$$D_x(-\eta) a^{(\dagger)} D_x(\eta) = a^{(\dagger)} + \eta J_x, \quad (\text{B1})$$

from which one gets

$$D_x(-\eta)(a^\dagger + a)D_x(\eta) = a^\dagger + a + 2\eta J_x, \quad (\text{B2})$$

and

$$D_x(-\eta)(a^\dagger a)D_x(\eta) = a^\dagger a + \eta J_x(a^\dagger + a) + \eta^2 J_x^2. \quad (\text{B3})$$

These rules depend only on the bosonic commutation relations and can be generalized for an arbitrary operator replacing J_x .

For the spin operator J_z one finds

$$\begin{aligned} D_x(-\eta) J_z D_x(\eta) &= J_z \sum_{n=0}^{\infty} \frac{1}{(2n)!} \eta^{2n} (a^\dagger - a)^{2n} \\ &\quad + i J_y \sum_{n=0}^{\infty} \frac{1}{(2n+1)!} \eta^{2n+1} (a^\dagger - a)^{2n+1} \\ &= J_z \cosh[\eta(a^\dagger - a)] + i J_y \sinh[\eta(a^\dagger - a)]. \end{aligned} \quad (\text{B4})$$

The simple form of this transformation rule depends on the spin commutation relations. It does not generalize to arbitrary operators.

Appendix C: Partial decoupling of H_{qc}

After the Holstein-Primakoff transformation the bosonic operator for the quantum corrections has the form

$$\begin{aligned} H_{\text{qc}} &= \omega_b b^\dagger b + \lambda(b^\dagger + b)(a^\dagger + a) + \omega_a a^\dagger a \\ &= \frac{1}{2}\omega_b(X_b^2 + P_b^2) + 2\lambda X_b X_a + \frac{1}{2}\omega_a(X_a^2 + P_a^2) - E_{\text{qc}} \end{aligned} \quad (\text{C1})$$

(cf. Eq. (17)), with parameters $\omega_a, \omega_b, \lambda$ that depend on $\Delta, \Omega, \bar{\kappa}$. Here, we introduced position and momentum operators as

$$X_a = \frac{1}{\sqrt{2}}(a^\dagger + a), \quad P_a = \frac{i}{\sqrt{2}}(a^\dagger - a), \quad (\text{C2a})$$

$$X_b = \frac{1}{\sqrt{2}}(b^\dagger + b), \quad P_b = \frac{i}{\sqrt{2}}(b^\dagger - b), \quad (\text{C2b})$$

and $E_{\text{qc}} = \frac{1}{2}(\omega_a + \omega_b)$. Notice the stability condition $4\lambda^2 < \omega_a \omega_b$ for a H_{qc} bounded from below. The specific form of H_{qc} in Eq. (C1) holds below the QPT. Above the

QPT an additional $(b + b^\dagger)^2$ term appears which can be accounted for by a redefinition of the X_b, P_b operators. The following argument does not change.

Our goal is to show that the ground state of H_{qc} can be written in the form $D_x(\gamma)[|\chi_b\rangle \otimes |\chi_a\rangle]$, where the unitary transformation is

$$D_x(\gamma) = \exp[i\gamma X_b P_a] = \exp[\frac{i}{2}\gamma(b^\dagger + b)(a^\dagger - a)] \quad (\text{C3})$$

(cf. Eq. (31)). The transformed Hamiltonian is

$$\begin{aligned} D_x(-\gamma) H_{\text{qc}} D_x(\gamma) &= \\ &\frac{1}{2}(\omega_b + \omega_a \gamma^2 - 4\lambda\gamma) X_b^2 + \frac{1}{2}\omega_b P_b^2 \\ &\quad + \frac{1}{2}\omega_a X_a^2 + \frac{1}{2}(\omega_a + \omega_b \gamma^2) P_a^2 \\ &\quad + (2\lambda - \omega_a \gamma) X_a X_b + \omega_b \gamma P_a P_b. \end{aligned} \quad (\text{C4})$$

Notice that all parameters are real.

Now make the ansatz

$$A = a_1 X_a + i a_2 P_a, \quad B = b_1 X_b + i b_2 P_b, \quad (\text{C5a})$$

$$A^\dagger = a_1 X_a - i a_2 P_a, \quad B^\dagger = b_1 X_b - i b_2 P_b, \quad (\text{C5b})$$

in the Hamiltonian

$$\begin{aligned} \tilde{H} &= B^\dagger B + \mu(B^\dagger A + B A^\dagger) + A^\dagger A \\ &= a_1^2 X_a^2 + a_2^2 P_a^2 + b_1^2 X_b^2 + b_2^2 P_b^2 \\ &\quad + 2\mu a_1 b_1 X_a X_b + 2\mu a_2 b_2 P_a P_b - \tilde{E}. \end{aligned} \quad (\text{C6})$$

Here, $\tilde{E} = a_1 a_2 + b_1 b_2$.

The ground state of \tilde{H} is a product state $|\chi_b\rangle \otimes |\chi_a\rangle$, where the two states $|\chi_{a/b}\rangle$ are those squeezed oscillator states that are annihilated by the operator A or B , respectively. Thus, to achieve the above goal, we must try to choose the transformation parameter γ in such a way that the transformed Hamiltonian from Eq. (C4) assumes the form of \tilde{H} . Comparison of the two expressions gives the condition

$$\frac{2\lambda - \omega_a \gamma}{\omega_b \gamma} = \frac{a_1 b_1}{a_2 b_2} = \frac{\sqrt{\omega_a(\omega_b + \omega_a \gamma^2 - 4\lambda\gamma)}}{\sqrt{\omega_b(\omega_a + \omega_b \gamma^2)}}, \quad (\text{C7})$$

or the equivalent equation

$$(2\lambda - \omega_a \gamma) \sqrt{\omega_b(\omega_a + \omega_b \gamma^2)} = \omega_b \gamma \sqrt{\omega_a(\omega_b + \omega_a \gamma^2 - 4\lambda\gamma)}. \quad (\text{C8})$$

Under the above stability condition the argument of the square root on the right hand side of the equation is always positive. The left and right hand side of the equation diverge towards opposite values $\pm\infty$ for $\gamma \rightarrow \pm\infty$, such that there is always a choice of γ to satisfy the above condition. Therefore, we have achieved our goal. We note that the specific value of γ can be obtained from a quadratic equation that follows from Eq. (C8). It could be used to fix the parameter η in Eq. (20) as an alternative to energy minimization, at least for large j .

-
- [1] S. Sachdev, *Quantum Phase Transitions* (Cambridge University Press, 2000).
- [2] A. P. Hines, R. H. McKenzie, and G. J. Milburn, *Phys. Rev. A* **71**, 042303 (2005).
- [3] R. Silbey and R. A. Harris, *J. Chem. Phys.* **80**, 2615 (1984).
- [4] R. F. Bishop, N. J. Davidson, R. M. Quick, and D. M. van der Walt, *Phys. Lett. A* **254**, 215 (1999).
- [5] O. Castaños, E. Nahmad-Achar, R. López-Peña, and J. G. Hirsch, *Phys. Rev. A* **84**, 013819 (2011).
- [6] E. Romera, R. del Real, and M. Calixto, *Phys. Rev. A* **85**, 053831 (2012).
- [7] O. Castaños, E. Nahmad-Achar, R. López-Peña, and J. G. Hirsch, *Phys. Rev. A* **86**, 023814 (2012).
- [8] K. Hepp and E. H. Lieb, *Annals of Physics* **76**, 360 (1973).
- [9] Y. K. Wang and F. T. Hioe, *Phys. Rev. A* **7**, 831 (1973).
- [10] R. H. Dicke, *Phys. Rev.* **93**, 99 (1954).
- [11] L. Bakemeier, A. Alvermann, and H. Fehske, *Phys. Rev. A* **85**, 043821 (2012).
- [12] C. Emary and T. Brandes, *Phys. Rev. Lett.* **90**, 044101 (2003).
- [13] C. Emary and T. Brandes, *Phys. Rev. E* **67**, 066203 (2003).
- [14] N. Lambert, C. Emary, and T. Brandes, *Phys. Rev. Lett.* **92**, 073602 (2004).
- [15] N. Lambert, C. Emary, and T. Brandes, *Phys. Rev. A* **71**, 053804 (2005).
- [16] I. G. Lang and Y. A. Firsov, *Zh. Eksp. Teor. Fiz.* **43**, 1843 (1962).
- [17] C. J. Gan and H. Zheng, *Eur. Phys. J. D* **59**, 473 (2010).
- [18] K. M. C. Lee and C. K. Law, *Phys. Rev. A* **88**, 015802 (2013).
- [19] L.-T. Shen, Z.-B. Yang, and R.-X. Chen, *Phys. Rev. A* **88**, 045803 (2013).
- [20] H. J. Lipkin, N. Meshkov, and A. J. Glick, *Nuclear Physics* **62**, 188 (1965).
- [21] A. J. Leggett, S. Chakravarty, A. T. Dorsey, M. P. A. Fisher, A. Garg, and W. Zwerger, *Rev. Mod. Phys.* **59**, 1 (1987).
- [22] U. Weiss, *Quantum Dissipative Systems* (World Scientific, 1999).
- [23] R. Bulla, N.-H. Tong, and M. Vojta, *Phys. Rev. Lett.* **91**, 170601 (2003).
- [24] A. Winter, H. Rieger, M. Vojta, and R. Bulla, *Phys. Rev. Lett.* **102**, 030601 (2009).
- [25] A. Alvermann and H. Fehske, *Phys. Rev. Lett.* **102**, 150601 (2009).
- [26] W.-M. Zhang, D. H. Feng, and R. Gilmore, *Rev. Mod. Phys.* **62**, 867 (1990).

Collapse-revival dynamics and atom-field entanglement in the nonresonant Dicke model

A. Alvermann*

Theory of Condensed Matter, Cavendish Laboratory, Cambridge CB3 0HE, United Kingdom

L. Bakemeier and H. Fehske

Institut für Physik, Ernst-Moritz-Arndt-Universität, 17487 Greifswald, Germany

(Received 16 August 2011; revised manuscript received 7 November 2011; published 3 April 2012)

We consider the dynamics of atomic and field coherent states in the nonresonant Dicke model. At weak coupling an initial product state evolves into a superposition of multiple field coherent states that are correlated with the atomic configuration. This process is accompanied by the buildup and decay of atom-field entanglement and leads to the periodic collapse and revival of Rabi oscillations. We provide a perturbative derivation of the underlying dynamical mechanism that complements the rotating wave approximation at resonance. The identification of two different time scales explains how the dynamical signatures depend on the sign of detuning between the atomic and field frequency and predicts the generation of either atomic or field cat states in the two opposite cases. We finally discuss the restrictions that the buildup of atom-field entanglement during the collapse of Rabi oscillations impose on the validity of semiclassical approximations that neglect entanglement.

DOI: [10.1103/PhysRevA.85.043803](https://doi.org/10.1103/PhysRevA.85.043803)

PACS number(s): 42.50.Pq, 03.67.Bg, 42.50.Dv

I. INTRODUCTION

In cavity quantum electrodynamics [1], where the confinement of atoms results in coherent coupling to a single field mode, optical signatures such as non-Poissonian photon statistics [2] or vacuum Rabi oscillations [3] allow for the direct observation of quantum effects on light-matter interaction. A fundamental consequence of field quantization is the collapse and revival (CR) of Rabi oscillations in a resonant cavity [4]. This effect, described by the Jaynes-Cummings model [5], involves the generation of atom-field entanglement and nonclassical “Schrödinger cat” states of the photon field [6]. In nonresonant cavities, on the other hand, the preparation of field cat states relies on linear frequency shifts induced by the atom-field coupling [7]. Additional effects arise in situations beyond weak coupling or resonance [8], but also for the superradiant quantum phase transition in atomic ensembles [9], which has a close connection to quantum chaos and critical entanglement [10].

In this paper we analyze the CR dynamics of atomic ensembles in the nonresonant Dicke model [11]. We identify the relevant CR mechanism that results from the weak-coupling correction to the bare atomic and field frequency. In difference to the behavior of a single atom studied in the Jaynes-Cummings model, more complex CR patterns are expected for atomic ensembles [12]. So far, they have been discussed only in the rotating wave approximation (RWA) [13,14], which is restricted to the near-resonant case.

The analysis of the nonresonant case provided here shows the importance of two different time scales for the CR dynamics. They are associated with the dynamical splitting of either field or atomic coherent states and the subsequent generation of field or atomic Schrödinger cat states. The effectiveness of the different dynamical mechanisms depends

on the sign of detuning: Atomic (field) cat states are generated predominantly if the field frequency is larger (smaller) than the atomic transition frequency. The former (latter) situation is further characterized by the buildup of significant atomic squeezing (atom-field entanglement) during the initial collapse phase. In both cases a periodic CR pattern develops on long time scales.

To understand these effects we proceed as follows. We first describe, in Sec. II, the principal behavior using numerical results for atomic expectation values, the entanglement entropy, and phase space distribution functions. These results establish Rabi oscillations and CR dynamics for the nonresonant case and indicate the evolution of an initial product state into a quantum superposition with large atom-field entanglement. We then deduce this behavior from the nonresonant weak-coupling perturbation theory developed in Sec. III and Appendix as the equivalent to the RWA at resonance. Perturbation theory allows for a clear identification of the relevant mechanisms and predicts the characteristic structure of the wave function as a quantum superposition of multiple classical field states. In Sec. IV we return to numerical calculations for the opposite cases of small or large field frequency. According to the two different time scales that we found in perturbation theory we will observe the realization of “Schrödinger cat”-like states of the atom or the field. Since atom-field entanglement plays a decisive role in the CR dynamics, we discuss in Sec. V the consequences for the standard semiclassical approximation to the Dicke model, which is found to encounter problems even close to the classical field limit. Our findings are summarized in Sec. VI.

II. COLLAPSE AND REVIVAL DYNAMICS

Atomic ensembles are described in the Dicke model [11],

$$H = -\Delta J_z + \lambda(a^\dagger + a)J_x + \Omega a^\dagger a, \quad (1)$$

as a pseudospin of length j (using angular momentum operators J_x, J_z), which represents an ensemble of $2j$ two-level atoms with transition frequency Δ coupled to a bosonic field

*Present address: Institut für Physik, Ernst-Moritz-Arndt-Universität, 17487 Greifswald, Germany; alvermann@physik.uni-greifswald.de

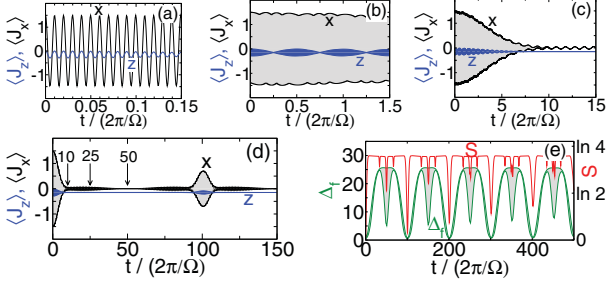


FIG. 1. (Color online) CR dynamics of three atoms ($j = 3/2$) for $\Omega/\Delta = 0.01$, $\lambda/\Delta = 0.01$, with $\theta_0 = \pi/2$, $\alpha_0 = 5.0$ in the initial state at $t = 0$. Upper row and lower left panel: Atomic expectation values $\langle J_x(t) \rangle$ (black curve marked “x”), $\langle J_z(t) \rangle$ (blue curve marked “z”) over different time scales, covering three orders of magnitude. Panels (b) and (c) show envelope functions because the fast atomic oscillations visible in panel (a) cannot be resolved in the pictures. Lower right panel: Entanglement entropy $S(t)$ (red curve) and field variance $\Delta_f(t)$ (green curve).

mode with frequency Ω (using ladder operators $a^{(\dagger)}$). We consider this model in the two different nonresonant cases $\Omega \ll \Delta$ and $\Omega \gg \Delta$.

An example of CR dynamics for $\Omega \ll \Delta$ is given in Fig. 1. In this and all following examples, the system at time $t = 0$ is prepared in the product state

$$|\psi(0)\rangle = |\theta_0\rangle \otimes |\alpha_0\rangle \quad (2)$$

of an atomic coherent state

$$\begin{aligned} |\theta_0\rangle &= \exp[-i\theta_0 J_y] |j, j\rangle \\ &= \sum_{m=-j}^j \binom{2j}{j+m}^{1/2} \left(\cos \frac{\theta_0}{2}\right)^{j+m} \left(\sin \frac{\theta_0}{2}\right)^{j-m} |j, m\rangle \end{aligned} \quad (3)$$

and a field coherent state

$$\begin{aligned} |\alpha_0\rangle &= \exp[\alpha_0 a^\dagger - \alpha_0^* a] |0\rangle \\ &= e^{-|\alpha_0|^2} \sum_{n=0}^{\infty} \frac{\alpha_0^n}{\sqrt{n!}} |n\rangle, \end{aligned} \quad (4)$$

using the J_z eigenstates $|j, m\rangle$ and the $a^\dagger a$ eigenstates $|n\rangle$ (cf. Ref. [15]). In the initial state it is $\langle J_z \rangle = j \cos \theta_0$, $\langle J_x \rangle = j \sin \theta_0$, and $\langle a \rangle = \alpha_0$. We assume that $|\alpha_0| \gg 1$ for a classical field and generally choose $\alpha_0 \in \mathbb{R}$, $\alpha_0 > 0$.

Figure 1 shows the atomic observables $\langle J_{x/z}(t) \rangle$ over different time scales. They have been calculated from numerical time propagation of the wave function using the Chebyshev technique [16]. Up to 10^3 bosons have been kept in the calculations to prevent errors from the truncation of the bosonic part of the Hilbert space. All numerical data shown are exact in the sense that the relative error is on the level of machine precision.

On a short time scale [panel (a)], we observe fast oscillations with the atomic frequency Δ . The amplitude of the $\langle J_z(t) \rangle$ oscillations is of order λ . On a longer time scale [panel (b)], the atomic oscillations in $\langle J_z(t) \rangle$ are modulated by oscillations with frequency Ω (note that we show envelope functions whenever the fast atomic oscillations are not resolved in the

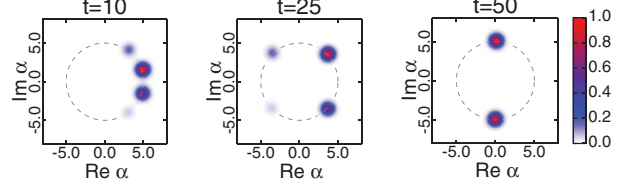


FIG. 2. (Color online) Field Husimi function $Q_f(\alpha)$ in the collapse phase for three atoms with parameters from Fig. 1, at times $t/(2\pi/\Omega) = 10, 25, 50$ corresponding to the arrows in the lower left panel in Fig. 1. The dashed circles have radius α_0 . The color encoding for $Q = 0$ through blue to red for the maximal Q value in the respective picture, as shown in the color bar on the right.

pictures). We call them Rabi oscillations in analogy to the resonant case because they arise from the coupling of the atoms to a classical field. In the nonresonant case $\Omega \ll \Delta$ they appear with the field frequency Ω . The collapse of Rabi oscillations is observable over the first 5 to 10 field periods $2\pi/\Omega$ [panel (c)], before they reappear on an even longer time scale [panel (d)], with a revival time of $T_R/(2\pi/\Omega) \approx 100$ field oscillations. In contrast to the resonant case, a periodic CR pattern of Rabi oscillations evolves.

The CR’s are accompanied by the periodic buildup and decay of atom-field entanglement (lower right panel in Fig. 1), which we measure through the entanglement entropy

$$S = -\text{Tr}[\rho_r \ln \rho_r]. \quad (5)$$

It is obtained from either the reduced atomic or field density matrix ρ_r , which both give the same value according to the Schmidt decomposition [17]. From the initial product state with $S = 0$, entanglement is generated in the collapse phase until S is close to the maximal possible value $\ln(2j + 1)$. The revivals coincide with entanglement decay, as the wave function returns to a product form. A similar behavior is found for the field variance, which we define as the product

$$\Delta_f = \frac{1}{2} \{\Delta[a^\dagger + a] \Delta[i(a^\dagger - a)]\}^{1/2} \quad (6)$$

of the uncertainties of the field operators $(a^\dagger + a)/\sqrt{2}$, $i(a^\dagger - a)/\sqrt{2}$, where $\Delta A = \langle A^2 \rangle - \langle A \rangle^2$ as usual. In Fig. 1 it signals that the initial coherent state with minimal $\Delta_f = 1/2$ evolves into a field state with large variance in the collapse phase.

To identify the structure of the bosonic field we show in Fig. 2 the field Husimi function [15]

$$Q_f(\alpha) = |\langle \alpha | \psi \rangle|^2. \quad (7)$$

By definition, it is the probability of finding the field in the coherent state $|\alpha\rangle$. For $\lambda = 0$, points in the phase space rotate on circles around the origin $\alpha = 0$. We observe that the Husimi function is a superposition of several Gaussian peaks indicating the splitting of the initial into multiple coherent field states in the collapse phase. Partial revivals, e.g., at $t = T_R/2 \approx 50 \times (2\pi)/\Omega$, occur when some but not all of the coherent field states merge. At a full revival $t = T_R$ (not shown), the Husimi function consists again of a single Gaussian peak at α_0 which indicates the revival of the initial state. This explains the behavior of the field variance Δ_f .

We observe here the first of two CR mechanisms. An initial coherent field state splits because the rotation frequency in

oscillator phase space depends on the atomic configuration. The field-induced collapse phase coincides with maximal entanglement between the atomic and several coherent field states whose phase space position differs by a finite angle. The large entanglement indicates an incoherent superposition rather than a field cat state that requires a coherent superposition [18]. Periodic revivals occur when the relative angles approach zero again.

III. NONRESONANT PERTURBATION THEORY

After the discussion of the first example, we now derive the CR mechanisms using perturbation theory. The central result will be that under the appropriate conditions for the perturbative treatment specified below, the wave function has the structure

$$|\psi(t)\rangle = \sum_{m=-j}^j \psi_m(t) |\sigma_m(t)\rangle \otimes |\alpha_m(t)\rangle, \quad (8)$$

where $|\sigma_m(t)\rangle$ are a set of atomic (i.e., spin) states that occur together with field coherent states $|\alpha_m(t)\rangle$. We note that the field remains essentially classical during time evolution since only coherent states occur, but it becomes entangled with the atomic ensemble because of the dependence of $\alpha_m(t)$ on m : Each classical field state is “tagged” by the associated atomic configuration $|\sigma_m(t)\rangle$.

A. Derivation of the perturbative wave function

The unperturbed eigenstates at zero coupling ($\lambda = 0$) are the product states $|m\rangle \otimes |n\rangle$ of J_z eigenstates $|m\rangle$ and field Fock states $|n\rangle$, with energy $E_{mn}^0 = -m\Delta + n\Omega$. From standard nondegenerate second-order perturbation theory we obtain the energy correction as

$$E_{mn}^{(2)} = \frac{\lambda^2}{8} \sum_{\mu\nu=\pm 1} \frac{(j - \mu m)(j + \mu m + 1)(2n + \nu + 1)}{\mu\Delta - \nu\Omega}, \quad (9)$$

where the sum contains contributions from the four states $|m \pm 1\rangle \otimes |n \pm 1\rangle$ contributing in second order through the interaction term $\lambda(a^\dagger + a)J_x$. The correction to the eigenstates is given by a similar expression, but we need to keep only the leading first-order terms in λ (further perturbative results are given in Appendix). Both expressions can be combined into a unitary time-evolution operator that gives the perturbative wave function as

$$|\psi(t)\rangle_{(2)} = U^\dagger \exp[-i\tilde{H}t]U|\psi(0)\rangle, \quad (10)$$

with an effective Hamiltonian

$$\tilde{H} = -\Delta J_z + \Omega a^\dagger a - \omega_E(2a^\dagger a + 1)J_z - \omega_S J_z^2 \quad (11)$$

and a unitary transformation of states

$$U = \exp\left[-\frac{2\omega_S}{\lambda}(a^\dagger - a)J_x - i\frac{2\omega_E}{\lambda}(a^\dagger + a)J_y\right]. \quad (12)$$

Here we introduced the two frequencies

$$\omega_E = \frac{\lambda^2\Delta}{2(\Delta^2 - \Omega^2)}, \quad \omega_S = \frac{\lambda^2\Omega}{2(\Delta^2 - \Omega^2)} \quad (13)$$

that appear in \tilde{H} as a consequence of the atom-field coupling and dropped a constant term $\Omega j(j+1)$. Due to the unitary

form of the perturbative result it remains valid for long times t and large $|\alpha_0|$, provided that $\lambda|\alpha_0| \ll |\Delta^2 - \Omega^2|$.

The central information about the nonresonant CR mechanism is contained in the two time scales

$$T_E = \frac{\pi}{|\omega_E|}, \quad T_S = \frac{\pi}{|\omega_S|} \quad (14)$$

in the effective Hamiltonian \tilde{H} . The “entangling” time T_E is associated with the term $a^\dagger a J_z$, which gives an energy correction $\propto mn$ and is the origin of the atom-dependent field splitting observed in Fig. 2. The “squeezing” time T_S occurs with J_z^2 . Since this term affects only the atomic ensemble, no additional entanglement is generated. Instead, it leads to the squeezing of atomic coherent states and splitting into atomic cat states [13,19]. The ratio $T_E/T_S = \Omega/\Delta$ determines which term dominates the initial dynamics. A similar perturbation theory for a simplified model in RWA does not distinguish between the different time scales [14] (see also Appendix).

We can now construct the perturbative wave function in the form of Eq. (8), starting from the initial state $|\psi(0)\rangle = |\theta_0\rangle \otimes |\alpha_0\rangle$ used throughout this paper. Under the assumption $|\alpha_0| \gg 1$ we can replace the operators $a^\dagger + a$, $i(a^\dagger - a)$ in the unitary transformation U from Eq. (12) by the scalars $2\text{Re}\alpha_0$, $2\text{Im}\alpha_0$, respectively. The error of this replacement is of order $1/|\alpha_0|$. Then, U reduces to a spin rotation operator of the form

$$R(a,b) = \exp[i(aJ_x - bJ_y)] \quad (a,b \in \mathbb{R}), \quad (15)$$

and we get

$$U[|\sigma\rangle \otimes |\alpha\rangle] = \left[R\left(\frac{4\omega_S \text{Im}\alpha}{\lambda}, \frac{4\omega_E \text{Re}\alpha}{\lambda}\right) |\sigma\rangle \right] \otimes |\alpha\rangle \quad (16)$$

for every atomic state $|\sigma\rangle$ and a field coherent state with $|\alpha| \gg 1$.

We note that general atomic coherent states can be defined through

$$|\theta, \phi\rangle = R(\theta \sin \phi, \theta \cos \phi) |j, j\rangle, \quad (17)$$

which gives

$$\begin{aligned} \langle \theta, \phi | J_z | \theta, \phi \rangle &= j \cos \theta, \\ \langle \theta, \phi | J_x | \theta, \phi \rangle &= j \sin \theta \cos \phi. \end{aligned} \quad (18)$$

Atomic coherent states remain coherent states under rotation. In particular for the initial state we have

$$U[|\theta_0\rangle \otimes |\alpha_0\rangle] = |\theta_0 + \delta\theta\rangle \otimes |\alpha_0\rangle \quad (19)$$

from the relation $R(0, \theta')|\theta\rangle = |\theta + \theta'\rangle$, a simple rotation of the atomic coherent state by the angle

$$\delta\theta = \frac{2\lambda\Delta\alpha_0}{\Delta^2 - \Omega^2}. \quad (20)$$

Here, we still assume for simplicity that $\alpha_0 \in \mathbb{R}$.

Since the effective Hamiltonian \tilde{H} is diagonal in the J_z eigenstates $|m\rangle$, application of $\exp[-i\tilde{H}t]$ to the state in Eq. (19) rotates the field component of the different J_z contributions. The operator $a^\dagger a$ generates a rotation of field coherent states of the form $\exp[i\xi a^\dagger a]|\alpha\rangle = |\exp(i\xi)\alpha\rangle$, such that we have

$$\exp[-i\tilde{H}t]|m\rangle \otimes |\alpha_0\rangle = e^{it(m(\Delta + \omega_E) + m^2\omega_S)} |m\rangle \otimes |\alpha_m(t)\rangle, \quad (21)$$

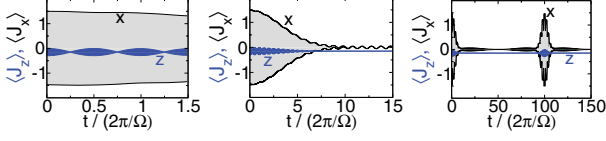


FIG. 3. (Color online) Perturbative result for the CR dynamics of three atoms with parameters from Fig. 1. Shown are the atomic expectation values $\langle J_x(t) \rangle$, $\langle J_z(t) \rangle$ obtained with Eqs. (8)–(25), corresponding to panels (b)–(d) in Fig. 1.

with

$$\alpha_m(t) = \alpha_0 e^{-it(\Omega - 2m\omega_E)}. \quad (22)$$

We note the scalar product

$$|\langle \alpha_m(t) | \alpha_{m'}(t) \rangle| = \exp[-|\alpha_0|^2 (1 - \cos \delta\alpha_{mm'})] \quad (23)$$

between two field coherent states enclosing the finite phase space angle $\delta\alpha_{mm'} = 2\pi(m - m')(t/T_E)$.

For each of the states in Eq. (21) the inverse transformation U^\dagger leads again to a spin rotation as in Eq. (16), but the arguments of $R(\cdot, \cdot)$ now depend on $\alpha_m(t)$. We have $U^\dagger |m\rangle \otimes |\alpha_m(t)\rangle = |\sigma_m(t)\rangle \otimes |\alpha_m(t)\rangle$ with

$$|\sigma_m(t)\rangle = R\left(-\frac{4\omega_S}{\lambda} \text{Im } \alpha_m(t), -\frac{4\omega_E}{\lambda} \text{Re } \alpha_m(t)\right) |m\rangle. \quad (24)$$

Collecting all results, we finally see that the perturbative wave function $|\psi(t)\rangle_{(2)}$ has indeed the structure proposed in Eq. (8), with individual terms given by Eqs. (22), (24) and

$$\psi_m(t) = e^{it[m(\Delta + \omega_E) + m^2\omega_S]} |m|\theta_0 + \delta\theta\rangle. \quad (25)$$

The coefficients $\langle m|\theta\rangle$ of an atomic coherent state are given in Eq. (3). We note that the spin states $|\sigma_m(t)\rangle$ are not orthogonal since the rotation with $R(\cdot, \cdot)$ depends on $\alpha_m(t)$. This effect is of order λ and not an artifact of perturbation theory.

B. Collapse and revivals in perturbation theory

Explicit expressions for the values of atomic and field observables can be derived from the above equations, but we do not show them here since they are rather lengthy and not very illuminating. Instead, let us focus on the CR dynamics in the situation $\Omega \ll \Delta$ addressed in Figs. 1 and 2. The perturbative result for atomic expectation values is shown in Fig. 3. Comparison with Fig. 1 shows that perturbation theory is in excellent agreement with the numerical data.

In the initial dynamics, for $t \ll T_E, T_S$, differences between the coherent state parameters $\alpha_m(t)$ are negligible. Therefore, the wave function has product form $|\psi(t)\rangle \approx |\sigma(t)\rangle \otimes |\alpha_0 e^{-i\Omega t}\rangle$. The atomic state $|\sigma(t)\rangle$ is obtained from the initial atomic coherent state $|\theta_0\rangle$ through three rotations around different axes: The first rotation from Eq. (19), the second rotation from the effective Hamiltonian as $\exp[it\Delta J_z]$, and the third rotation from Eq. (24) which currently does not depend on m . Therefore, $|\sigma(t)\rangle$ is itself an atomic coherent state as in Eq. (17). From Eq. (18) we obtain the atomic expectation values as

$$\begin{aligned} \langle J_z(t) \rangle &= j[\cos \Delta t \sin(\delta\theta \cos \Omega t) \sin(\theta_0 + \delta\theta) \\ &\quad + \cos(\delta\theta \cos \Omega t) \cos(\theta_0 + \delta\theta)], \end{aligned} \quad (26)$$

$$\begin{aligned} \langle J_x(t) \rangle &= j[\cos \Delta t \cos(\delta\theta \cos \Omega t) \sin(\theta_0 + \delta\theta) \\ &\quad - \sin(\delta\theta \cos \Omega t) \cos(\theta_0 + \delta\theta)]. \end{aligned} \quad (27)$$

These expressions describe, through the term $\delta\theta \cos \Omega t$, Rabi oscillations with frequency Ω . Their origin within perturbation theory is the dependence of the final rotation in Eq. (24) on $\alpha_m(t) \approx \alpha_0 e^{-i\Omega t}$ for $t \ll T_E$.

Since $\Omega \ll \Delta$, the term $a^\dagger a J_z$ determines the CR dynamics for times $t \sim T_E \ll T_S$. The splitting of the initial coherent field state $|\alpha_0\rangle$ into the $2j + 1$ coherent states $|\alpha_m\rangle$ is the source of entanglement with the atomic J_z eigenstates $|m\rangle$. Because different $|m\rangle$ states are orthogonal, the field is in an incoherent superposition. The collapse of Rabi oscillations is a consequence of the decreasing overlap $|\langle \alpha_m | \alpha_{m'} \rangle|$ from Eq. (23).

Deep in the collapse phase the overlap between different contributions $|\sigma_m\rangle \otimes |\alpha_m\rangle$ in Eq. (8) is negligible. As a consequence the phase of $\psi_m(t)$ in Eq. (25), and thus the term Δt responsible for atomic oscillations, drops out of the expressions. The atomic expectation values are now

$$\langle J_z(t) \rangle = \sum_{m=-j}^j m |\langle m|\theta_0 + \delta\theta\rangle|^2 \cos \xi_m(t), \quad (28)$$

$$\langle J_x(t) \rangle = \sum_{m=-j}^j m |\langle m|\theta_0 + \delta\theta\rangle|^2 \sin \xi_m(t), \quad (29)$$

with $\xi_m(t) = \delta\theta \cos(\Omega - 2\omega_E m)t$. Expanding $\cos \xi_m(t) = 1 + O(\lambda^2)$ we see that up to small corrections, $\langle J_z \rangle$ in the collapse phase is given by the constant value

$$\begin{aligned} \langle J_z(t) \rangle_{\text{collapse}} &= \sum_{m=-j}^j m |\langle m|\theta_0 + \delta\theta\rangle|^2 \\ &= \langle \theta_0 + \delta\theta | J_z | \theta_0 + \delta\theta \rangle = j \cos(\theta_0 + \delta\theta). \end{aligned} \quad (30)$$

This result is again a consequence of the rotation of the initial atomic coherent state in Eq. (19). For the parameters in Fig. 1 the expected value is $j \cos(\theta_0 + \delta\theta) \approx -0.15$, which is in full agreement with the numerical results. On the other hand, $\langle J_x(t) \rangle$ retains through the $\sin \xi_m(t)$ term of order λ the $\cos(\Omega t)$ dependence seen in the middle panel in Figs. 1 and 3.

For later times, inspection of Eqs. (22) and (23) shows that periodic revivals occur at multiples of T_E . For Fig. 1, the estimate $T_E = 100(2\pi/\Omega)$ is close to the numerical value. The appearance of a periodic CR pattern is a consequence of the linear dependence of $E_{mn}^{(2)}$ on both m, n , which is a significant difference from the RWA at resonance, where the energy correction $\propto \sqrt{n}$ prevents truly periodic revivals [6].

IV. GENERATION OF ATOMIC AND FIELD CAT STATES

The nonresonant perturbation theory from the previous section shows that in the opposite cases $\Omega \ll \Delta$ and $\Omega \gg \Delta$ either the term $\propto a^\dagger a J_z$ or $\propto J_z^2$ in the effective Hamiltonian \tilde{H} determines the dynamical properties over the respectively shorter time scale T_E or T_S . Both terms lead to a different structure of the wave function that is related to the generation of either field or atomic cat states. These cat states appear as linear combinations of well-separated atomic or field coherent states.

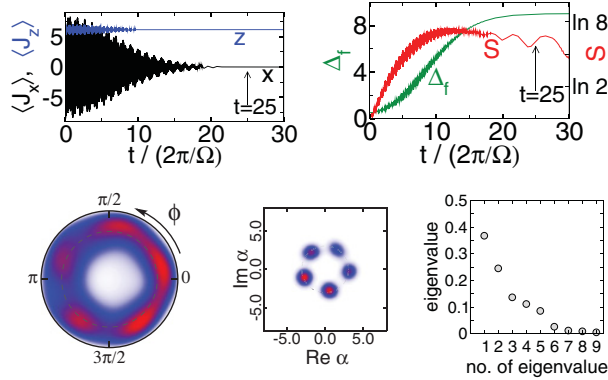


FIG. 4. (Color online) Formation of field cat states in the CR dynamics for $\Omega/\Delta = 1/20 \ll 1$, with $\lambda/\Delta = 0.02$, $j = 10$ and $\theta_0 = \pi/4$, $\alpha_0 = 3$. Upper panels: Spin expectation values $\langle J_{x/z} \rangle$ (left), entanglement entropy S and field variance Δ_f (right). Lower panels: Atomic and field Husimi function $Q_a(\theta, \phi)$ (left), $Q_f(\alpha)$ (middle) and Schmidt coefficients (right), at $t = 25 \times (2\pi/\Omega)$. For $Q_a(\theta, \phi)$, we show the hemisphere $0 \leq \theta \leq \pi/2$, with $\theta = 0$ in the center, $\theta = \pi/2$ on the outer circle, and $0 \leq \phi < 2\pi$ running counterclockwise as depicted. The gray dashed circle indicates $\theta = \pi/4$. The gray dashed circles in this and the following figures indicate $\theta = \pi/4$.

A “perfect” field cat state would, e.g., be the state $|\alpha\rangle \pm |-\alpha\rangle$ for $|\alpha| \gg 1$.

We have already discussed the case $\Omega \ll \Delta$ in some detail and will now revisit the structure of the wave function for the situation shown in Fig. 4. As expected, the collapse phase coincides with large atom-field entanglement and large field variance. The coherent state parameters $\alpha_m(t)$ in the wave function Eq. (8) differ by an angle that is a multiple of $2\pi(t/T_E)$. Whenever t/T_E is a rational number, some of the α_m are equal such that fewer coherent field states appear in the wave function. This explains the dips in the entanglement entropy $S(t)$ in Figs. 1 and 4.

At $t = 25 \times (2\pi/\Omega) \approx T_E/5$, the field Husimi function Q_f is a superposition of five Gaussian peaks. For the atomic state, a similar fivefold pattern cannot be clearly identified in the atomic Husimi function [15]

$$Q_a(\theta, \phi) = |\langle \theta, \phi | \psi \rangle|^2, \quad (31)$$

which is defined via atomic coherent states from Eq. (17) similar to the field Husimi function. It gives the pseudospin probability distribution as a function of spherical angle coordinates θ, ϕ . For $\lambda = 0$, the phase space sphere would rotate rigidly around the z axis passing through the origin $\theta = 0$.

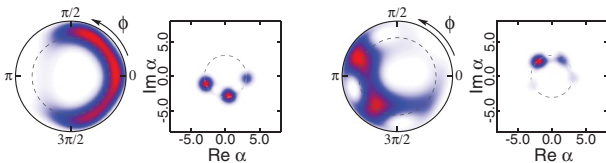


FIG. 5. (Color online) Atomic and field Husimi function of the two largest contributions in the Schmidt decomposition from Fig. 4, with respective weight 0.37 (left), 0.25 (right).

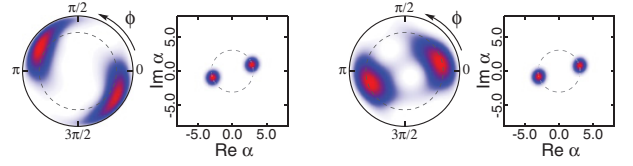


FIG. 6. (Color online) Atomic and field Husimi function of the two relevant contributions in the Schmidt decomposition at $t = 60 \times (2\pi/\Omega) \approx T_E/2$ (remaining parameters as in Fig. 4), with respective weight 0.65 (left), 0.32 (right).

If the atomic states $|\sigma_m(t)\rangle$ in Eq. (8) were mutually orthogonal the field superposition seen in Q_f would be completely incoherent. We know from perturbation theory that the states are not orthogonal due to the rotation with U^\dagger in Eq. (24), which allows for a coherent superposition and the appearance of field cat states. To check up on this possibility we use the Schmidt decomposition of the atomic and field wave function [17]. The Schmidt coefficients, i.e., the eigenvalues of both the atomic and field density matrix depicted by $Q_{a/f}$, have five relevant contributions. The two largest are shown separately in Fig. 5. We can identify a field cat state in the largest contribution (left panels), while the corresponding atomic state is strongly squeezed but not a cat state. In the second largest contribution the indication of an atomic cat state is visible. We also conclude that the fivefold field superposition in Fig. 4 is partially coherent.

Halfway through the collapse phase, for $t \approx T_E/2$, the two contributions shown in Fig. 6 comprise 98% of the wave function. Now, atomic and field cat states appear simultaneously. Note that the appearance of field cat states is again a consequence of the transformation U^\dagger in the perturbative result and the resulting nonorthogonality of the $|\sigma_m\rangle$ states in Eq. (8). Otherwise, the wave function would have the form $|\sigma_+\rangle|\alpha\rangle + |\sigma_-\rangle|-\alpha\rangle$ with two orthogonal atomic states $|\sigma_\pm\rangle$, and no field cat states could appear. Instead, the final rotation with U^\dagger in Eq. (24) leads to a finite overlap $\langle \sigma_+ | \sigma_- \rangle \neq 0$, and field cat states $\simeq |\alpha\rangle \pm |-\alpha\rangle$ occur in the Schmidt decomposition.

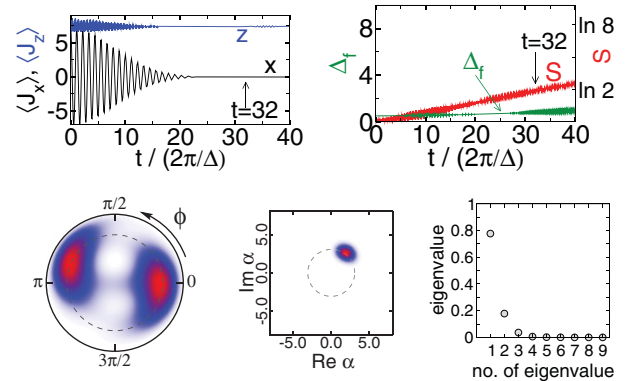


FIG. 7. (Color online) Formation of atomic cat states for $\Omega/\Delta = 20 \gg 1$, with $\lambda/\Delta = 0.5$, $j = 10$ and $\theta_0 = \pi/4$, $\alpha_0 = 3$ in the initial state. The panels show the same quantities as in Fig. 4, with $t = 32 \times (2\pi/\Delta)$ in the lower row.

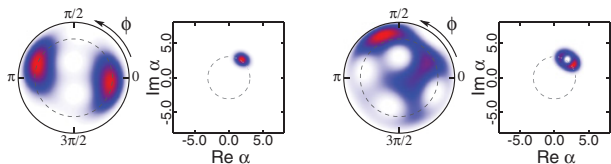


FIG. 8. (Color online) Atomic and field Husimi function of the two largest contributions in the Schmidt decomposition from Fig. 7, with respective weight 0.78 (left), 0.18 (right).

In the opposite case $\Omega \gg \Delta$, addressed in Fig. 7, the wave function remains close to a product form $|\sigma(t)\rangle \otimes |\alpha(t)\rangle$ for times $t \lesssim T_S \ll T_E$. The entanglement entropy and field variance are correspondingly small. In contrast to the initial short-time dynamics of Rabi oscillations in Eq. (26) that we deduced from the product form for times $t \ll T_S, T_E$, the term J_z^2 in \hat{H} now gives rise to squeezing and splitting of the initial atomic coherent state. In the situation shown in Fig. 7, the atomic Q function at $t = 32 \times (2\pi/\Delta) \approx T_S/2 \ll T_E$ has a twofold structure. It appears since, in the present case of integer even j ,

$$\exp\left[-i\frac{\pi}{2}J_z^2\right]|\theta\rangle = \frac{1}{1+i}|\theta\rangle + \frac{1}{1-i}|-\theta\rangle \quad (32)$$

is a linear combination of two atomic coherent states $|\theta\rangle, |-\theta\rangle$. The two relevant contributions in the Schmidt decomposition are shown in Fig. 8. As opposed to the previous case $\Omega \ll \Delta$, we identify the signatures of an atomic cat state together with a single coherent field state in the largest contribution (left panels). The annulus in Q_f for the second largest contribution (right panels) originates from a superposition of two field coherent states $|\alpha \pm \delta\alpha\rangle$ with $|\delta\alpha| \ll 1$. This structure is a precursor of the field state splitting through the $a^\dagger a J_z$ term for later times $T_S \lesssim t \lesssim T_E$.

V. ATOM-FIELD ENTANGLEMENT AND THE SEMICLASSICAL APPROXIMATION

The CR mechanism for $\Omega \ll \Delta$ does not depend on the nonclassical properties of a quantized field, but only on the possibility of atom-field entanglement. We thus expect that the basic signature of this mechanism, the collapse of Rabi oscillations, also occurs for atoms in strong radiation fields close to the classical field limit where the field quantization plays no role.

The classical field limit can be defined rigorously as the limit $|\alpha_0| \rightarrow \infty$, keeping $\lambda|\alpha_0|$ constant. In this limit, the field mode evolves independently of the atoms because the product $\lambda\langle J_x \rangle$, which gives the strength of the atomic influence on the field, goes to zero for $\lambda \rightarrow 0$ and finite j . The product $\lambda(a + a^\dagger)$, which determines the influence of the field on the atoms, remains finite. The Dicke model reduces to the model of an atomic ensemble driven by an external field $\mathbf{B}(t) = (2\lambda\alpha_0 \cos \Omega t, 0, -\Delta)$. The atomic expectation values $\mathbf{J} = (\langle J_x \rangle, \langle J_y \rangle, \langle J_z \rangle)$ obey the equation of motion

$$\partial_t \mathbf{J} = \mathbf{B}(t) \times \mathbf{J}. \quad (33)$$

The characteristic signatures of such a driven system are Rabi oscillations.

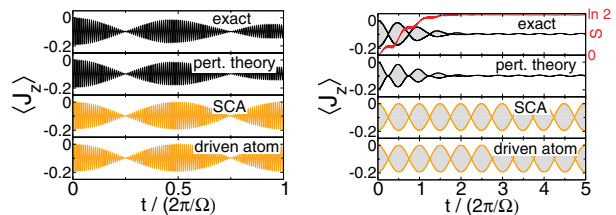


FIG. 9. (Color online) Comparison of the SCA to the exact dynamics of the Rabi model ($j = 1/2$) with $\Omega/\Delta = 0.01$, $\lambda/\Delta = 0.02$ and $\theta_0 = \pi/2$, $\alpha_0 = 5$. The left panels show $\langle J_z(t) \rangle$ over a short time interval, presenting the exact numerical, perturbative, and SCA result together with the result in the limit of a field-driven atom [Eq. (33)]. The right panels cover a longer time interval and include the entanglement entropy $S(t)$ (red curve) from the numerical calculation.

For finite α, λ the field mode does not evolve independently of the atoms, but we expect only small corrections from the classical field dynamics for small λ . One attempt to include these corrections is the semiclassical approximation (SCA) (see, e.g., Ref. [20] for a discussion). The SCA is based on the assumption that the coupled atom-field system remains in a product $|\theta(t), \phi(t)\rangle \otimes |\alpha(t)\rangle$ of coherent states during time evolution. This assumption allows for decoupling of the equations of motion for the atomic and field expectation values.

After decoupling, the atomic state evolves again similar to a spin in a magnetic field $\mathbf{B}(\alpha) = (2\lambda \text{Re}\alpha, 0, -\Delta)$. Now, however, the field state evolves as for an oscillator with an additional external force $\lambda\langle J_x \rangle$ that accounts for the back-reaction from the atomic ensemble. The corresponding SCA equations of motion are

$$\partial_t \mathbf{J} = \mathbf{B}(\alpha) \times \mathbf{J}, \quad i\partial_t \alpha = \Omega\alpha + \lambda\langle J_x \rangle. \quad (34)$$

The SCA equations of motion become exact in the classical field limit, where they reduce to Eq. (33).

From the equations of motions we can observe a potential problem of the SCA that arises from the generation of atom-field entanglement in the true Dicke dynamics. The change of the field state in Eq. (34) is $\propto \lambda$, and the influence on the atoms $\propto \lambda^2$. Therefore, the dynamically relevant time scale in SCA is $\propto 1/\lambda^2$, just as the scaling of the entangling time T_E from Eq. (14). We should thus expect that for time scales on which the SCA differs from the simpler Eq. (33) significant atom-field entanglement has been generated for which the SCA cannot account.

We consider exemplarily the limit $\Omega \rightarrow 0$ of a classical field with negligible energy quantization. In Fig. 9 we compare the SCA with the exact and perturbative result for the dynamics, and with the simplified Eq. (33) of a driven atomic ensemble. For short times (left panels) all four descriptions agree and describe Rabi oscillations, which are characteristic for classical field dynamics. For longer times (right panels), we see that significant entanglement is generated over the first few field periods even in the most simple Rabi case $j = 1/2$. The SCA cannot account for entanglement and accordingly misses the collapse of Rabi oscillations entirely. We note that the SCA simply reproduces the result also obtained with the simpler Eq. (33). Note also that we are in the weak coupling regime, where the nonresonant perturbation theory describes

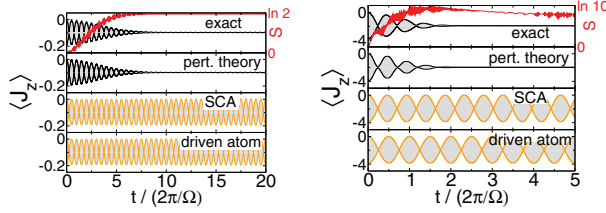


FIG. 10. (Color online) Comparison of the SCA to the exact dynamics, still with $\Omega/\Delta = 0.01$ and $\theta_0 = \pi/2$ as in Fig. 9. Left panels: Results for the Rabi model ($j = 1/2$) with $\lambda/\Delta = 0.005$ and $\alpha_0 = 20$. Right panels: Results for the Dicke model with $j = 10$, and other parameters $\lambda/\Delta = 0.02$ and $\theta_0 = \pi/2$, $\alpha_0 = 5$ identical to Fig. 9.

the dynamics accurately. The failure of the SCA is not a result of strong atom-field coupling.

A situation with larger α_0 is shown in the left panel in Fig. 10. The collapse of Rabi oscillations takes place for later times since T_E is larger, but both SCA and the simpler Eq. (33) again fail in the same way. In the right panel in Fig. 10 we see that this behavior is not restricted to the Rabi case, but occurs equally for $j \gg 1/2$. We note that its significance is not reduced since the present violation of classical field dynamics is not a consequence of quantum fluctuations of the atomic system, which would decay with $1/j$. The relevance of entanglement, bounded by $\ln(2j + 1)$, even increases with j .

The violation of the mean-field assumption of negligible atom-field correlations already at weak coupling presents a genuine problem for the SCA. As a consequence of entanglement generation, the SCA can be correct only as long as the field dynamics remains decoupled from the dynamics of the atomic ensemble. In that situation the atomic ensemble is already described by the simpler Eq. (33): The SCA does not improve on a model with entirely classical field dynamics where any influence of the atoms on the field state is neglected. We conclude that the SCA fails to account for the back-reaction of the atoms on the field, even at weak coupling or large j .

The nonresonant CR dynamics discussed here is an example of nontrivial coupled quantum-classical dynamics [21], as is evident from the wave function Eq. (8) with multiple coherent field states. In our case, the signatures of coupled quantum-classical dynamics are the periodic CR patterns which cannot be explained in a simple mean-field description.

VI. CONCLUSIONS

In summary, our analysis explains the CR patterns of Rabi oscillations in the nonresonant Dicke model by the dynamical splitting of atomic or field coherent states, which takes place on different time scales distinguished by the detuning ratio Ω/Δ . The collapse phase is accompanied by the buildup of atom-field entanglement or atomic squeezing, whose subsequent decay leads to periodic revivals. Both atomic and field cat states can arise in the collapse phase. The quantitative explanation of this behavior is provided by perturbation theory for large detuning. Application of the RWA to the nonresonant case would erroneously predict a single time scale (cf. Appendix), instead of the two time scales obtained in the correct calculation.

The nonresonant CR patterns arise through a dynamical mechanism that involves the creation of highly nonclassical states from initial classical state preparations. They give direct evidence for quantum entanglement and coherent quantum superpositions in atom-field and related systems. Even close to the classical field limit, where other quantum properties such as field quantization are of minor importance, atom-field entanglement can prevail over the semiclassical dynamics that would occur for a hypothetical noncorrelated atom-field system. This indicates how semiclassical approximations can fail because they neglect atom-field correlations.

The observation of nonresonant CR patterns might become possible in experiments using superconducting circuits instead of optical cavities [22]. These experiments can reach the regime of strong coupling or large detuning [23], which requires calculations beyond the RWA [24,25]. Although the experimentally controllable detuning can be made large, the most serious obstruction against observation of the dynamical patterns described here is the necessity of preserving quantum coherence over many Rabi oscillations. Further improvement of experimental techniques may resolve this issue.

ACKNOWLEDGMENTS

This work was supported by DFG through AL1317/1-1 and SFB 652.

APPENDIX: NONRESONANT PERTURBATION THEORY FOR DICKE-TYPE HAMILTONIANS

We give here the result of second-order perturbation theory for Dicke-type Hamiltonians

$$H = \omega J_z + \Omega a^\dagger a + g(a J_+ + a^\dagger J_-) + \bar{g}(a^\dagger J_+ + a J_-), \quad (\text{A1})$$

with $J_\pm = J_x \pm i J_y$ denoting spin ladder operators, in the nonresonant case $|\omega| \neq \Omega$.

Standard perturbation theory gives a correction to the eigenstates and eigenvalues of the noninteracting Hamiltonian in the first line in Eq. (A1). The result can be expressed in the form of Eq. (10), with a unitary transformation

$$U = \exp[T_1 + T_2] \quad (\text{A2})$$

that accounts for the change of the eigenstates, where

$$T_1 = \frac{g}{\omega - \Omega}(a J_+ - a^\dagger J_-) + \frac{\bar{g}}{\omega + \Omega}(a^\dagger J_+ - a J_-), \quad (\text{A3})$$

$$T_2 = \frac{g\bar{g}}{\omega^2 - \Omega^2} \left[\frac{\Omega}{2\omega} (J_+^2 - J_-^2) + \frac{\omega}{\Omega} (a^{\dagger 2} - a^2) J_z \right], \quad (\text{A4})$$

and an effective Hamiltonian

$$\begin{aligned} \tilde{H} = & \omega J_z + \Omega a^\dagger a + \frac{g^2(\omega + \Omega) + \bar{g}^2(\omega - \Omega)}{\omega^2 - \Omega^2} (2a^\dagger a + 1) J_z \\ & + \frac{g^2(\omega + \Omega) - \bar{g}^2(\omega - \Omega)}{\omega^2 - \Omega^2} (J_+^2 - J_-^2) \end{aligned} \quad (\text{A5})$$

that gives the perturbed eigenvalues. By construction, \tilde{H} is diagonal in the unperturbed eigenstates and contains only operators J_z and $a^\dagger a$, and the constant of motion J^2 . Perturbation theory thus provides us with an approximate diagonalization

of the Hamiltonian, in the sense that both sides of

$$U^\dagger \tilde{H} U = H + O(\{g, \bar{g}\}^3) \quad (\text{A6})$$

differ by terms of third or higher order in the coupling constants. Alternatively, the contribution of T_2 can be included in the effective Hamiltonian as in Ref. [25]. The present formulation with a diagonal \tilde{H} is preferential for the study of the dynamical evolution of the wave function since it allows for direct evaluation of Eq. (10).

Our Hamiltonian from Eq. (1) corresponds to the choice $g = \bar{g}$, including counter-rotating terms in H . The second-order term T_2 is finite and contributes to the atomic and field squeezing, but it appears as a higher-order correction to the leading-order term T_1 in U . Therefore, it is not relevant for the understanding of the dynamical effect discussed in the main part of the text and was not included in Eq. (12). Within the

perturbative setting the relevant second-order term in \tilde{H} , which grows during time evolution, is separated from the irrelevant second-order term in U .

In the RWA, applicable at resonance $\omega \approx \Omega$, counter-rotating terms are dropped from the Hamiltonian by setting $\bar{g} = 0$. In Refs. [13,14] an even simpler model with $\bar{g} = 0$ and $\Omega = 0$ was taken as the starting point. Within RWA, the term T_2 is zero in accordance with the fact that the number of excitations (corresponding to the operator $J_z + a^\dagger a$) is conserved. More importantly, the effective Hamiltonian now contains the same prefactor $g^2/(\omega - \Omega)$ in front of the two operators $a^\dagger a J_z$ and J_z^2 . Instead of the two different time scales for atomic and field squeezing introduced in Eq. (14) only a single time scale appears in the RWA. By construction, the RWA is valid only close to resonance and incompatible with the nonresonant perturbation theory.

-
- [1] H. Walther, B. T. H. Varcoe, B.-G. Englert, and T. Becker, *Rep. Prog. Phys.* **69**, 1325 (2006).
- [2] H. J. Carmichael, *Phys. Rev. Lett.* **55**, 2790 (1985); G. Rempe, F. Schmidt-Kaler, and H. Walther, *ibid.* **64**, 2783 (1990).
- [3] B. T. H. Varcoe, S. Brattke, M. Weidinger, and H. Walther, *Nature* **403**, 743 (2000).
- [4] G. Rempe, H. Walther, and N. Klein, *Phys. Rev. Lett.* **58**, 353 (1987); M. Brune, F. Schmidt-Kaler, A. Maali, J. Dreyer, E. Hagley, J. M. Raimond, and S. Haroche, *ibid.* **76**, 1800 (1996).
- [5] E. T. Jaynes and F. W. Cummings, *Proc. IEEE* **51**, 89 (1963); D. F. Walls and G. J. Milburn, *Quantum Optics* (Springer-Verlag, Berlin Heidelberg, 2008).
- [6] J. H. Eberly, N. B. Narozhny, and J. J. Sanchez-Mondragon, *Phys. Rev. Lett.* **44**, 1323 (1980); J. Gea-Banacloche, *ibid.* **65**, 3385 (1990).
- [7] M. Brune, S. Haroche, J. M. Raimond, L. Davidovich, and N. Zagury, *Phys. Rev. A* **45**, 5193 (1992); M. Brune, E. Hagley, J. Dreyer, X. Maître, A. Maali, C. Wunderlich, J. M. Raimond, and S. Haroche, *Phys. Rev. Lett.* **77**, 4887 (1996).
- [8] A. Wallraff, D. I. Schuster, A. Blais, L. Frunzio, R.-S. Huang, J. Majer, S. Kumar, S. M. Girvin, and R. J. Schoelkopf, *Nature* **431**, 162 (2004); I. Chiorescu, P. Bertet, K. Semba, Y. Nakamura, C. J. P. M. Harmans, and J. E. Mooij, *ibid.* **431**, 159 (2004).
- [9] K. Baumann, C. Guerlin, F. Brennecke, and T. Esslinger, *Nature* **464**, 1301 (2010).
- [10] C. Emary and T. Brandes, *Phys. Rev. Lett.* **90**, 044101 (2003); N. Lambert, C. Emary, and T. Brandes, *ibid.* **92**, 073602 (2004).
- [11] R. H. Dicke, *Phys. Rev.* **93**, 99 (1954).
- [12] P. L. Knight and B. W. Shore, *Phys. Rev. A* **48**, 642 (1993); T. Meunier, A. Le Diffon, C. Ruef, P. Degiovanni, and J.-M. Raimond, *ibid.* **74**, 033802 (2006); C. E. A. Jarvis, D. A. Rodrigues, B. L. Györfy, T. P. Spiller, A. J. Short, and J. F. Annett, *J. Opt. Soc. Am. B* **27**, A164 (2010).
- [13] G. S. Agarwal, R. R. Puri, and R. P. Singh, *Phys. Rev. A* **56**, 2249 (1997).
- [14] A. B. Klimov and C. Saavedra, *Phys. Lett. A* **247**, 14 (1998).
- [15] W.-M. Zhang, D. H. Feng, and R. Gilmore, *Rev. Mod. Phys.* **62**, 867 (1990).
- [16] H. Tal-Ezer and R. Kosloff, *J. Chem. Phys.* **81**, 3967 (1984).
- [17] R. Horodecki, P. Horodecki, M. Horodecki, and K. Horodecki, *Rev. Mod. Phys.* **81**, 865 (2009).
- [18] W. Schleich, M. Pernigo, and F. L. Kien, *Phys. Rev. A* **44**, 2172 (1991).
- [19] M. Kitagawa and M. Ueda, *Phys. Rev. A* **47**, 5138 (1993).
- [20] R. Graham and M. Höhnnerbach, *Z. Phys. B* **57**, 233 (1984).
- [21] L. Diósi, N. Gisin, and W. T. Strunz, *Phys. Rev. A* **61**, 022108 (2000).
- [22] R. J. Schoelkopf and S. M. Girvin, *Nature* **451**, 664 (2008).
- [23] A. A. Abdumalikov, O. Astafiev, Y. Nakamura, Y. A. Pashkin, and J. S. Tsai, *Phys. Rev. B* **78**, 180502 (2008).
- [24] J. Bourassa, J. M. Gambetta, A. A. Abdumalikov, O. Astafiev, Y. Nakamura, and A. Blais, *Phys. Rev. A* **80**, 032109 (2009).
- [25] D. Zueco, G. M. Reuther, S. Kohler, and P. Hänggi, *Phys. Rev. A* **80**, 033846 (2009).

Dynamics of the Dicke model close to the classical limit

L. Bakemeier,^{*} A. Alvermann, and H. Fehske

Institut für Physik, Ernst-Moritz-Arndt-Universität, 17487 Greifswald, Germany

(Received 7 May 2013; published 21 October 2013)

We study the dynamical properties of the Dicke model for increasing spin length, as the system approaches the limit of a classical spin. First, we describe the emergence of collective excitations above the ground state that converge to the coupled spin-oscillator oscillations found in the classical limit. The corresponding Green functions reveal quantum dynamical signatures close to the superradiant quantum phase transition. Second, we identify signatures of classical quasiperiodic orbits in the quantum time evolution using numerical time propagation of the wave function. The resulting phase-space plots are compared to the classical trajectories. We complete our study with the analysis of individual eigenstates close to the quasiperiodic orbits.

DOI: [10.1103/PhysRevA.88.043835](https://doi.org/10.1103/PhysRevA.88.043835)

PACS number(s): 42.50.Pq, 05.45.Mt, 73.43.Nq

I. INTRODUCTION

The relation between quantum dynamical systems and their classical counterparts is of fundamental interest, but also important for the understanding of the quantum dynamics itself. Specific questions concern the construction of and convergence to the classical limit [1,2], the relation between classical and quantum chaos [3,4], or between quantum chaos and thermalization [5–7]. This includes the identification of specific signatures of the classical dynamics, in particular of stable or unstable periodic orbits characteristic for regular or chaotic motion, in the eigenstates and quantum phase-space dynamics.

A paradigmatic example studied intensively in this context is the Dicke model [8] of quantum optics. The Dicke model, with Hamilton operator

$$H = \Delta J_z + \lambda(a^\dagger + a)J_x + \Omega a^\dagger a, \quad (1)$$

describes a spin (with operators J_x, J_z) of length j coupled to a harmonic oscillator (with bosonic operators $a^{(\dagger)}$). While the Dicke model acquires nontrivial behavior through the coupling of the spin to the oscillator, it remains accessible to analytical studies in the classical spin limit $j \rightarrow \infty$. In this limit, the Dicke model shows a quantum phase transition at the critical coupling $\lambda^2 = (\Delta\Omega)/2j$, from a ground state with zero bosonic expectation value ($\langle a \rangle = 0$) to a “superradiant” ground state with finite bosonic expectation value ($\langle a \rangle \neq 0$) [9,10]. This superradiant quantum phase transition (QPT) is accompanied by a divergence of spin-oscillator entanglement [11–13]. This is in contrast to the QPT in the “static” oscillator limit $\Omega \rightarrow 0$, which occurs already for finite spin length and shows no divergence of entanglement [14].

The Dicke model gives also an example for quantum chaotic behavior as seen in the level statistics [15–18]. The quantum chaos is accompanied by classical chaos in the corresponding semiclassical (SC) equations of motion for spin and oscillator expectation values [19]. It was further shown that classical chaos strongly influences the dynamics of entanglement [20,21] and spin squeezing [22]. The buildup and decay of entanglement is closely linked with the collapse and revival dynamics at finite j [23–25].

In this paper we study the dynamical properties of the Dicke model as the classical limit is approached. Our goal is to compare the quantum dynamics at large j with the SC dynamics in the limit $j \rightarrow \infty$. Our comparison includes the linearized dynamics around the ground state, seen as the collective response to a weak perturbation, and the full nonlinear dynamics in the entire phase space. With modern numerical tools, in particular Chebyshev algorithms for the computation of spectral functions [26] and time propagation [27], we can produce unbiased numerical results for large j (up to $j = 400$). This allows for a direct analysis of the emergence of “classical” behavior as the $j \rightarrow \infty$ limit is approached.

The paper is organized as follows. In Sec. II we discuss the SC equations of motion that hold in the limit $j \rightarrow \infty$. In Sec. III we compute the classical modes in the vicinity of the stationary state(s), and compare to the quantum-mechanical excitation spectrum that is given by a spin-spin Green function. In Sec. IV we address the quantum dynamics at higher energies. Convergence towards the classical dynamics is studied with the spin Husimi (phase-space) function, both for individual eigenstates and the time evolution of initial coherent states. We finally conclude in Sec. V. The Appendixes give details for the derivation of the SC equations of motion from the Dirac-Frenkel variation principle (Appendix A), for the computation of the classical collective modes (Appendix B), and for the numerical computation of the time averaged Husimi function through a modification of Chebyshev time propagation (Appendix C).

II. SEMICLASSICAL EQUATIONS OF MOTION

We first derive the SC equations of motion for the spin and oscillator expectation values. They are only an approximation to the true dynamics for finite j , but become exact in the limit $j \rightarrow \infty$ [28].

To obtain the SC equations of motion we can start with the Ehrenfest equations of motion $d\langle A \rangle/dt = i\langle [H, A] \rangle$ for the spin (J_x, J_y, J_z) and oscillator ($a^{(\dagger)}$) observables, e.g., $(d/dt)\langle J_y \rangle = \Delta\langle J_x \rangle - \lambda\langle (a^\dagger + a)J_z \rangle$.

The SC approximation consists in neglecting spin-oscillator correlations [28], replacing a mixed operator product $\langle AB \rangle$ by $\langle A \rangle\langle B \rangle$, e.g., $\langle (a^\dagger + a)J_z \rangle \mapsto \langle a^\dagger + a \rangle\langle J_z \rangle$ in the equation of

^{*}bakemeier@physik.uni-greifswald.de

motion for $\langle J_y \rangle$. This results in the SC equations of motion

$$\frac{d}{dt} \begin{pmatrix} \langle J_x \rangle \\ \langle J_y \rangle \\ \langle J_z \rangle \end{pmatrix} = \begin{pmatrix} 2\lambda \operatorname{Re}\langle a \rangle \\ 0 \\ \Delta \end{pmatrix} \times \begin{pmatrix} \langle J_x \rangle \\ \langle J_y \rangle \\ \langle J_z \rangle \end{pmatrix} \quad (2)$$

for the spin observables and

$$i \frac{d}{dt} \langle a \rangle = \Omega \langle a \rangle + \lambda \langle J_x \rangle \quad (3)$$

for the oscillator observables. Intuitively, the spin moves in the magnetic field generated by the oscillator, and the oscillator moves in the constant force exerted upon it by the spin. In this sense, the SC approximation gives a mean-field description of the system dynamics.

Equations (2) and (3) describe a five-dimensional dynamical system in the real variables $\langle J_{x,y,z} \rangle$, $\operatorname{Re}\langle a \rangle$, and $\operatorname{Im}\langle a \rangle$ with two conserved quantities, energy

$$E = \Delta \langle J_z \rangle + 2\lambda \operatorname{Re}\langle a \rangle \langle J_x \rangle + \Omega |\langle a \rangle|^2 \quad (4)$$

and spin length

$$j^2 = \langle J_x \rangle^2 + \langle J_y \rangle^2 + \langle J_z \rangle^2. \quad (5)$$

Note that the latter equation coincides with $\langle J^2 \rangle = j(j+1)$ only in the limit $j \rightarrow \infty$.

To eliminate one degree of freedom, using the conservation of j^2 , we switch to planar coordinates for the spin [29]. With spherical coordinates θ, ϕ and

$$\begin{pmatrix} \langle J_x \rangle \\ \langle J_y \rangle \\ \langle J_z \rangle \end{pmatrix} = \begin{pmatrix} j \cos \phi \sin \theta \\ j \sin \phi \sin \theta \\ -j \cos \theta \end{pmatrix}, \quad (6)$$

the complex variable

$$z = e^{-i\phi} \tan(\theta/2) \quad (7)$$

gives a mapping of the Bloch sphere onto the complex plane. We note $\langle J_x \rangle = 2j \operatorname{Re} z / (1 + |z|^2)$, $\langle J_y \rangle = -2j \operatorname{Im} z / (1 + |z|^2)$, and $\langle J_z \rangle = j(|z|^2 - 1) / (1 + |z|^2)$.

For the oscillator we introduce the complex variable

$$\bar{\alpha} = \frac{\Omega}{j\lambda} \langle a \rangle. \quad (8)$$

The prefactor guarantees a well-defined limit $j \rightarrow \infty$. We can identify $\bar{\alpha}$ with (the suitably scaled) position and momentum of the harmonic oscillator:

$$Q = \operatorname{Re} \bar{\alpha}, \quad P = \operatorname{Im} \bar{\alpha}. \quad (9)$$

Expressed in z and $\bar{\alpha}$, Eqs. (2) and (3) become

$$i \dot{\bar{\alpha}} = \Omega \left(\bar{\alpha} + \frac{2 \operatorname{Re} z}{1 + |z|^2} \right), \quad i \dot{z} = \Delta \left(z + \frac{\kappa}{2} (1 - z^2) \operatorname{Re} \bar{\alpha} \right). \quad (10)$$

Here, we introduced the dimensionless coupling constant

$$\kappa = \frac{2j\lambda^2}{\Delta\Omega}. \quad (11)$$

The quantum phase transition occurs at $\kappa = 1$. Conservation of spin length is imminent, and only four real dynamical variables remain. Note that j does not appear in the equations. Rescaling

of the time variable t would further allow the elimination of either Ω or Δ . The energy is given by

$$E(z, \bar{\alpha}) / (j\Delta) = \frac{|z|^2 - 1}{|z|^2 + 1} + 2\kappa \frac{\operatorname{Re} z \operatorname{Re} \bar{\alpha}}{1 + |z|^2} + \frac{\kappa}{2} |\bar{\alpha}|^2. \quad (12)$$

We note the parity symmetry $z \mapsto -z$ and $\bar{\alpha} \mapsto -\bar{\alpha}$ of Eqs. (10) and (12).

To shed further light on the meaning of the SC approximation, we stress that the SC equations of motion can also be derived from a time-dependent variational ansatz

$$|\psi_{\text{SC}}(t)\rangle = |\alpha(t)\rangle \otimes |z(t)\rangle \quad (13)$$

for the wave function. Here,

$$|\alpha\rangle = e^{-|\alpha|^2/2} e^{\alpha a^\dagger} |0\rangle \quad (14)$$

with $a|\alpha\rangle = \alpha|\alpha\rangle$ for $\alpha \in \mathbb{C}$ and

$$|z\rangle = (1 + |z|^2)^{-j} e^{zJ_+} |j, -j\rangle \quad (15)$$

denote oscillator and spin coherent states, respectively [29]. The relation between z and the spin observables is as in Eqs. (6) and (7), and the relation between $\alpha = \langle a \rangle$ and $\bar{\alpha}$ as in Eq. (8).

The time dependence of $|\psi_{\text{SC}}\rangle$ now follows from the Dirac-Frenkel time-dependent variational principle [30,31]. The equation of motion is

$$\frac{d}{dt} |\psi_{\text{SC}}\rangle = \mathcal{P} \frac{1}{i} H |\psi_{\text{SC}}\rangle, \quad (16)$$

where \mathcal{P} is the orthogonal projection onto the tangent space of the manifold of $|\psi_{\text{SC}}\rangle$ states. Evaluation of the projection (see Appendix A) recovers the equations of motion (10). The SC approximation is thus equivalent to the assumption that the system stays in a coherent product state as in Eq. (13) during time evolution. This explains the restrictions of the SC approximation, and hence part of the deviations between classical and quantum dynamics to be observed later.

III. CLASSICAL AND QUANTUM COLLECTIVE MODES

We now consider the classical dynamics in the vicinity of the stationary solutions of Eq. (10), and compare to the collective response of the Dicke model for small perturbations of the ground state.

A. Classical collective modes

Depending on the value of κ , Eq. (10) has one or two stable stationary solutions, which give the ground state of the Dicke model at zero temperature and in the limit $j \rightarrow \infty$. For $\kappa < 1$, the only stationary solution is $z = \bar{\alpha} = 0$. For $\kappa > 1$, this solution becomes unstable and the two stable solutions

$$z_{\pm} = \pm \sqrt{\frac{\kappa - 1}{\kappa + 1}}, \quad \bar{\alpha}_{\pm} = \mp \frac{\sqrt{\kappa^2 - 1}}{\kappa} \quad (17)$$

appear. Upon change of the value of κ , Eq. (10) thus displays a (supercritical) pitchfork bifurcation [32]. The appearance of stable solutions with $\langle a \rangle \neq 0$, which break the parity symmetry, signals the superradiant quantum phase transition at the critical coupling $\kappa = 1$.

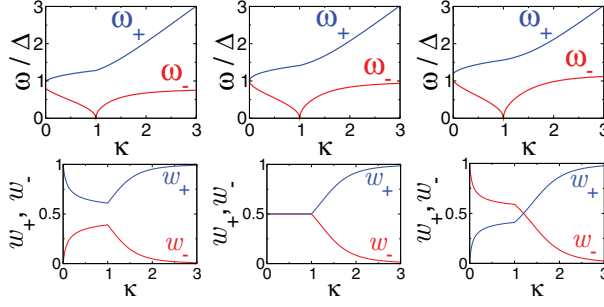


FIG. 1. (Color online) Collective mode frequencies ω_{\pm} from Eqs. (19) and (20) (upper row) and weights w_{\pm} from Eqs. (23), (24), and (25) (lower row) as a function of κ for $\Omega/\Delta = 0.8, 1.0, 1.2$ from left to right.

For small oscillations $z = z_s + \delta z$, $\bar{\alpha} = \bar{\alpha}_s + \delta \bar{\alpha}$ around a stationary solution $z_s, \bar{\alpha}_s$, linearization of Eq. (10) gives

$$\begin{aligned} i\delta\dot{\bar{\alpha}} &= \Omega \left(\delta\bar{\alpha} + \frac{2(1-z_s^2)}{(1+z_s^2)^2} \text{Re} \delta z \right), \\ i\delta\dot{z} &= \Delta \left((1 - \kappa \bar{\alpha}_s z_s) \delta z + \frac{\kappa}{2} (1 - z_s^2) \text{Re} \delta \bar{\alpha} \right). \end{aligned} \quad (18)$$

Equation (18) is a linear equation of motion for the deviations $\delta\bar{\alpha}$, δz , with purely imaginary eigenvalues (see Appendix B). They give the frequencies of small oscillations around the ground state of the Dicke model in the $j \rightarrow \infty$ limit. Two different modes exist, with frequencies

$$\omega_{\pm}^2 = \frac{\Omega^2 + \Delta^2}{2} \pm \sqrt{\left(\frac{\Omega^2 - \Delta^2}{2} \right)^2 + (\Delta\Omega)^2 \kappa} \quad (19)$$

for $\kappa < 1$, and

$$\omega_{\pm}^2 = \frac{\Omega^2 + (\Delta\kappa)^2}{2} \pm \sqrt{\left(\frac{\Omega^2 - (\Delta\kappa)^2}{2} \right)^2 + (\Delta\Omega)^2} \quad (20)$$

for $\kappa > 1$. The frequencies are plotted in Fig. 1. The appearance of a “soft mode” with $\omega_- = 0$ at $\kappa = 1$ signals the second order QPT. The frequencies obtained here directly from the SC equations of motion agree with the result obtained with a Holstein-Primakoff transformation of the spin operators in Ref. [18]. Both approaches are mathematically identical because they give, implicitly, the same linearized equations of motion around the stationary solutions of Eq. (10).

From the eigenvectors of Eq. (18) the full dynamical response can be determined (see Appendix B). Let us exemplarily focus on the response to a small rotation of the spin around the y axis, such that $J_x \mapsto J_x + \delta J_x$. Within the linear approximation of Eq. (18) it is

$$\frac{\delta J_x(t)}{\delta J_x(0)} = w_- \cos \omega_- t + w_+ \cos \omega_+ t, \quad (21)$$

with Fourier transform

$$\begin{aligned} \frac{\delta J_x(\omega)}{\delta J_x(0)} &= \frac{1}{\delta J_x(0)} \int_{-\infty}^{\infty} \delta J_x(t) e^{+i\omega t} dt \\ &= \pi w_- [\delta(\omega - \omega_-) + \delta(\omega + \omega_-)] \\ &\quad + \pi w_+ [\delta(\omega - \omega_+) + \delta(\omega + \omega_+)]. \end{aligned} \quad (22)$$

The Fourier transform has four δ peaks at frequencies $\pm\omega_{\pm}$. The weight w_{\pm} of the peaks, as shown in Fig. 1, is given by

$$w_- = \cos^2 \beta, \quad w_+ = \sin^2 \beta, \quad (23)$$

with

$$\tan 2\beta = \frac{2\Omega\Delta\sqrt{\kappa}}{\Omega^2 - \Delta^2} \quad (24)$$

for $\kappa < 1$ and

$$\tan 2\beta = \frac{2\Omega\Delta}{\Omega^2 - (\Delta\kappa)^2} \quad (25)$$

for $\kappa > 1$. Note that these equations determine the angle β only up to multiples of $\pi/2$. The correct choice is $0 \leq \beta \leq \pi/2$ for $\Omega \geq \Delta$ (with $w_- \rightarrow \Delta$, $w_- \rightarrow 1$ for $\kappa \rightarrow 0$) and $\pi/2 \leq \beta \leq \pi$ for $\Omega < \Delta$ (with $w_+ \rightarrow \Delta$, $w_+ \rightarrow 1$ for $\kappa \rightarrow 0$). At resonance $\Omega = \Delta$, it is $w_- = w_+ = 1/2$ for $\kappa < 1$ below the critical coupling. For $\kappa > 1$, the weight w_+ of the high-frequency peak grows, and $w_+ \rightarrow 1$, $w_- \rightarrow 0$ for $\kappa \rightarrow \infty$ (cf. Fig. 1).

B. Quantum collective modes

For a comparison of the quantum dynamics with the classical collective oscillations, we slightly disturb the ground state and then determine the time evolution of the wave function. With the operator for a spin rotation around the y axis

$$S(\theta) = e^{i\theta J_y}, \quad (26)$$

the initial state is given by

$$|\psi_{\delta}\rangle = S(\delta\theta)|\psi_0\rangle \quad (27)$$

for small $\delta\theta \ll 1$. The expectation value of J_x then is

$$J_x(t) = \langle \psi_{\delta}(t) | J_x | \psi_{\delta}(t) \rangle = \langle \psi_0 | S(-\delta\theta) J_x(t) S(\delta\theta) | \psi_0 \rangle. \quad (28)$$

Linearization for small $\delta\theta$ gives

$$\begin{aligned} J_x(t) &= \langle \psi_0 | (1 - i\delta\theta J_y) J_x(t) + J_x(t) (1 + i\delta\theta J_y) | \psi_0 \rangle \\ &= \langle \psi_0 | J_x | \psi_0 \rangle + i \langle \psi_0 | [J_x(t), J_y] | \psi_0 \rangle \delta\theta. \end{aligned} \quad (29)$$

The relevant quantity for comparison with the SC result in Eqs. (21) and (22) thus is the commutator Green function

$$\langle \langle J_x(t); J_y \rangle \rangle = i \langle \psi_0 | [J_x(t), J_y] | \psi_0 \rangle, \quad (30)$$

with Fourier transform

$$\begin{aligned} \langle \langle J_x; J_y \rangle \rangle_{\omega} &= \int_{-\infty}^{\infty} \langle \langle J_x(t); J_y \rangle \rangle e^{i\omega t} dt \\ &= 2\pi i \langle \psi_0 | J_x \delta[\omega - (H - E_0)] J_y | \psi_0 \rangle \\ &\quad - 2\pi i \langle \psi_0 | J_y \delta[\omega + (H - E_0)] J_x | \psi_0 \rangle. \end{aligned} \quad (31)$$

We note that $\langle \langle J_x(t); J_y \rangle \rangle \in \mathbb{R}$; hence $\langle \langle J_x; J_y \rangle \rangle_{\omega} = \langle \langle J_x; J_y \rangle \rangle_{-\omega}^*$, and have the sum rule

$$\int_{-\infty}^{\infty} \langle \langle J_x; J_y \rangle \rangle_{\omega} d\omega = -2\pi \langle J_z \rangle. \quad (32)$$

It is $\langle J_z \rangle < 0$ for $\Delta > 0$, as chosen here. For a real Hamiltonian such as for the Dicke model, time-reversal symmetry $\langle \langle J_x(-t); J_y \rangle \rangle = \langle \langle J_x(t); J_y \rangle \rangle^*$ holds, and $\langle \langle J_x; J_y \rangle \rangle_{\omega} \in \mathbb{R}$.

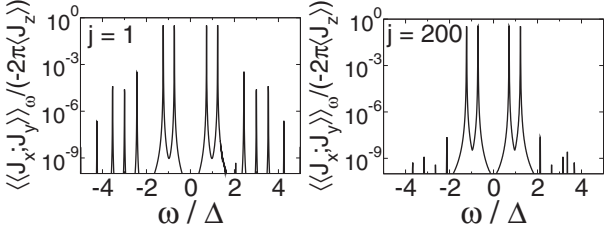


FIG. 2. Frequency spectrum of the normalized Green function as defined in Eq. (31), for $\Omega/\Delta = 1$, $\kappa = 0.95$ and $j = 1$ (left panel), $j = 100$ (right panel). The peaks are plotted with a finite width acquired from convolution with a narrow Gaussian.

The Green function is computed with the kernel polynomial method (KPM) [26], which allows us to treat large j . According to Eqs. (8) and (17) the average number of bosons in the ground state scales as $j\Delta/(2\Omega)(\kappa^2 - 1)/\kappa$ for $\kappa > 1$, in addition to significant bosonic fluctuations at the QPT [14]. Therefore, up to 10^3 bosons are kept in the calculation to ensure a negligible error from truncation of the infinite-dimensional Hilbert space. The spectral resolution of $\langle\langle J_x; J_y \rangle\rangle_\omega$ can be arbitrarily refined by increasing the number of Chebyshev moments.

For $j \rightarrow \infty$, the Green function should converge to the classical result from Eq. (22). Some care has to be taken about the correct normalization of $\langle\langle J_x; J_y \rangle\rangle_\omega$ in comparison to Eq. (22), because the relation between $\delta J_x(0)$ and $\delta\theta$ depends on the value of the stationary solution z_s . According to Eq. (6) it is $\delta J_x(0) = -\langle J_z \rangle \delta\theta$, which is just the factor from the sum rule for $\langle\langle J_x; J_y \rangle\rangle_\omega$. Therefore, we can use the normalized Green function $\langle\langle J_x; J_y \rangle\rangle_\omega / (-2\pi \langle J_z \rangle)$.

We show $\langle\langle J_x; J_y \rangle\rangle_\omega$ in Fig. 2 for small and large j . The function consists of several peaks, but a (pair of) two peaks close to the classical frequencies $\pm\omega_\pm$ from Eqs. (19) and (20) dominate the spectrum already at $j = 1$.

For a quantitative comparison with the classical limit, we show in Fig. 3 the peak positions and weights as extracted from $\langle\langle J_x; J_y \rangle\rangle_\omega / (-2\pi \langle J_z \rangle)$. We see that with increasing j , the quantum-mechanical Green function indeed converges to the result in the classic limit [Eq. (22)], in the sense that the weight of the dominant peaks increases and their position shifts towards the frequencies $\pm\omega_\pm$ of the classical collective modes. Since there is no QPT for finite j , convergence is slowest for κ in the vicinity of the critical $\kappa = 1$. For example, for $j = 100$, the peaks at $\pm\omega_\pm$ contribute 96% of the spectral weight for all $|\kappa - 1| > 0.4$, but only 79% for $\kappa \approx 1.06$. In particular, precursors of the “soft mode” with $\omega_- \rightarrow 0$ for $\kappa \rightarrow 1$ can be identified only for large $j \geq 200$.

The various energies in Fig. 3 correspond to quantized periodic motion around the one (below the QPT) or two (above the QPT) minima of the classical energy $E(z, \bar{\alpha})$ from Eq. (12). In principle, it should be possible to obtain these energies, and the corresponding wave functions and the peak weights w , with the Wentzel-Kramers-Brillouin approximation or other SC quantization schemes [33,34]. A comparison with the numerical data presented here would be most interesting in the vicinity of the phase transition, where deviations from the classical collective mode energies ω_\pm remain significant also for large j .

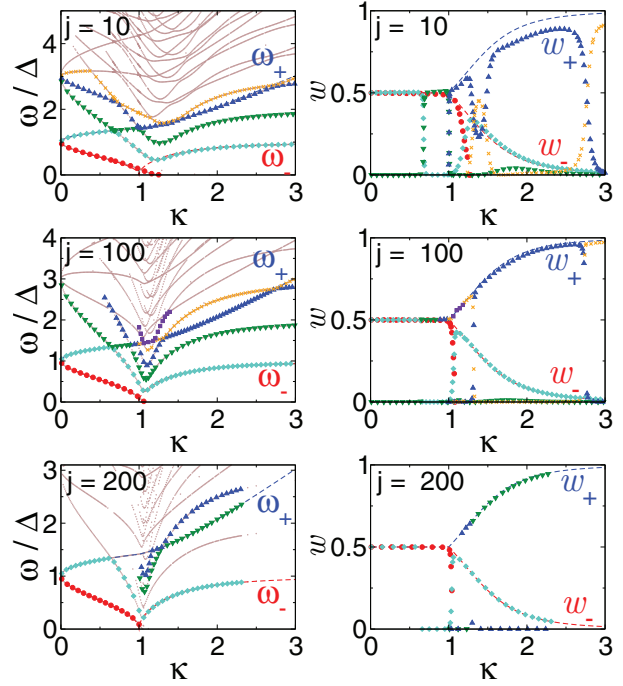


FIG. 3. (Color online) Position (left panel) and weight (right panel) of the peaks in the normalized Green function $\langle\langle J_x; J_y \rangle\rangle_\omega / (-2\pi \langle J_z \rangle)$, for $\Omega/\Delta = 1$ and $j = 10, 100, 200$ from top to bottom. The dashed lines show the classical frequencies ω_\pm and weights w_\pm from Eqs. (19)–(25). Those branches of the quantum excitation spectrum which gain significant weight are accentuated by colored symbols.

IV. CLASSICAL AND QUANTUM CHAOS

After our study of the dynamics in the vicinity of the ground state, we now turn to the general nonequilibrium dynamics for larger energies. In contrast to the linear response dynamics studied in the previous section, we can no longer expect a simple relation between the classical dynamics and the time evolution of quantum-mechanical expectation values. Additional corrections beyond the leading order of the SC approximation arise, e.g., from quantum diffusion in phase space [6,7] that leads to spreading of the wave function. These corrections manifest themselves in the time evolution of the wave function, but not in simple expectation values. Stable or unstable periodic orbits lead to different signatures in the quantum eigenstates [3,4], and require classification of individual eigenstates in particular for mixed classical dynamics where regular and chaotic orbits coexist at the same energy. Conversely, SC quantization schemes can be used to construct stationary or time-dependent wave functions along known classical orbits [33–35]. Therefore, we will compare classical orbits with phase-space distribution functions of the corresponding quantum orbits and eigenstates rather than the (spin) observables used in the previous section. To give a global picture of the dynamics we compare classical and quantum Poincaré plots.

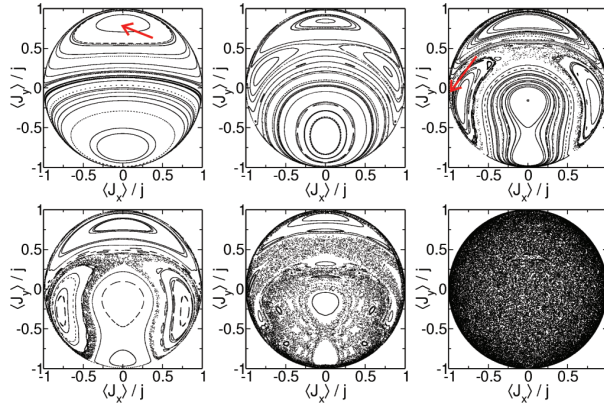


FIG. 4. (Color online) Top row: Poincaré plots for $E = -0.5$ and $\kappa = 0.1$ (left), $\kappa = 0.5$ (middle), $\kappa = 0.6$ (right). Bottom row: Poincaré plots for $\kappa = 0.6$ and $E = -1.0$ (left), $E = 1.0$ (middle), $E = 9.9$ (right). Red arrows denote the initial conditions for the orbits given in Fig. 5 below.

A. Classical dynamics

Depending on parameters and initial conditions, the SC equations of motion [Eq. (10)] predict regular or chaotic dynamics in the limit $j \rightarrow \infty$. This is illustrated by the Poincaré plots in Fig. 4, which are obtained from classical orbits to fixed energy $E = E(z, \bar{\alpha})$. Plotted are the values of $J_x(t)$, $J_y(t)$ at those times $t \geq 0$ when $Q(t) = \text{Re} \bar{\alpha}(t) = 0$. The knowledge of the four variables E , $J_x(t)$, $J_y(t)$, $Q(t)$ fixes the remaining variable $P(t) = \text{Im} \bar{\alpha}(t)$ because of energy conservation [cf. Eq. (12)]. The points in the plot are assembled from several orbits at the respective energy.

Regions with regular and chaotic motion can be discerned in the Poincaré plots. For large E all orbits are chaotic, but regular and chaotic dynamics coexist for smaller E . Two different orbits, a stable periodic orbit (left panel) and a chaotic orbit (right panel), are shown in Fig. 5. The stability of the classical orbits is characterized by the behavior of the (maximal) Lyapunov exponent $\Lambda(t)$ for $t \rightarrow \infty$, which we calculate with the “standard method” from Refs. [36,37]. In the present case, for a four-dimensional Hamiltonian system, the Lyapunov exponents appear in two pairs $\pm\Lambda_1(t)$, $\pm\Lambda_2(t)$. Two exponents $[\pm\Lambda_2(t)]$ vanish for $t \rightarrow \infty$ because motion along the orbit is stable [36]. For a regular orbit (left panel in Fig. 5) also $\pm\Lambda_1(t)$ vanish, while a chaotic orbit (right panel in Fig. 5) is characterized by a positive Lyapunov exponent $\Lambda_1(t) > 0$ in the limit $t \rightarrow \infty$. Note that the chaotic orbit is ergodic and fills the entire energy shell $E(z, \bar{\alpha}) = E$ [cf. Eq. (12)]. We next compare the two classical orbits to their quantum-mechanical counterparts for $j < \infty$.

B. Quantum dynamics

For the quantum dynamics, we start from a coherent product state

$$|\psi(0)\rangle = |\alpha(0)\rangle \otimes |z(0)\rangle, \quad (33)$$

whose parameters are chosen according to the classical initial condition. The relation to the spin and oscillator expectation

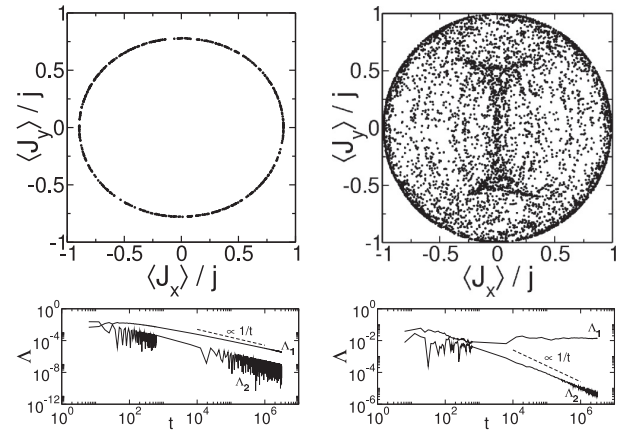


FIG. 5. Top row: Classical orbits for $E = -0.5$, $\kappa = 0.1$, $J_x(0) = 0.0$, $J_y(0) = 0.78$ (left panel) and $E = -0.5$, $\kappa = 0.6$, $J_x(0) = -0.987$, $J_y(0) = -0.065$ (right panel), corresponding to the arrows in the Poincaré plots in the previous figure. Shown is the trajectory in J_x - J_y phase space for $0 \leq t \leq 6000 \times 2\pi/\Delta$. Bottom row: Positive Lyapunov exponents $\Lambda_{1,2}$ for the two orbits as a function of time. The left orbit is regular with $\Lambda_{1,2} \rightarrow 0$ for $t \rightarrow \infty$; the right orbit is chaotic with $\Lambda_1 \rightarrow 0.014 > 0$.

values is given by Eqs. (7)–(9). We obtain the time evolution of $|\psi(t)\rangle$ numerically with Chebyshev time propagation [27,38].

In Fig. 6 we show the spin expectation values $\langle J_x(t) \rangle$, $\langle J_y(t) \rangle$ that constitute the quantum trajectory in comparison to the corresponding classical orbits from Fig. 5. The classical and quantum trajectory agree only over a short time period, whose length increases with j . As expected, the agreement is better for the stable orbit than for the chaotic orbit. Nevertheless, deviations occur even for the stable orbit already after a few periods (see lower left panel for $j = 300$). In difference to the

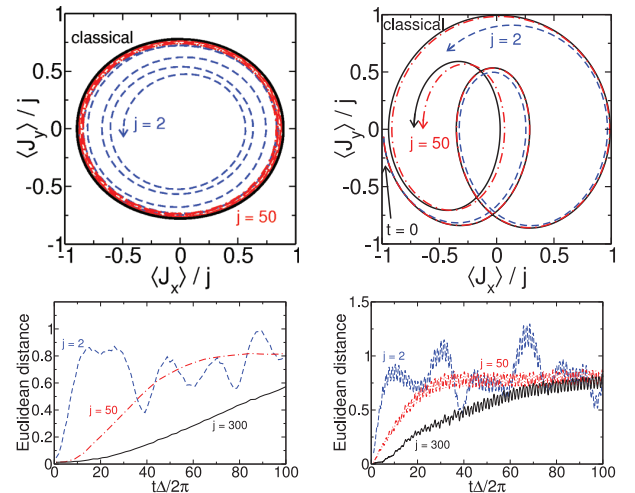


FIG. 6. (Color online) Comparison of the classical orbits from Fig. 5 to the spin expectation values $\langle J_x(t) \rangle$, $\langle J_y(t) \rangle$ from the quantum dynamics for the corresponding initial states as in Eq. (33). Shown are the classical (solid curves) and quantum (dashed curves) trajectories in J_x - J_y phase space (upper row) and the Euclidean distance between the trajectories as a function of time (lower row), for $j = 2, 50, 300$.

linear response situation studied in Sec. III, convergence of the quantum to the classical trajectory with increasing j is absent or slow.

This behavior can be traced back to the fact that the SC equations of motion coincide with the quantum time evolution only as long as the quantum state is approximately a coherent product state as in Eq. (13). Therefore, the classical and quantum trajectories agree only over a finite time T_E , the Ehrenfest time, which is of the order of a few spin periods $2\pi/\Delta$ in Fig. 6.

A better comparison of the quantum and classical time evolution is possible with phase-space functions. We use the spin Husimi function

$$Q(\theta, \phi; t) = |\langle \theta, \phi | \psi(t) \rangle|^2, \quad (34)$$

which gives the overlap with a coherent spin state $|\theta, \phi\rangle = |z\rangle$ in the spin phase space θ, ϕ [the relation to the complex variable z is as in Eq. (7)]. For a coherent state in the classical limit $j \rightarrow \infty$, $Q(\theta, \phi)$ shrinks to a point at the respective spin position. For $j < \infty$, the coherent state covers a phase-space volume $\propto 1/j$.

For the present study of the Dicke model we prefer the Husimi function over, e.g., the Wigner function [39] because it has a well-defined classical limit. As shown in Refs. [6,7] the exact time evolution of the joint spin-oscillator Husimi function $Q(z, \alpha, t)$ is determined by a Fokker-Planck equation with a classical drift and a quantum diffusion term. The quantum diffusion term vanishes for $j \rightarrow \infty$, and the Husimi function reduces to a classical probability function on phase space that obeys the Liouville equation. The equations of motion for the Wigner function contain higher-order derivatives that complicate the classical limit. Although the Wigner function is successfully used for other systems or the study of other aspects, such as the phase-space complexity of quantum dynamics [40,41], the comparison between the quantum and classical Dicke model is best performed with the Husimi functions.

In Fig. 7 we show the spin Husimi function for the two orbits from Fig. 6, for large spin length $j = 300$. We now observe convergence of the quantum to the classical dynamics, in the sense that the spin Husimi function traces out the phase-space region accessible to the classical orbits. However, classical phase-space drift and quantum diffusion lead to the spreading of the phase-space probability [6], such that the Husimi function at a single point of time t covers the entire orbit. Clearly, the values of t in Fig. 7 are beyond the Ehrenfest time. For the stable periodic orbit, the quantum state strictly expands along the one-dimensional classical trajectory in J_x - J_y phase space. The Husimi function remains localized on the classical orbit in spite of the spreading in phase space. Already at finite (though large) j we thus observe how the classical dynamics constrains the quantum dynamics: the quantum state spreads along, but not perpendicular to the classical orbit. We note that this behavior, which leads to zero spin expectation values due to the averaging over the entire orbit, is related to the collapse of Rabi oscillations for large j [25,42]. For the chaotic orbit, the Husimi function fills the entire energy shell also traversed by the classical orbit, which can be understood as a signature of (microcanonical) thermalization [6,7].

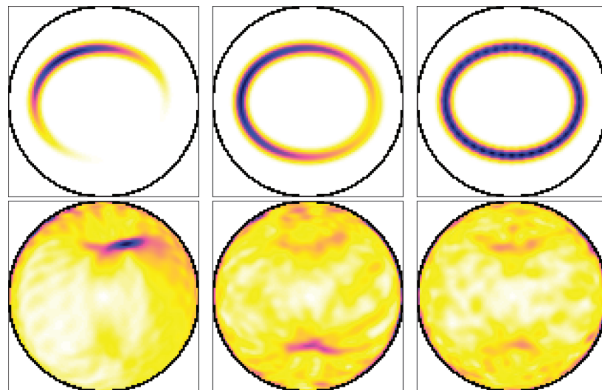


FIG. 7. (Color online) Spin Husimi function $Q(\theta, \phi; t)$ of the two orbits from Figs. 5 (upper panel) and 6 (lower panel), for $j = 300$ and for $t\Delta/(2\pi) = 50, 100, 200$ from left to right. Here and in the following figures we show the projection of $Q(\theta, \phi; t)$ onto the J_x - J_y plane. The angle θ runs from 0 in the center to $\pi/2$ on the outer circle. The angle ϕ runs counterclockwise from 0 at the top of the circle to 2π .

Spreading of the quantum state along the classical orbit explains why the Ehrenfest time is short even when convergence to the classical dynamics is observed in the phase-space functions. Because the classical drift term dominates the initial time evolution of the Husimi function for large spin length [6,7] the Ehrenfest time depends crucially on the associated classical motion [35]. For a chaotic orbit classical drift in the unstable directions dominates and the Ehrenfest time scales as $T_E \sim \Lambda^{-1} \ln(1/V)$, where Λ is the maximal Lyapunov exponent and V the initial phase-space volume. For a stable regular orbit the Ehrenfest time is determined by the much slower quantum diffusion along the orbit, which results in the scaling $T_E \sim 1/\sqrt{V}$. Indications of this difference between a regular and chaotic orbit can be seen already in Fig. 6.

To quantify the spreading of a quantum state we use the spin variance $\Delta J_{\parallel} = \langle J_{\parallel}^2 \rangle - \langle J_{\parallel} \rangle^2$ of a rotated spin operator

$$J_{\parallel} = \mathbf{n} \cdot \mathbf{J} = n_x J_x + n_y J_y + n_z J_z, \quad (35)$$

which is minimized over all the possible directions $\mathbf{n} = (n_x, n_y, n_z)^T$ with $|\mathbf{n}| = 1$. The variance ΔJ_{\parallel} is the minimum of a quadratic form in \mathbf{n} and given by the smallest eigenvalue of the 3×3 matrix,

$$\begin{pmatrix} \Delta_{x;x} & \Delta_{x;y} & \Delta_{x;z} \\ \Delta_{x;y} & \Delta_{y;y} & \Delta_{y;z} \\ \Delta_{x;z} & \Delta_{y;z} & \Delta_{z;z} \end{pmatrix}, \quad (36)$$

whose entries are the (mixed) spin operator variances

$$\Delta_{k;l} = \frac{1}{2} (\langle J_k J_l + J_l J_k \rangle - 2 \langle J_k \rangle \langle J_l \rangle). \quad (37)$$

The spin variance is invariant under rotation. It is $\Delta J_{\parallel} \geq 0$, and $\Delta J_{\parallel} = 0$ precisely for a spin coherent state.

In Fig. 8 we show the spin variance for the quantum dynamics corresponding to the two classical orbits in Fig. 5. For small spin length $j = 2$ the spin variance is identical for both orbits, reaching its maximum at about the same time. Going to large spin length $j = 400$ we observe the different scaling of the spin variance and thus the Ehrenfest time. For the

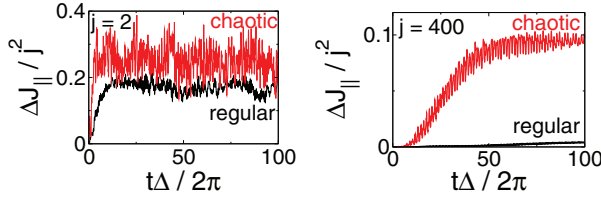


FIG. 8. (Color online) Spin variance $\Delta J_{||}$ as a function of time, for $j = 2$ (left) and $j = 400$ (right) with initial conditions corresponding to the regular and chaotic orbit in Fig. 5.

regular orbit the spin variance [at $t = 100(\Delta/2\pi)$] is reduced by a factor 0.02 and stays small during the plotted time interval. For the chaotic orbit the spin variance again grows quickly, and is only slightly smaller (by 0.4) than for $j = 2$. This is a clear sign of the different rates of spreading due to classical drift for chaotic and quantum diffusion for regular orbits.

Note that the quantum diffusion term in the Fokker-Planck equation respects the reversibility of the quantum dynamics [6,7]. Technically, this follows from the invariance under time reversal $t \mapsto -t$ combined with conjugation $z \mapsto z^*$, $\alpha \mapsto \alpha^*$ of the spin and oscillator phase-space coordinates, i.e., with $Q(z, \alpha, t)$ also the time-reversed Husimi function $Q(z^*, \alpha^*, -t)$ is a solution of the Fokker-Planck equation. In spite of this the time evolution shown in Fig. 7 and further below is indicative of irreversible dynamics because it starts from a highly untypical state such as the coherent states used here. In classical dynamics, chaotic mixing of trajectories leads to rapid spreading of the initially localized yet somewhat extended phase-space distribution at least on times scales smaller than the Poincaré recurrence time. The perceived irreversibility thus is a consequence of averaging over diverging trajectories starting from nearby phase-space points. For quantum chaotic systems with few degrees of freedom this kind of irreversibility is linked to the complex energy spectrum [43], as revealed in random matrix theory [4]. True irreversibility, involving the approach to a stationary equilibrium state, requires coupling to an infinite number of degrees of freedom provided, e.g., by a bath or the environment [44,45].

C. Classical and quantum periodic orbits

Because the quantum state traces out the classical orbit, periodic orbits that cover only a low-dimensional part of the phase space lead to distinct features in the quantum dynamics. For further illustration of the relation between classical and quantum dynamics we will, therefore, use the four (quasi-)periodic orbits shown in Fig. 9. The quantum signatures of these orbits are identified again with the spin Husimi function.

The spin Husimi function for the orbit from panel (a) is shown in Fig. 10, for increasing spin length j and time t . We clearly see the behavior described above, how the spin Husimi function traces out the classical trajectory for larger j . We also observe how the quantum state quickly loses the shape of the initial coherent state after the first few periods [e.g., for $t\Delta/(2\pi) = 10$ and $j = 400$], while it still follows the classical orbit.

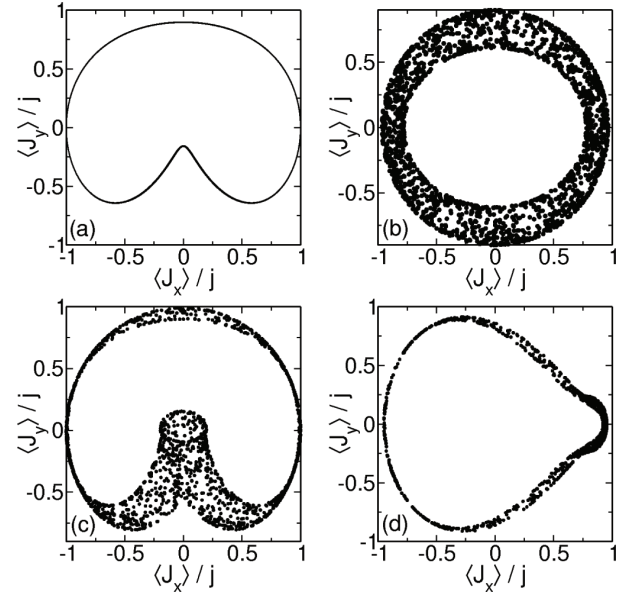


FIG. 9. Four quasiperiodic classical orbits in $J_x - J_y$ phase space, for $E = -0.5$ and $\kappa = 0.6$, $J_x(0) = 0$, $J_y(0) = 0.9$ (a), $\kappa = 0.1$, $J_x(0) = 0.0$, $J_y(0) = 0.9$ (b), $\kappa = 0.65$, $J_x(0) = 0.0$, $J_y(0) = 0.9$ (c), and $\kappa = 0.85$, $J_x(0) = 0.5$, $J_y(0) = 0.5$ (d).

Reminders of the quantum-mechanical dynamics are seen for large t (rightmost panels), where the spin Husimi function fragments into several “blobs” located on the classical trajectory [25]. This is a precursor of the revival of the initial state at much larger times, which occurs because for finite j the quantum dynamics explores only a finite-dimensional Hilbert space (the infinite-dimensional bosonic part is restricted by energy conservation).

The scenario of convergence in phase space generally holds for (quasi-) periodic orbits, as the spin Husimi functions in Fig. 11 for the remaining three orbits from Figs. 9(b), 9(c), and 9(d) show. The required waiting time after which the entire classical orbit can be identified in a “snapshot” of the quantum

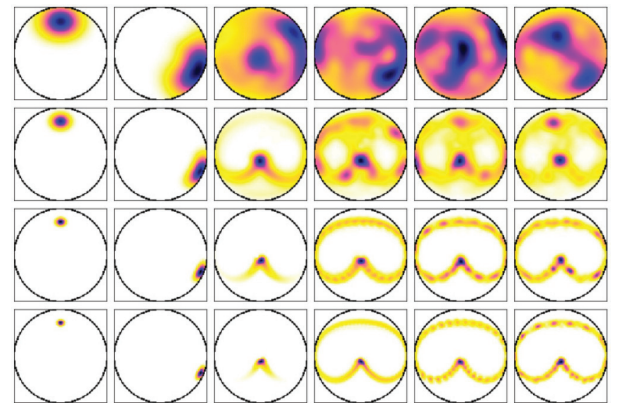


FIG. 10. (Color online) Spin Husimi function at time steps $t\Delta/2\pi = 0, 1, 10, 50, 100, 200$ (from left to right) and spin length (from top to bottom) $j = 10, 50, 200, 400$ (from top to bottom). The initial states correspond to the classical orbit from panel (a) in Fig. 9.

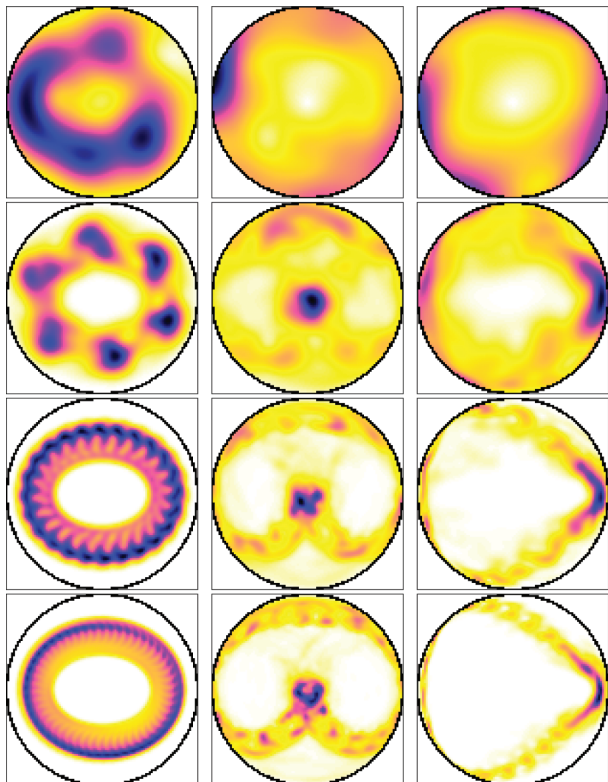


FIG. 11. (Color online) Spin Husimi functions for the three classical orbits from Figs. 9(b), 9(c), and 9(d), all at time $t = 200 \times 2\pi/\Delta$. The left, central, right column corresponds to the respective orbit in panels (b), (c), (d) in Fig. 9. From top to bottom, the spin length grows as $j = 10, 50, 200, 400$.

dynamics at time t can become nevertheless large, depending on the rapidity of phase-space diffusion. Therefore, the plots in Fig. 11 already show fragmentation of the Husimi function, indicating the later revival of the initial state.

To identify the classical orbit from the quantum time evolution already at earlier times we can use the time-averaged Husimi function

$$\bar{Q}(\theta, \phi) = \frac{1}{2T} \int_{-T}^T dt Q(\theta, \phi; t), \quad (38)$$

where T is of the order of a few periods. $\bar{Q}(\theta, \phi)$ can be directly computed from the Chebyshev time propagation (see Appendix C), which is a more elegant numerical approach than sampling and averaging of $Q(\theta, \phi; t)$ at many values of t . The time-averaged Husimi function as shown in Fig. 12 now gives a clear picture of the classical trajectory as it is (re-)constructed from the quantum trajectory in J_x - J_y phase space.

D. Quantum states close to periodic orbits

Because the time evolution of a quantum state is directly related to the eigenstates of the Hamiltonian, the same signatures that appear in the time-dependent Husimi function should show up in the individual eigenstates. Therefore, we finally try to relate the different classical orbits with energy E to the eigenstates $H|E_n\rangle = E_n|E_n\rangle$ with nearby energies

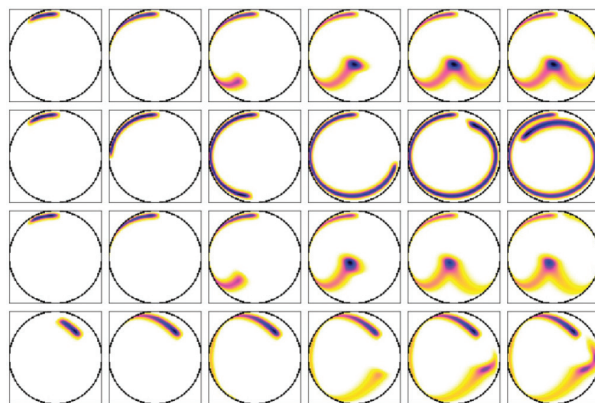


FIG. 12. (Color online) Time-averaged spin Husimi function as defined in Eq. (38) for $j = 100$ and $T\Delta/(2\pi) = 0.1, 0.25, 0.5, 0.75, 1.0, 1.25$ from left to right. The rows, from top to bottom, correspond to the classical orbits in panels (a)–(d) in Fig. 9.

$E_n \approx E$. We use two different spin Husimi functions to characterize the eigenstates, which give correspondence either to the classical orbits or the Poincaré plots.

The spin Husimi function

$$Q_n^{\text{spin}}(\theta, \phi) = |\langle \theta, \phi | E_n \rangle|^2 \quad (39)$$

for the eigenstates $|E_n\rangle$ directly corresponds to the time-dependent spin Husimi function from Eq. (34). In Fig. 13 we show the Husimi functions for different eigenstates in the energy range $-0.703 < E_n < -0.249$. The eigenstates are arranged according to their overlap with classical orbits to energy $E = -0.5$. Both regular (a)–(c) and chaotic (d)–(e) orbits appear in the figure because of the classical “mixed” dynamics (recall the Poincaré plot in Fig. 4). To every orbit, we show the four eigenstates $|E_n\rangle$ with maximal overlap $|\langle E_n | \psi(0) \rangle|$ with the initial state $|\psi(0)\rangle$ from Eq. (33) that corresponds to the initial conditions of the classical orbit. The comparison clearly reveals the correspondence between regular classical orbits and the fine structure of the phase-space distribution visible in some of the quantum eigenstates. These eigenstates occupy only part of the admissible phase space. Classical chaotic orbits, on the other hand, correspond to eigenstates that are spread out over the entire phase space.

The rightmost Husimi functions in the second and fourth row belong to the same eigenstate, which has significant overlap with the two different initial coherent states $|\psi(0)\rangle$ that correspond to the regular (b) or chaotic (d) orbit. Accordingly, the phase-space density of this state shows signatures common to classical orbits of different type. This effect resembles the “scars” of ergodic eigenstates in chaotic systems that arise from (unstable) periodic classical orbits [46–49]. Note, however, that in the present example with mixed regular and chaotic dynamics stable (quasi-)periodic orbits occupy a finite portion of the classical phase space. Therefore, a finite fraction of the eigenstates shows signatures arising from periodic orbits even in the limit $j \rightarrow \infty$, in contrast to the scars in completely chaotic systems [46,47].

For small spin length ($j = 9/2$) early indications for the localization of the oscillator (but not spin) Husimi function on stable periodic orbits have been observed in Refs. [50,51].

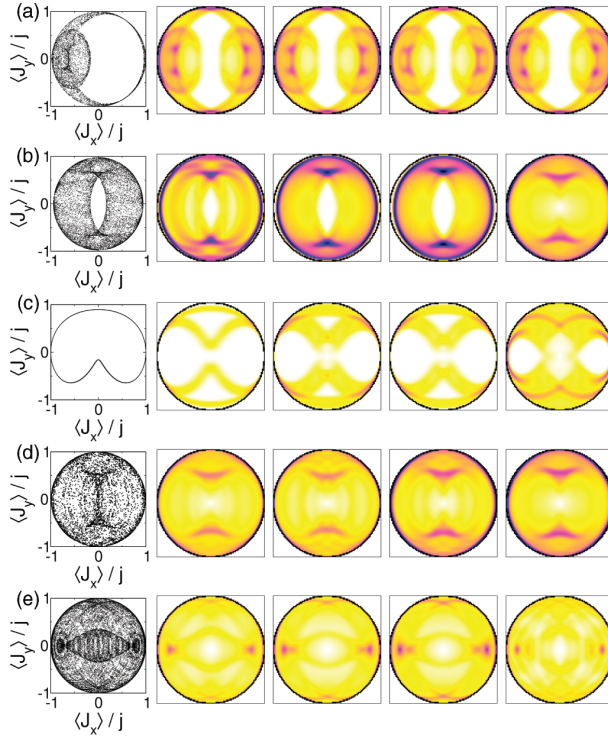


FIG. 13. (Color online) Five classical orbits at $\kappa = 0.6$ and $E = -0.5$ and eigenstates in the energy range $-0.703 < E_n < -0.249$. Shown are the respective four eigenstates (to $j = 200$) with maximal overlap with initial coherent state corresponding to the initial conditions of the respective classical orbit. Orbits (a)–(c) are regular; orbits (d)–(e) are chaotic with $\Lambda_1^{(d)} = 0.014$ and $\Lambda_1^{(e)} = 0.013$.

The clear distinction between eigenstates and phase-space signatures corresponding to regular or chaotic classical orbits requires the much larger values of j used here.

The Poincaré Husimi function is defined as

$$Q_n^{\text{Poinc}}(\theta, \phi) = |\langle \bar{\alpha}; \theta, \phi | E_n \rangle|^2, \quad (40)$$

where $\bar{\alpha}$ has the value as in the corresponding classical Poincaré surface of section, i.e., $Q = \text{Re } \bar{\alpha} = 0$ and $P = \text{Im } \bar{\alpha}$ is determined from the energy constraint $E = E(z, \bar{\alpha})$ (cf. the discussion of Fig. 4). In contrast to the spin Husimi function from Eq. (39), no trace over the bosonic degree of freedom is involved.

This function has been considered previously for other models [52,53]. In Fig. 14 we show the Poincaré Husimi function of several individual eigenstates, with energies in the vicinity of the energies of the classical Poincaré surface of section in Figs. 4. This figure reveals how the eigenstates localize at regular structures in the Poincaré plots.

V. CONCLUSIONS

Based on a combination of analytical and numerical data for the quantum dynamics of the Dicke model at large spin length we study the approach towards the classical spin limit $j \rightarrow \infty$ in two different situations.

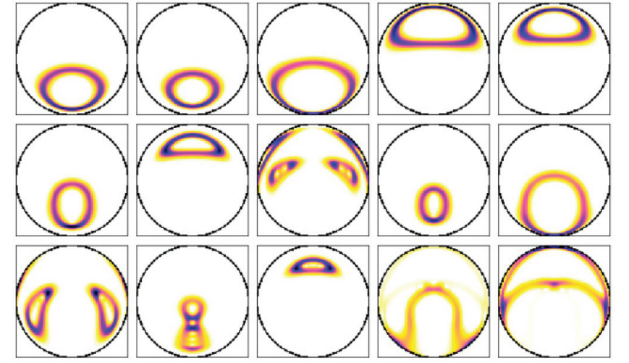


FIG. 14. (Color online) Poincaré Husimi function of the eigenstates for $j = 100$ and $\kappa = 0.1$, $-0.570 < E_n < -0.475$ (upper row) $\kappa = 0.5$, $-0.530 < E_n < -0.470$ (middle row) $\kappa = 0.6$, $-0.530 < E_n < -0.460$ (lower row) near the classical energy $E_{cl} = -0.5$ of the classical Poincaré surface of section in Fig. 4.

For the low-energy dynamics around the stationary states linearization of the semiclassical equations of motion gives two classical collective modes. The corresponding quantum observables are Green functions that describe the response of the system to a small perturbation of the ground state. The quantum-mechanical spectrum is dominated by the two classical modes already at small spin length. Convergence is rapid with growing j and allows for clear identification of the “soft mode” at the QPT already for $j \simeq 200$.

For the dynamics at higher energies, a direct comparison of quantum and classical trajectories does not show convergence towards the classical dynamics because of rapid spreading in quantum phase space. Instead, convergence is observed in the Husimi phase-space functions only. They allow us to unambiguously identify the signatures of classical (quasi-)periodic orbits and chaotic orbits in the quantum dynamics and in individual eigenstates.

In conclusion, our results give a direct picture how the classical dynamics determines the quantum dynamics at larger j . In short, the quantum dynamics is a combination of motion along a classical orbit, and spreading of the phase-space probability along, but not perpendicular to, the classical orbit. The spreading can be attributed to classical phase-space drift and quantum diffusion. This behavior is most naturally observed for classical (quasi-)periodic orbits, which lead to distinct signature in the quantum dynamics and the eigenstates. Our results thus corroborate the general scenario developed for the Dicke model in, e.g., Ref. [6]. For very long times, fragmentation of phase-space functions indicates the revival of the initial state, which poses a natural limit to the almost classical phase-space dynamics at large but finite j .

ACKNOWLEDGMENTS

We thank B. Bruhn for helpful discussions. This work was supported by Deutsche Forschungsgemeinschaft through Sonderforschungsbereich 652 (B5).

APPENDIX A: DERIVATION OF THE EQUATIONS OF MOTION FROM THE DIRAC-FRENKEL VARIATIONAL PRINCIPLE

From the derivative of the product state in Eq. (13) with respect to the parameters α , z , one obtains the three linearly independent states

$$\{|\alpha, z\rangle; a^\dagger|\alpha, z\rangle; J_+|\alpha, z\rangle\}, \quad (\text{A1})$$

which span the tangent space of the manifold of variational states. To apply the Dirac-Frenkel variational principle [30,31], we have to build an orthonormal basis in the tangent space. This is given by

$$\{|\alpha, z\rangle; |\tilde{\alpha}, z\rangle; |\alpha, \tilde{z}\rangle\}, \quad (\text{A2})$$

where

$$|\tilde{\alpha}\rangle = a^\dagger|\alpha\rangle - \alpha^*|\alpha\rangle \quad (\text{A3})$$

and

$$|\tilde{z}\rangle = \frac{1+|z|^2}{\sqrt{2j}} \left(J_+|z\rangle - \frac{2jz^*}{1+|z|^2}|z\rangle \right). \quad (\text{A4})$$

Projection of $H|\psi\rangle$ onto the basis set (A2) results in

$$\mathcal{P}H|\psi\rangle = \xi_1|\alpha, z\rangle + \xi_2|\tilde{\alpha}, z\rangle + \xi_3|\alpha, \tilde{z}\rangle, \quad (\text{A5})$$

with

$$\xi_1 = j\Delta \left(\frac{|z|^2 - 1}{|z|^2 + 1} + \frac{\kappa}{2}|\tilde{\alpha}|^2 + 2\kappa \frac{\text{Re}(\tilde{\alpha})\text{Re}(z)}{1+|z|^2} \right), \quad (\text{A6})$$

$$\xi_2 = \sqrt{\frac{j\Delta\Omega\kappa}{2}} \left(\tilde{\alpha} + \frac{2\text{Re}(z)}{1+|z|^2} \right), \quad (\text{A7})$$

and

$$\xi_3 = \sqrt{2j}\Delta \left(\frac{z}{1+|z|^2} + \frac{\kappa}{2} \frac{1-z^2}{1+|z|^2} \text{Re}(\tilde{\alpha}) \right). \quad (\text{A8})$$

On the other hand, it is

$$i \frac{d}{dt} |\psi_{\text{SC}}\rangle = \chi_1|\alpha, z\rangle + \chi_2|\tilde{\alpha}, z\rangle + \chi_3|\alpha, \tilde{z}\rangle \quad (\text{A9})$$

with

$$\begin{aligned} \chi_1 &= \frac{j\Delta\kappa}{2\Omega} (\text{Re} \dot{\tilde{\alpha}} \text{Im} \tilde{\alpha} - \text{Re} \tilde{\alpha} \text{Im} \dot{\tilde{\alpha}}) \\ &+ \frac{2j}{1+|z|^2} (\text{Re} \dot{z} \text{Im} z - \text{Re} z \text{Im} \dot{z}) \end{aligned} \quad (\text{A10})$$

and

$$\chi_2 = i \sqrt{\frac{j\Delta\kappa}{2\Omega}} \dot{\tilde{\alpha}}, \quad \chi_3 = i \frac{\sqrt{2j}}{1+|z|^2} \dot{z}. \quad (\text{A11})$$

From comparison of the coefficients ξ_1, ξ_2, ξ_3 and χ_1, χ_2, χ_3 one directly obtains the SC equations of motion for α, z [Eq. (10)].

APPENDIX B: EQUATION OF MOTION FOR THE CLASSICAL COLLECTIVE MODES

Equation (18) is a linear equation of motion, which can be written as

$$i \frac{d}{dt} \begin{pmatrix} \text{Re} \delta\tilde{\alpha} \\ i \text{Im} \delta\tilde{\alpha} \\ \text{Re} \delta z \\ i \text{Im} \delta z^* \end{pmatrix} = \mathbf{g}_{\text{lin}} \begin{pmatrix} \text{Re} \delta\tilde{\alpha} \\ i \text{Im} \delta\tilde{\alpha} \\ \text{Re} \delta z \\ i \text{Im} \delta z^* \end{pmatrix}, \quad (\text{B1})$$

with a 4×4 matrix of the form

$$\mathbf{g}_{\text{lin}} = \begin{pmatrix} 0 & g_1 & 0 & 0 \\ g_1 & 0 & g_2 & 0 \\ 0 & 0 & 0 & g_4 \\ g_3 & 0 & g_4 & 0 \end{pmatrix}, \quad (\text{B2})$$

whose parameters are read off Eq. (18) as

$$\begin{aligned} g_1 &= \Omega, & g_2 &= \Omega \frac{2(1-z_s^2)}{(1+z_s^2)^2}, \\ g_3 &= \Delta \frac{\kappa}{2}(1-z_s^2), & g_4 &= \Delta(1-\kappa\tilde{\alpha}_s z_s). \end{aligned} \quad (\text{B3})$$

For $\kappa < 1$, it is

$$g_1 = \Omega, \quad g_2 = 2\Omega, \quad g_3 = \frac{\Delta\kappa}{2}, \quad g_4 = \Delta, \quad (\text{B4})$$

and, for $\kappa > 1$,

$$g_1 = \Omega, \quad g_2 = \frac{\Omega(\kappa+1)}{\kappa^2}, \quad g_3 = \frac{\Delta\kappa}{\kappa+1}, \quad g_4 = \Delta\kappa. \quad (\text{B5})$$

Equation (B1) is the equation of motion of two coupled oscillators and can be solved as such. The eigenvalues of \mathbf{g}_{lin} are

$$\omega_{\pm}^2 = \frac{g_1^2 + g_4^2}{2} \pm \sqrt{\frac{(g_1^2 - g_4^2)^2}{4} + g_1 g_2 g_3 g_4}. \quad (\text{B6})$$

For oscillatory motion, it must be $\omega^2 > 0$, which gives the criterion

$$g_1 g_4 > g_2 g_3. \quad (\text{B7})$$

Then, four different real eigenvalues $\pm\omega_+, \pm\omega_-$ exist.

Let us now assume that $g_1 \geq g_4$, and swap g_1 and g_4 otherwise. Then, $\omega_+^2 \rightarrow g_1^2$ and $\omega_-^2 \rightarrow g_4^2$ for $g_2, g_3 \rightarrow 0$. The eigenvectors of \mathbf{g}_{lin} are

$$x_{1/2,+} = \begin{pmatrix} 1 \\ \frac{\omega}{g_1} \\ \frac{\omega^2 - g_1^2}{g_1 g_2} \\ \frac{\omega(\omega^2 - g_1^2)}{g_1 g_2 g_4} \end{pmatrix} \quad (\text{B8})$$

for the eigenvalues $\pm\omega_+$ with $\omega = \omega_+$ for x_{1+} , and $\omega = -\omega_+$ for x_{2+} , and

$$x_{1/2,-} = \begin{pmatrix} \frac{\omega^2 - g_4^2}{g_3 g_4} \\ \frac{\omega(\omega^2 - g_4^2)}{g_1 g_3 g_4} \\ 1 \\ \frac{\omega}{g_4} \end{pmatrix} \quad (\text{B9})$$

for the eigenvalues $\pm\omega_-$ with $\omega = \omega_-$ for x_{1-} , and $\omega = -\omega_-$ for x_{2-} . These expressions converge to the eigenvectors of the uncoupled oscillators for $g_2, g_3 \rightarrow 0$.

For the computation of $\delta J_x(t)$ in Eq. (21), we make the ansatz

$$\begin{pmatrix} 0 \\ 0 \\ 1 \\ 0 \end{pmatrix} = a \frac{1}{2}(x_{1-} + x_{2-}) + b \frac{\sqrt{g_1 g_2}}{\sqrt{g_3 g_4}}(x_{1+} + x_{2+}), \quad (\text{B10})$$

such that

$$a + b\xi = 1, \quad a\xi - b = 0, \quad (\text{B11})$$

with

$$\xi = \frac{\omega_+^2 - g_1^2}{\sqrt{g_1 g_2 g_3 g_4}} = -\frac{\omega_-^2 - g_4^2}{\sqrt{g_1 g_2 g_3 g_4}}. \quad (\text{B12})$$

Here we have $\xi \geq 0$. We can alternatively write

$$\begin{pmatrix} a & b \\ -b & a \end{pmatrix} \begin{pmatrix} 1 \\ \xi \end{pmatrix} = \begin{pmatrix} 1 \\ 0 \end{pmatrix}, \quad (\text{B13})$$

which is the characteristic equation for a Givens rotation. For $\xi \geq 0$, this can be solved as

$$a = \cos^2 \beta, \quad b\xi = \sin^2 \beta, \quad (\text{B14})$$

with

$$\cos 2\beta = \frac{1 - \xi^2}{1 + \xi^2} \quad (\text{B15})$$

or

$$\tan 2\beta = \pm \frac{\sqrt{1 - \cos^2 2\beta}}{\cos \beta} = \pm \frac{2|\xi|}{1 - \xi^2} = \pm \frac{2\sqrt{g_1 g_2 g_3 g_4}}{g_1^2 - g_4^2}. \quad (\text{B16})$$

Insertion of g_1, \dots, g_4 from Eqs. (B4) and (B5) gives Eqs. (24) and (25). Note that the angle β in Eq. (B16) has to be chosen from the correct branch of the arctan function. For $g_1 \geq g_4$, we take $|\beta| < \pi/2$ from the principal branch. In the opposite case $g_1 < g_4$, we use $\pi/2 < |\beta| < \pi$ (or similar) which coincides with the result after swapping g_1 and g_4 in the equations.

The third component $x_3(t)$ of the solution vector $x(t)$ of Eq. (B1), to initial condition $x(0) = \mathbf{e}_3$, then is

$$\begin{aligned} x_3(t) &= a \cos \omega_- t + b\xi \cos \omega_+ t \\ &= \cos^2 \beta \cos \omega_- t + \sin^2 \beta \cos \omega_+ t, \end{aligned} \quad (\text{B17})$$

yielding Eq. (21).

APPENDIX C: CALCULATION OF THE TIME-AVERAGED HUSIMI FUNCTION

We give here the deviation of Eq. (38). We start with the definition of the time-averaged Husimi function,

$$\bar{Q}(\theta, \phi) = \frac{1}{2T} \int_{-T}^T dt |\langle \theta, \phi | \psi(t) \rangle|^2. \quad (\text{C1})$$

The time evolved state $|\psi(t)\rangle$ is calculated by means of the Chebyshev expansion [27,38]

$$|\psi(t)\rangle = \sum_{n=0}^N c_n(t) T_n(H) |\psi(0)\rangle, \quad (\text{C2})$$

with the Chebyshev polynomials $T_n(x)$ and the expansion coefficients $c_n(t) = (-i)^n J_n(at)$, where a is a scaling factor chosen such that the spectrum of $(1/a)H$ lies in the interval $[-1, 1]$. $J_n(x)$ is the Bessel function

$$J_n(x) = \frac{1}{2\pi} \int_{-\pi}^{\pi} d\tau e^{-i(n\tau - x \sin \tau)}. \quad (\text{C3})$$

The absolute-squared overlap of $|\psi(t)\rangle$ with the coherent state $|\theta, \phi\rangle$ is given by

$$|\langle \theta, \phi | \psi(t) \rangle|^2 = \sum_{m,n=0}^N c_m^*(t) c_n(t) \mu_m^*(\theta, \phi) \mu_n(\theta, \phi), \quad (\text{C4})$$

with $\mu_n(\theta, \phi) = \langle \theta, \phi | T_n(H) | \psi(0) \rangle$. This allows us to write the time average as a matrix-vector product according to

$$\begin{aligned} \bar{Q}(\theta, \phi) &= \frac{1}{2T} \sum_{m,n=0}^N \int_{-T}^T dt c_m^*(t) c_n(t) \mu_m^*(\theta, \phi) \mu_n(\theta, \phi) \\ &= \bar{\mu}^*(\theta, \phi) \mathbf{C} \bar{\mu}(\theta, \phi), \end{aligned} \quad (\text{C5})$$

where the matrix coefficients are

$$C_{mn} = \frac{1}{2T} \int_{-T}^T dt c_m^*(t) c_n(t). \quad (\text{C6})$$

Since the integrand is given by

$$c_m^*(t) c_n(t) = \frac{i^{(m-n)}}{(2\pi)^2} \int_{-\pi}^{\pi} dx dy e^{-i(nx-my)} e^{iat(\sin x - \sin y)}, \quad (\text{C7})$$

we obtain

$$\begin{aligned} C_{mn} &= \frac{i^{(m-n)}}{2T(2\pi)^2} \int_{-\pi}^{\pi} dx dy e^{-i(nx-my)} \int_{-T}^T dt e^{iat(\sin x - \sin y)} \\ &= \frac{i^{(m-n)}}{(2\pi)^2} \int_{-\pi}^{\pi} dx dy e^{-i(nx-ny)} \text{sinc}[aT(\sin x - \sin y)]. \end{aligned} \quad (\text{C8})$$

The remaining integral can be evaluated numerically, e.g., by means of a discrete Fourier transformation in the form

$$\begin{aligned} C_{mn} &= \frac{i^{(m-n)} (-1)^{(m+n)}}{N^2} \\ &\times \sum_{\nu=0}^{N-1} \sum_{\mu=0}^{N-1} \text{sinc}[aT(\sin x_\nu + \sin y_\nu)] e^{-inx_\nu} e^{-imy_\mu}, \end{aligned} \quad (\text{C9})$$

with $x_\nu = \frac{2\pi\nu}{N}$, $y_\nu = \frac{2\pi\mu}{N}$, and $\nu, \mu = 0, 1, \dots, N-1$.

- [1] L. G. Yaffe, *Rev. Mod. Phys.* **54**, 407 (1982).
- [2] L. Diósi, N. Gisin, and W. T. Strunz, *Phys. Rev. A* **61**, 022108 (2000).
- [3] M. C. Gutzwiller, *Chaos in Classical and Quantum Mechanics* (Springer, New York, 1990).
- [4] F. Haake, *Quantum Signatures of Chaos*, 3rd ed. (Springer, Berlin, 2010).
- [5] M. Srednicki, *Phys. Rev. E* **50**, 888 (1994).
- [6] A. Altland and F. Haake, *Phys. Rev. Lett.* **108**, 073601 (2012).
- [7] A. Altland and F. Haake, *New J. Phys.* **14**, 073011 (2012).
- [8] R. H. Dicke, *Phys. Rev.* **93**, 99 (1954).
- [9] K. Hepp and E. H. Lieb, *Ann. Phys. (N.Y.)* **76**, 360 (1973).
- [10] Y. K. Wang and F. T. Hioe, *Phys. Rev. A* **7**, 831 (1973).
- [11] N. Lambert, C. Emary, and T. Brandes, *Phys. Rev. Lett.* **92**, 073602 (2004).
- [12] N. Lambert, C. Emary, and T. Brandes, *Phys. Rev. A* **71**, 053804 (2005).
- [13] J. Vidal and S. Dusuel, *Europhys. Lett.* **74**, 817 (2006).
- [14] L. Bakemeier, A. Alvermann, and H. Fehske, *Phys. Rev. A* **85**, 043821 (2012).
- [15] M. Kuś, *Phys. Rev. Lett.* **54**, 1343 (1985).
- [16] R. Graham and M. Höhnnerbach, *Phys. Rev. Lett.* **57**, 1378 (1986).
- [17] C. Lewenkopf, M. Nemes, V. Marvulle, M. Pato, and W. Wreszinski, *Phys. Lett. A* **155**, 113 (1991).
- [18] C. Emary and T. Brandes, *Phys. Rev. E* **67**, 066203 (2003).
- [19] M. A. M. de Aguiar, K. Furuya, C. H. Lewenkopf, and M. C. Nemes, *Ann. Phys. (N.Y.)* **216**, 291 (1992).
- [20] K. Furuya, M. C. Nemes, and G. Q. Pellegrino, *Phys. Rev. Lett.* **80**, 5524 (1998).
- [21] L. Song, J. Ma, D. Yan, and X. Wang, *Eur. Phys. J. D* **66**, 1 (2012).
- [22] L. Song, D. Yan, J. Ma, and X. Wang, *Phys. Rev. E* **79**, 046220 (2009).
- [23] G. Rempe, H. Walther, and N. Klein, *Phys. Rev. Lett.* **58**, 353 (1987).
- [24] M. Brune, F. Schmidt-Kaler, A. Maali, J. Dreyer, E. Hagley, J. M. Raimond, and S. Haroche, *Phys. Rev. Lett.* **76**, 1800 (1996).
- [25] A. Alvermann, L. Bakemeier, and H. Fehske, *Phys. Rev. A* **85**, 043803 (2012).
- [26] A. Weiße, G. Wellein, A. Alvermann, and H. Fehske, *Rev. Mod. Phys.* **78**, 275 (2006).
- [27] H. Tal-Ezer and R. Kosloff, *J. Chem. Phys.* **81**, 3967 (1984).
- [28] R. Graham and M. Höhnnerbach, *Z. Phys. B* **57**, 233 (1984).
- [29] W.-M. Zhang, D. H. Feng, and R. Gilmore, *Rev. Mod. Phys.* **62**, 867 (1990).
- [30] P. A. M. Dirac, *Proc. Cambridge Philos. Soc.* **26**, 373 (1930).
- [31] J. Frenkel, *Wave Mechanics, Advanced General Theory* (Clarendon Press, Oxford, 1934).
- [32] M. A. M. de Aguiar, K. Furuya, and M. C. Nemes, *Quantum Opt.* **3**, 305 (1991).
- [33] L. S. Schulman, *Phys. Rev. A* **68**, 052109 (2003).
- [34] R. Sonone and S. Jain, *Eur. Phys. J.: Spec. Top.* **222**, 601 (2013).
- [35] R. Schubert, R. O. Vallejos, and F. Toscano, *J. Phys. A* **45**, 215307 (2012).
- [36] G. Benettin, L. Galgani, A. Giorgilli, and J.-M. Strelcyn, *Meccanica* **15**, 9 (1980).
- [37] G. Benettin, L. Galgani, A. Giorgilli, and J.-M. Strelcyn, *Meccanica* **15**, 21 (1980).
- [38] A. Alvermann and H. Fehske, *Phys. Rev. B* **77**, 045125 (2008).
- [39] W. P. Schleich, *Quantum Optics in Phase Space* (Wiley-VCH, New York, 2001).
- [40] V. V. Sokolov, O. V. Zhirov, G. Benenti, and G. Casati, *Phys. Rev. E* **78**, 046212 (2008).
- [41] V. Balachandran, G. Benenti, G. Casati, and J. Gong, *Phys. Rev. E* **82**, 046216 (2010).
- [42] V. Bužek, H. Moya-Cessa, P. L. Knight, and S. J. D. Phoenix, *Phys. Rev. A* **45**, 8190 (1992).
- [43] L. Chotorlishvili and A. Ugulava, *Physica D* **239**, 103 (2010).
- [44] U. Weiss, *Quantum Dissipative Systems* (World Scientific, Singapore, 1999).
- [45] D. Pagel, A. Alvermann, and H. Fehske, *Phys. Rev. E* **87**, 012127 (2013).
- [46] E. J. Heller, *Phys. Rev. Lett.* **53**, 1515 (1984).
- [47] L. Kaplan and E. Heller, *Ann. Phys. (N.Y.)* **264**, 171 (1998).
- [48] R. L. Waterland, J.-M. Yuan, C. C. Martens, R. E. Gillilan, and W. P. Reinhardt, *Phys. Rev. Lett.* **61**, 2733 (1988).
- [49] D. Biswas and S. R. Jain, *Phys. Rev. A* **42**, 3170 (1990).
- [50] M. A. M. de Aguiar, K. Furuya, C. H. Lewenkopf, and M. C. Nemes, *Europhys. Lett.* **15**, 125 (1991).
- [51] K. Furuya, M. de Aguiar, C. Lewenkopf, and M. Nemes, *Ann. Phys. (N.Y.)* **216**, 313 (1992).
- [52] P. Leboeuf and M. Saraceno, *J. Phys. A* **23**, 1745 (1990).
- [53] G. Groh, H. J. Korsch, and W. Schweizer, *J. Phys. A* **31**, 6897 (1998).

Route to chaos in optomechanics

L. Bakemeier,^{*} A. Alvermann,[†] and H. Fehske[‡]
Institut für Physik, Ernst-Moritz-Arndt-Universität, 17487 Greifswald, Germany

We establish the emergence of chaotic motion in optomechanical systems. Chaos appears at negative detuning for experimentally accessible values of the pump power and other system parameters. We describe the sequence of period doubling bifurcations that leads to chaos, and state the experimentally observable signatures in the optical spectrum. In addition to the semi-classical dynamics we analyze the possibility of chaotic motion in the quantum regime. We find that quantum mechanics protects the optomechanical system against irregular dynamics, such that simple periodic orbits reappear and replace the classically chaotic motion. In this way observation of the dynamical signatures makes it possible to pin down the crossover from quantum to classical mechanics.

PACS numbers: 42.50.Ct, 37.10.Vz, 05.45.-a, 07.10.Cm

The coupling between light and matter lies at the heart of modern physics. In recent years the fabrication of optomechanical systems using, e.g., microtoroid resonators [1–3], suspended micromirrors [4, 5], whispering gallery microdisks [6, 7] or microsphere resonators [8–10] has opened up new possibilities for fundamental research and technological applications [11–14]. Because the light-matter coupling and other system parameters can be adjusted over large scales optomechanics provides a genuine opportunity to access the classical and quantum dynamics of mesoscopic driven dissipative systems in a variety of different regimes. Optomechanical systems have been used—or proposed to be used—for the creation of non-classical light [15], preparation of Schrödinger cat states [16], generation of light-matter entanglement [17], ultra-precision measurements [18, 19], and radiative cooling to the ground state [20, 21].

The basic optomechanical system consists of a cantilever in a cavity. The cantilever motion is affected by the radiation pressure of the cavity field, and thus implements light-matter coupling at a truly fundamental level. The cavity is pumped with an external laser, which drives the system out of equilibrium. Experiments have successfully demonstrated the optical bistability of the cavity-cantilever dynamics that leads to self-induced cantilever oscillations [2, 22, 23]. With a few exceptions [1, 24], previous studies mainly addressed the regime of simple periodic cantilever motion, and took the prevalence of regular over irregular dynamics for granted.

In this Letter, we consider the dynamics of the optomechanical system with a view towards chaotic motion. We demonstrate the appearance of chaos at negative detuning and explain how to detect it experimentally through characteristic signatures in the optical spectrum. Chaos emerges already for slightly increased pump power which makes it accessible with present experimental setups. We identify the period doubling bifurcations on the way to chaos, and provide the bifurcation diagrams for the first chaotic orbits.

Chaotic dynamics of the optomechanical system appears in the bad-cavity limit and is described by the semi-

classical equations of motion. In the quantum regime we use a Monte Carlo propagation technique [25, 26] to solve the master equation for the density matrix, which allows us to track the deviations from the classical dynamics systematically. Surprisingly, chaotic motion can be suppressed in favor of regular oscillatory motion of the cantilever by pushing the system into the quantum regime. We can relate the reemergence of periodic cantilever oscillations to the localization of individual quantum trajectories on simple limit cycles that are not accessible in the classical dynamics.

Our theoretical analysis is based on the generic Hamilton operator of optomechanics [13, 14, 27]

$$\frac{1}{\hbar} H = [-\Delta + g_0(b + b^\dagger)] a^\dagger a + \Omega b^\dagger b + \alpha_L (a^\dagger + a). \quad (1)$$

It describes, e.g., the vibrational mode of a cantilever ($b^{(\dagger)}$, with frequency Ω) under the influence of the radiation pressure ($\propto g_0$) of the cavity photon field ($a^{(\dagger)}$). To include the effect of the pump laser, with amplitude α_L and detuning $\Delta = \omega_{\text{las}} - \omega_{\text{cav}}$ of the laser and cavity frequency, the Hamilton operator is written in a reference frame rotating at the laser frequency. To account for radiative cavity losses ($\propto \kappa$) and cantilever damping ($\propto \Gamma$) we have to study the time evolution of the density matrix $\rho(t)$ with the quantum-optical master equation

$$\frac{d\rho}{dt} = -\frac{i}{\hbar} [H, \rho] + \Gamma \mathcal{D}[b, \rho] + \kappa \mathcal{D}[a, \rho]. \quad (2)$$

Note that we work here and in the following at zero temperature, such that the dissipative Lindblad terms

$$\mathcal{D}[L, \rho] = L\rho L^\dagger - \frac{1}{2}(L^\dagger L\rho + \rho L^\dagger L) \quad (3)$$

contain only bosonic annihilation operators $L \in \{a, b\}$.

We now express the system parameters in units of Ω , measure time as $\tau = \Omega t$, and introduce the two dimensionless parameters [28, 29]

$$P = \frac{8\alpha_L^2 g_0^2}{\Omega^4}, \quad \sigma = \frac{g_0}{\kappa}. \quad (4)$$

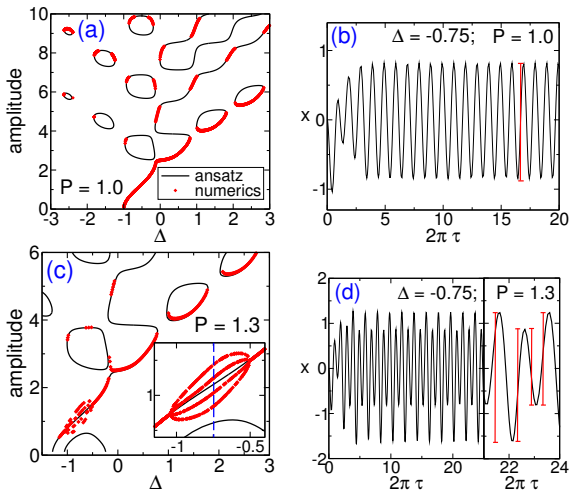


FIG. 1. (Color online) (a) and (c): Amplitudes of cantilever oscillation limit cycles given by the sinusoidal ansatz (black line) and from the numerical solution of the SC equations of motions (6) (red diamonds). (b) and (d): Initial dynamics of the cantilever converging to a period-1 resp. period-2 limit cycle. Here, as in all figures, we give Δ, τ in units of $\Omega^{(-1)}$ and use the dimensionless parameters P, σ from Eq. (4).

The pump parameter P gives the strength of the laser pumping of the cavity. The quantum-classical scaling parameter $\sigma = x_{\text{zpt}}/x_{\text{res}} = g_0/\kappa$ relates the zero-point fluctuations $x_{\text{zpt}} = \sqrt{\hbar/(2m\Omega)}$ of the cantilever (with mass m) to the resonance width x_{res} of the cavity [29]. Note that x_{res} is a classical quantity, characterizing the cavity quality, while x_{zpt} is of order $\hbar^{1/2}$ such that σ vanishes for $\hbar \rightarrow 0$. Variation of σ thus allows us to track how the quantum dynamics of the optomechanical system evolves towards the classical dynamics in the bad-cavity limit $x_{\text{zpt}} \ll x_{\text{res}}$, i.e., $\sigma \ll 1$.

For the numerical results we fix the damping parameters $\kappa/\Omega = 1$, $\Gamma/\Omega = 10^{-3}$, which are typical values realized in experiments [14]. This leaves us with the three parameters Δ, P, σ .

We first establish the emergence of chaotic motion in the bad-cavity limit $\sigma \ll 1$. In this limit, the dynamics of the optomechanical systems follows the semi-classical (SC) equations of motion [29]

$$\frac{d\alpha}{d\tau} = i \left[\frac{\Delta}{\Omega} \alpha - (\beta + \beta^*) \alpha - \frac{1}{2} \right] - \frac{\kappa}{2\Omega} \alpha, \quad (5)$$

$$\frac{d\beta}{d\tau} = -i \left[\frac{P}{2} |\alpha|^2 + \beta \right] - \frac{\Gamma}{2\Omega} \beta \quad (6)$$

for the rescaled cavity and cantilever amplitude $\alpha = (\Omega/(2\alpha_L)) \langle a \rangle$, $\beta = (g/\Omega) \langle b \rangle$. For the cantilever we also use the phase space variables $x = 1/\sqrt{2}(\beta + \beta^*)$ and $p = -i/\sqrt{2}(\beta^* - \beta)$.

The SC equations of motion are obtained from the Ehrenfest equations of motion for the photon ($a^{(\dagger)}$) and

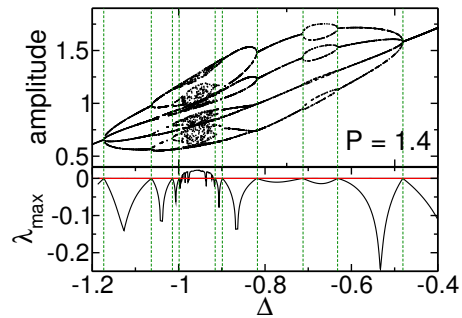


FIG. 2. (Color online) Bifurcation diagram of the limit cycle amplitude (above) and corresponding maximal Lyapunov exponent λ_{max} (below) at $P = 1.4$. Vertical dashed lines mark PDBs, signaled by $\lambda_{\text{max}} = 0$.

phonon ($b^{(\dagger)}$) mode, together with the SC approximation $\langle (b^\dagger + b) a \rangle \approx \langle b^\dagger + b \rangle \langle a \rangle$ in which all photon-phonon correlations are neglected. For $\sigma > 0$ the SC equations are an approximation to the full quantum dynamics in Eq. (2), but become exact in the limit $\sigma \rightarrow 0$.

The SC equations of motion predict the optical bistability of the optomechanical system, where self-induced cantilever oscillations arise through a Hopf bifurcation [28, 29]. The stable attractors of self-induced oscillations are shown in Fig. 1 (a). The oscillations can be described with a simple sinusoidal ansatz $x(t) = \bar{x} + A \cos(\Omega t)$ for the cantilever position. Inserting the ansatz into the SC equations of motion (6) allows for an analytical solution in terms of a Fourier series [28, 29]. The predictions of the ansatz agree well with the amplitudes extracted from the numerical solution of the SC equations (see Fig. 1 (b) for a sample trajectory).

We now follow the route from regular self-induced cantilever oscillations into the chaotic regime by increasing the pump power P . For $P = 1.3$ a period doubling bifurcation (PDB) has taken place, and a new limit cycle with twice the period of the original simple periodic cycle appears for negative detuning and small amplitude, as shown in Fig. 1 (c). A sample trajectory located on the period-2 limit cycle is shown in Fig. 1 (d). The single-frequency ansatz fails trivially predicting the PDB, the four possible “amplitudes” of the period-2 cycle are extracted from the numerical solution of the SC equations.

Increasing the driving further leads to additional PDBs and the appearance of period- n limit cycles (not shown here). Eventually, for $P = 1.4$, chaotic motion emerges as shown in Fig. 2. We distinguish chaotic and regular trajectories through the maximal Lyapunov exponent (LE), which we calculate with the “standard” method from [30, 31]. The LE vanishes at every PDB, and separates regular motion with a negative LE from chaotic motion with a positive LE. As the LE in Fig. 2 shows, the chaotic region is bounded and contained within a small window $\Delta \in [-1.0, -0.91]$.

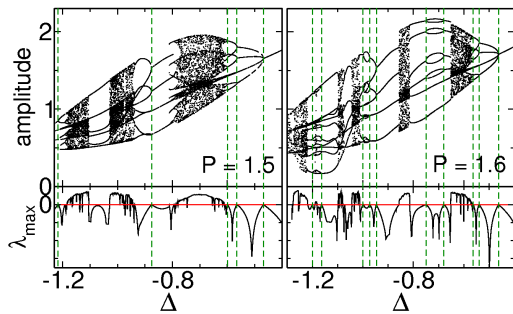


FIG. 3. (Color online) Bifurcation diagrams of the limit cycle amplitude and maximal Lyapunov exponents λ_{\max} for larger pump power $P = 1.5, 1.6$.

The bifurcation diagrams get more and more complex with increasing P , as shown in Fig. 3. The chaotic regions do not only expand and fill larger intervals of the detuning, but they also split and form a fairly complex intertwined sequence of regular and chaotic dynamics. Notably, the appearance of regular or chaotic motion is very susceptible to the value of Δ . Changing the laser-cavity detuning one can easily tune the optomechanical system in and out of chaos.

The appearance of chaos is summarized in Fig. 4. If we follow the route to chaos by increasing the pump power P , the first PDBs occur in a parabolic region for $P \gtrsim 1.15$ before chaotic motion sets in for slightly larger $P \gtrsim 1.4$. The chaotic regime does not form a simple convex part of the parameter plane, but has a complex structure characterized by interjacent regions of regular motion. Importantly, PDBs and chaos appear at parameter values $-1.5 \leq \Delta$, $P \leq 1.6$ accessible to experiments.

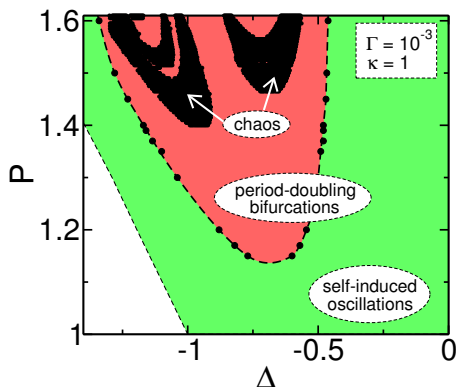


FIG. 4. (Color online) Schematic picture of the regular and chaotic regimes of the optomechanical system in the bad-cavity limit $\sigma \ll 1$, plotted in the Δ - P plane. Here, as everywhere, $\kappa = 1$ and $\Gamma = 10^{-3}$. Dots represent numerical data extracted from bifurcation diagrams (such as Figs. 2, 3), dashed lines interpolate between the numerical data.

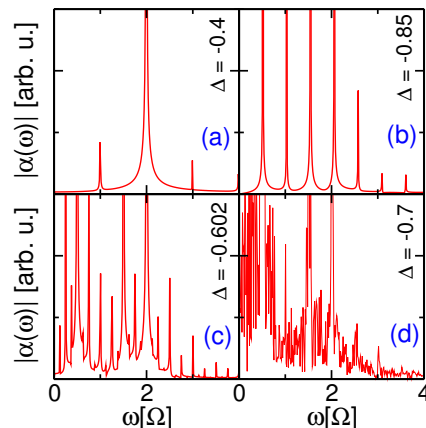


FIG. 5. (Color online) Fourier spectrum of the classical photon field amplitude α for $P = 1.5$. The figures show spectra corresponding to cantilever dynamics on a simple periodic limit cycle (a), a period-2 limit cycle (b), a period-4 limit cycle (c), and a chaotic limit cycle (d).

Experimental evidence for chaotic motion can be obtained from the cavity intensity spectrum, as shown in Fig. 5. For period-1 oscillations, with $\Delta = -0.4$ to the right of the chaotic window in Fig. 2, peaks in the spectrum occur only at multiples of the cantilever frequency Ω (panel a). Moving further into the negative detuning regime ($\Delta < -0.4$), additional peaks occur between the peaks of the preceding spectrum with each PDB, at multiples of $\Omega/2$ ($\Omega/4$) after the first (second) PDB in panel (b) (panel (c)), until the chaotic regime is reached and the spectrum becomes continuous (Fig. 5 (d)).

Note that we focus on negative detuning $\Delta < 0$, where chaos appears already at moderate pump power P . Chaotic motion exists also for positive detuning $\Delta > 0$, but then requires much larger P such that it will be harder to access experimentally.

We now turn to the quantum dynamics of the optomechanical system. The non-linear SC dynamics emerges from the quantum dynamics only in the bad-cavity limit $\sigma \ll 1$. In this regime the photon and phonon mode are occupied up to high boson numbers ($\langle a \rangle, \langle b \rangle \sim 10^3$), which renders the direct solution of the master equation (2) impossible. Instead we use the Monte Carlo method of quantum state diffusion (QSD) [25, 26] in the implementation of Schack and Brun [32]. In QSD the density matrix $\rho(t)$ is represented as a classical mixture of individual quantum trajectories. The time evolution of the trajectories is governed by a stochastic differential equation that replaces the master equation (2). One advantage of QSD over other unraveling techniques, e.g., the quantum jump method [33], is the dynamical localization of the quantum trajectories on classical orbits [34–36]. This property gives direct access to the emergence of SC dynamics in the bad-cavity limit through comparison of

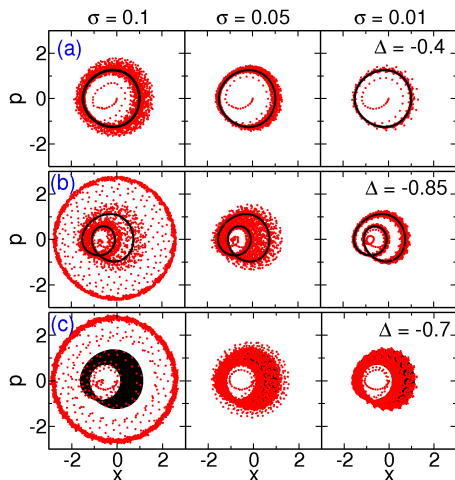


FIG. 6. (Color online) Stroboscopic (x, p) -phase space plot of a single quantum trajectory (red points) for decreasing quantum-classical scaling parameter σ , approaching a simple periodic limit cycle (a), a period-2 limit cycle (b) and a chaotic limit cycle (c) (black curves) in the limit $\sigma \rightarrow 0$.

individual quantum and classical trajectories.

Typical quantum trajectories for different values of the scaling parameter σ and different classical attractors are shown as a stroboscopic plot in Fig. 6. We observe how with decreasing σ the trajectories localize on the classical limit cycles. For more complex classical orbits, localization requires smaller values of σ . The localization properties change completely in the quantum regime ($\sigma = 0.1$, panels (b), (c)). Now the quantum trajectory localizes on a simple periodic orbit, which differs from the classical limit cycle and is not accessible in the SC dynamics.

The localization of individual quantum trajectories provides a qualitative idea of the quantum dynamics of the optomechanical system, but can not be measured or quantified. Experimentally accessible quantities are obtained from the ensemble average over all trajectories. Fig. 7 shows the resulting cantilever position $x(t)$ in comparison to the SC trajectories after the initial transient dynamics has faded out. As the optomechanical systems evolves out of the SC limit one observes that the classical (period-2 or chaotic) motion is replaced by simple periodic cantilever oscillations in the quantum regime. As could be anticipated by the different localization properties of the individual quantum trajectories the quantum dynamics favors simple periodic motion, which does not need to have a classical counterpart. As witnessed by the two curves for $\sigma = 0.01$ in Fig. 7 the position of the crossover from classical to period-1 motion depends on the complexity of the classical limit cycle. For more complex or chaotic orbits it takes place closer to the SC limit, such that the $\sigma = 0.01$ curve still agrees with the classical dynamics for a period-2 orbit (left panels), but al-

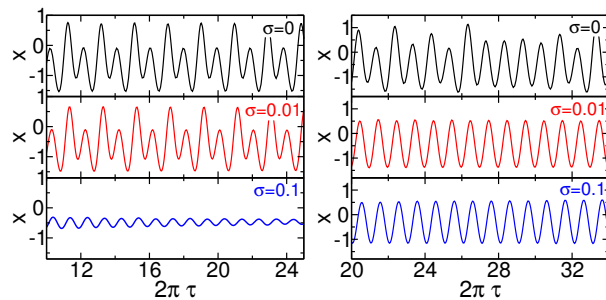


FIG. 7. (Color online) Quantum dynamics of the cantilever from the ensemble average of 5000 quantum trajectories ($\sigma > 0$) in comparison to the SC dynamics ($\sigma = 0$), all for $P = 1.5$. The figures depict the case of a classical period-2 orbit ($\Delta = -0.85$, left) and a chaotic orbit ($\Delta = -0.7$, right).

ready shows the simple periodic oscillations of the quantum regime for a classically chaotic orbit (right panels).

To conclude, we here analyze the route to chaos in the optomechanical system and track the appearance of PDBs in the cantilever oscillations as the first step to mixed regular-chaotic dynamics. From comparison of the SC dynamics with the quantum dynamics we find that the quantum dynamics is strongly protected against chaotic motion. The central result is that in the optomechanical system quantum mechanics counteracts the classical route to chaos and stabilizes simple periodic orbits. This behavior can be traced back to the different localization properties of individual quantum trajectories.

Besides being of interest in itself, the existence of chaos in the optomechanical system could be relevant for ultra-precision measurements or fundamental tests on the physical conditions for classical dynamics. Because the mixed regular-chaotic dynamics we depicted is susceptible to small variations of the systems parameters, e.g., the cantilever mass or the laser-cavity detuning, such variations can be detected through drastic changes in the cantilever dynamics. On the other, the fact that the quantum dynamics favors simple periodic over multi-periodic or irregular chaotic motion may help to explain why optomechanical systems can be used in a controlled way even deep in the quantum regime.

First experimental results on the observation of PDBs and chaotic motion in the intensity spectrum of an optomechanical system were reported in [1, 24]. In light of our results we suggest to continue experimental studies in this direction, systematically tracing out the boundaries of the regular and chaotic regimes in comparison to the theoretical predictions garnered from the SC equations of motion. In particular, one should try to locate the crossover from classically multi-periodic or chaotic motion to the simple periodic quantum dynamics by changing the quantum-classical scaling parameter σ , e.g., through variation of the cantilever mass.

Acknowledgments. The authors wish to thank B. Bruhn and F. Marquardt for helpful discussion. This work was supported by Deutsche Forschungsgemeinschaft via SFB 652 (B5).

* bakemeier@physik.uni-greifswald.de

† alvermann@physik.uni-greifswald.de

‡ fehske@physik.uni-greifswald.de

- [1] T. Carmon, H. Rokhsari, L. Yang, T. J. Kippenberg, and K. J. Vahala, *Phys. Rev. Lett.* **94**, 223902 (2005).
- [2] T. J. Kippenberg, H. Rokhsari, T. Carmon, A. Scherer, and K. J. Vahala, *Phys. Rev. Lett.* **95**, 033901 (2005).
- [3] H. Rokhsari, T. H. Kippenberg, T. Carmon, and K. J. Vahala, *Opt. Express* **13**, 5293 (2005).
- [4] O. Arcizet, P.-F. Cohadon, T. Briant, T. Pinard, and A. Heidmann, *Nature* **444**, 71 (2006).
- [5] S. Gigan, H. R. Böhm, M. Paternostro, F. Blaser, G. Langer, J. B. Hertzberg, K. C. Schwab, D. Bäuerle, M. Aspelmeyer, and A. Zeilinger, *Nature* **444**, 67 (2006).
- [6] X. Jiang, Q. Lin, J. Rosenberg, K. Vahala, and O. Painter, *Optics Express* **17**, 20911 (2006).
- [7] G. S. Wiederhecker, L. Chen, A. Gondarenko, and M. Lipson, *Nature* **462**, 633 (2009).
- [8] R. Ma, A. Schliesser, P. Del’Haye, A. Dabirian, G. Anetsberger, and T. Kippenberg, *Opt. Lett.* **32**, 2200 (2007).
- [9] Y.-S. Park and H. Wang, *Nature Phys.* **5**, 489 (2009).
- [10] M. Tomes and T. Carmon, *Phys. Rev. Lett.* **102**, 113601 (2009).
- [11] T. J. Kippenberg and K. J. Vahala, *Science* **321**, 1172 (2008).
- [12] F. Marquardt and S. M. Girvin, *Physics* **2**, 40 (2009).
- [13] P. Meystre, *Ann. Phys. (Berlin)* **525**, 215 (2013).
- [14] M. Aspelmeyer, T. J. Kippenberg, and F. Marquardt, “Cavity Optomechanics,” (2013), arXiv:1303.0733.
- [15] D. W. C. Brooks, T. Botter, S. Schreppler, T. P. Purdy, N. Brahms, and D. M. Stamper-Kurn, *Nature* **488**, 476 (2012).
- [16] X.-Y. Lü, W.-M. Zhang, S. Ashhab, Y. Wu, and F. Nori, *Sci. Rep.* **3**, 2943 (2013).
- [17] R. Ghobadi, S. Kumar, B. Pepper, D. Bouwmeester, A. I. Lvovsky, and C. Simon, *Phys. Rev. Lett.* **112**, 080503 (2014).
- [18] J.-Q. Zhang, Y. Li, M. Feng, and Y. Xu, *Phys. Rev. A* **86**, 053806 (2012).
- [19] F. Liu, S. Alaie, Z. C. Leseman, and M. Hossein-Zadeh, *Optics Express* **21**, 19555 (2013).
- [20] J. D. Teufel, T. Donner, D. Li, J. W. Harlow, M. S. Allman, K. Cicak, A. J. Sirois, J. D. Whittaker, K. W. Lehnert, and R. W. Simmonds, *Nature* **475**, 359 (2011).
- [21] J. Chan, T. P. M. Alegre, A. H. Safavi-Naeini, J. T. Hill, A. Krause, S. Groblacher, M. Aspelmeyer, and O. Painter, *Nature* **478**, 89 (2011).
- [22] C. Metzger, M. Ludwig, C. Neuenhahn, A. Ortlieb, I. Favero, K. Karrai, and F. Marquardt, *Phys. Rev. Lett.* **101**, 133903 (2008).
- [23] S. Zaitsev, A. K. Pandey, O. Shtempluck, and E. Buks, *Phys. Rev. E* **84**, 046605 (2011).
- [24] T. Carmon, M. C. Cross, and K. J. Vahala, *Phys. Rev. Lett.* **98**, 167203 (2007).
- [25] N. Gisin and I. C. Percival, *J. Phys. A: Math. Gen.* **25**, 5677 (1992).
- [26] L. Diosi, *Phys. Lett. A* **129**, 419 (1988).
- [27] C. K. Law, *Phys. Rev. A* **51**, 2537 (1995).
- [28] F. Marquardt, J. G. E. Harris, and S. M. Girvin, *Phys. Rev. Lett.* **96**, 103901 (2006).
- [29] M. Ludwig, B. Kubala, and F. Marquardt, *New J. Phys.* **10**, 095013 (2008).
- [30] G. Benettin, L. Galgani, A. Giorgilli, and J.-M. Strelcyn, *Meccanica* **15**, 9 (1980).
- [31] G. Benettin, L. Galgani, A. Giorgilli, and J.-M. Strelcyn, *Meccanica* **15**, 21 (1980).
- [32] R. Schack and T. A. Brun, *Comp. Phys. Comm.* **102**, 210 (1997).
- [33] K. Mølmer, Y. Castin, and J. Dalibard, *J. Opt. Soc. Am. B* **10**, 524 (1993).
- [34] M. Rigo and N. Gisin, *Quantum Semiclass. Opt.* **8**, 255 (1996).
- [35] R. Schack, T. A. Brun, and I. C. Percival, *J. Phys. A: Math. Gen.* **28**, 5401 (1995).
- [36] W. T. Strunz and I. C. Percival, *J. Phys. A: Math. Gen.* **31**, 1801 (1998).

Bibliography

- [Agarwal97] G. S. Agarwal, R. R. Puri, and R. P. Singh. *Phys. Rev. A* **56**, 2249 (1997).
- [Altland12a] A. Altland and F. Haake. *New Journal of Physics* **14**, 073011 (2012).
- [Altland12b] A. Altland and F. Haake. *Phys. Rev. Lett.* **108**, 073601 (2012).
- [Aspelmeyer13] M. Aspelmeyer, T. J. Kippenberg, and F. Marquardt. *Cavity Optomechanics* (2013).
- [Benettin80a] G. Benettin, L. Galgani, A. Giorgilli, and J.-M. Strelcyn. *Meccanica* **15**, 9 (1980).
- [Benettin80b] G. Benettin, L. Galgani, A. Giorgilli, and J.-M. Strelcyn. *Meccanica* **15**, 21 (1980).
- [Bourassa09] J. Bourassa, J. M. Gambetta, A. A. Abdumalikov, O. Astafiev, Y. Nakamura, and A. Blais. *Phys. Rev. A* **80**, 032109 (2009).
- [Braunstein05] S. L. Braunstein and P. van Loock. *Rev. Mod. Phys.* **77**, 513 (2005).
- [Brun96] T. A. Brun, I. C. Percival, and R. Schack. *Journal of Physics A: Mathematical and General* **29**, 2077 (1996).
- [Brune90] M. Brune, S. Haroche, V. Lefevre, J. M. Raimond, and N. Zagury. *Phys. Rev. Lett.* **65**, 976 (1990).
- [Brune92] M. Brune, S. Haroche, J. M. Raimond, L. Davidovich, and N. Zagury. *Phys. Rev. A* **45**, 5193 (1992).
- [Brune96] M. Brune, F. Schmidt-Kaler, A. Maali, J. Dreyer, E. Hagley, J. M. Raimond, and S. Haroche. *Phys. Rev. Lett.* **76**, 1800 (1996).
- [Dicke53] R. H. Dicke. *Phys. Rev.* **93**, 99 (1953).
- [Diosi88] L. Diosi. *Physics Letters A* **129**, 419 (1988).
- [Dirac30] P. A. M. Dirac. *Proc. Cambridge Philos. Soc.* **26**, 373 (1930).
- [Eberly80] J. H. Eberly, N. B. Narozhny, and J. J. Sanchez-Mondragon. *Phys. Rev. Lett.* **44**, 1323 (1980).
- [Emary03a] C. Emary and T. Brandes. *Phys. Rev. E* **67**, 066203 (2003).

- [Emary03b] C. Emary and T. Brandes. *Phys. Rev. Lett.* **90**, 044101 (2003).
- [Fink09] J. M. Fink, R. Bianchetti, M. Baur, M. Göppl, L. Steffen, S. Filipp, P. J. Leek, A. Blais, and A. Wallraff. *Phys. Rev. Lett.* **103**, 083601 (2009).
- [Frenkel34] J. Frenkel. *Wave Mechanics, Advanced General Theory*. Clarendon Press (Oxford), 1934.
- [Gea-Banacloche90] J. Gea-Banacloche. *Phys. Rev. Lett.* **65**, 3385 (1990).
- [Gisin92] N. Gisin and I. C. Percival. *J. Phys. A: Math. Gen.* **25**, 5677 (1992).
- [Graham84] R. Graham and M. Höhnerbach. *Z. Phys. B* **57**, 233 (1984).
- [Haroche97] S. Haroche, M. Brune, and J. M. Raimond. *Philosophical Transactions of the Royal Society of London. Series A: Mathematical, Physical and Engineering Sciences* **355**, 2367 (1997).
- [Heinrich11] G. Heinrich, M. Ludwig, J. Qian, B. Kubala, and F. Marquardt. *Phys. Rev. Lett.* **107**, 043603 (2011).
- [Hepp73] K. Hepp and E. H. Lieb. *Annals of Physics* **76**, 360 (1973).
- [Holstein40] T. Holstein and H. Primakoff. *Phys. Rev.* **58**, 1098 (1940).
- [Horodecki09] R. Horodecki, P. Horodecki, M. Horodecki, and K. Horodecki. *Rev. Mod. Phys.* **81**, 865 (2009).
- [Jaynes63] E. Jaynes and F. W. Cummings. *Proceedings of the IEEE* **51**, 89 (1963).
- [Kippenberg08] T. J. Kippenberg and K. J. Vahala. *Science* **321**, 1172 (2008).
- [Klimov98] A. Klimov and C. Saavedra. *Physics Letters A* **247**, 14 (1998).
- [Kryuchkyan02] G. Y. Kryuchkyan and S. B. Manvelyan. *Phys. Rev. Lett.* **88**, 094101 (2002).
- [Lambert04] N. Lambert, C. Emary, and T. Brandes. *Phys. Rev. Lett.* **92**, 073602 (2004).
- [Lambert05] N. Lambert, C. Emary, and T. Brandes. *Phys. Rev. A* **71**, 053804 (2005).
- [Larson10] J. Larson. *EPL (Europhysics Letters)* **90**, 54001 (2010).
- [Law95] C. K. Law. *Phys. Rev. A* **51**, 2537 (1995).
- [Ludwig08] M. Ludwig, B. Kubala, and F. Marquardt. *New Journal of Physics* **10**, 095013 (2008).
- [Lvovsky09] A. I. Lvovsky and M. G. Raymer. *Rev. Mod. Phys.* **81**, 299 (2009).

-
- [Marquardt09] F. Marquardt and S. M. Girvin. *Physics* **2**, 40 (2009).
- [Meystre13] P. Meystre. *Annalen* **525**, 215 (2013).
- [Miller05] R. Miller, T. E. Northup, K. M. Birnbaum, A. Boca, A. D. Boozer, and H. J. Kimble. *Journal of Physics B: Atomic, Molecular and Optical Physics* **38**, S551 (2005).
- [Mølmer93] K. Mølmer, Y. Castin, and J. Dalibard. *J. Opt. Soc. Am. B* **10**, 524 (1993).
- [Peropadre10] B. Peropadre, P. Forn-Diaz, E. Solano, and J. J. Garcia-Ripoll. *Phys. Rev. Lett.* **105**, 023601 (2010).
- [Rabi37] I. I. Rabi. *Phys. Rev.* **51**, 652 (1937).
- [Raimond01] J. M. Raimond, M. Brune, and S. Haroche. *Rev. Mod. Phys.* **73**, 565 (2001).
- [Rempe87] G. Rempe, H. Walther, and N. Klein. *Phys. Rev. Lett.* **58**, 353 (1987).
- [Rigo96] M. Rigo and N. Gisin. *Quantum Semiclass. Opt.* **8**, 255 (1996).
- [Schack95] R. Schack, T. A. Brun, and I. C. Percival. *J. Phys. A: Math. Gen.* **28**, 5401 (1995).
- [Schack97] R. Schack and T. A. Brun. *Comput. Phys. Commun.* **102**, 210 (1997).
- [Schubert12] R. Schubert, R. O. Vallejos, and F. Toscano. *Journal of Physics A: Mathematical and Theoretical* **45**, 215307 (2012).
- [Spiller94] T. Spiller and J. Ralph. *Physics Letters A* **194**, 235 (1994).
- [Strunz98] W. T. Strunz and I. C. Percival. *J. Phys. A: Math. Gen.* **31**, 1801 (1998).
- [Tal-Ezer84] H. Tal-Ezer and R. Kosloff. *J. Chem. Phys.* **81**, 3967 (1984).
- [Vidal07] J. Vidal, S. Dusuel, and T. Barthel. *Journal of Statistical Mechanics: Theory and Experiment* **2007**, P01015 (2007).
- [Walther06] H. Walther, B. T. H. Varcoe, B.-G. Englert, and T. Becker. *Reports on Progress in Physics* **69**, 1325 (2006).
- [Wang73] Y. K. Wang and F. T. Hioe. *Phys. Rev. A* **7**, 831 (1973).
- [Weiße06] A. Weiße, G. Wellein, A. Alvermann, and H. Fehske. *Rev. Mod. Phys.* **78**, 275 (2006).
- [Xiang13] Z.-L. Xiang, S. Ashhab, J. Q. You, and F. Nori. *Rev. Mod. Phys.* **85**, 623 (2013).

- [Zhang90] W.-M. Zhang, D. H. Feng, and R. Gilmore. *Rev. Mod. Phys.* **62**, 867 (1990).
- [Zheng95] X. Zheng and C. M. Savage. *Phys. Rev. A* **51**, 792 (1995).

Publications and Conferences

Publications

- (a) A. Alvermann, L. Bakemeier, and H. Fehske, “Collapse-revival dynamics and atom-field entanglement in the nonresonant Dicke model”, *Phys. Rev. A* **85**, 043803 (2012). Copyright (2012) by the American Physical Society.
- (b) L. Bakemeier, A. Alvermann, and H. Fehske, “Quantum phase transition in the Dicke model with critical and noncritical entanglement”, *Phys. Rev. A* **85**, 043821 (2012). Copyright (2012) by the American Physical Society.
- (c) L. Bakemeier, A. Alvermann, and H. Fehske, “Dynamics of the Dicke model close to the classical limit”, *Phys. Rev. A* **88**, 043835 (2013). Copyright (2013) by the American Physical Society.
- (d) L. Bakemeier, A. Alvermann, and H. Fehske, “Variational treatment of entanglement in the Dicke model”, submitted to *Physica Scripta*
- (e) L. Bakemeier, A. Alvermann, and H. Fehske, “Route to chaos in optomechanics”, submitted to *Phys. Rev. Lett.*

Talks

- (a) “Dynamics of the Rabi model on different time scales”, DPG Spring meeting, Dresden, 2011
- (b) “Route to chaos in optomechanics”, SFB 652 meeting, Plau am See, 2014

Posters

- (a) “Quantum dynamics of a spin-boson system close to a classical phase transition”, DPG Spring Meeting, Regensburg, 2010
- (b) “Evolution of atom-field entanglement during collapse & revival of Schrödinger cat states”, International conference on correlation effects in radiation fields (CERF), Rostock, 2011
- (c) “Quantum-classical correspondence in the dynamics of the Dicke model”, DPG Spring Meeting, Regensburg, 2013
- (d) “Quantum-classical correspondence in the dynamics of the Dicke model”, Frontiers of Quantum and Mesoscopic Thermodynamics, Prague, 2013

Erklärung

Hiermit erkläre ich, dass diese Arbeit bisher von mir weder an der Mathematisch-Naturwissenschaftlichen Fakultät der Ernst-Moritz-Arndt-Universität Greifswald noch einer anderen wissenschaftlichen Einrichtung zum Zwecke der Promotion eingereicht wurde. Ferner erkläre ich, dass ich diese Arbeit selbständig verfasst und keine anderen als die darin angegebenen Hilfsmittel und Hilfen benutzt und keine Textabschnitte eines Dritten ohne Kennzeichnung übernommen habe.

(Lutz Bakemeier)

Greifswald, 21 October 2014

Acknowledgement

I extend my deepest gratitude to

Holger Fehske,

Andreas Alvermann,

my colleagues and my family

for their advice, inspiration, and support.

Moreover, I thank the

Deutsche Forschungsgemeinschaft

for financial support through the research program SFB 652, project B5.